

DOPPLER RADAR OBSERVATIONS OF
AN OKLAHOMA DOWNBURST

by

Marilyn Mitchell Wolfson

B.S., University of Michigan (1979)

Submitted to the Department of Meteorology
and Physical Oceanography in partial
fulfillment of the degree of

Master of Science


at the

Massachusetts Institute of Technology

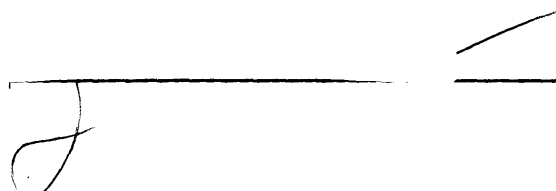
February 1983

© Massachusetts Institute of Technology 1983


Signature of Auth


Department of Meteorology
and Physical Oceanography
January, 1983

Certified by


Kerry Emanuel
Thesis Supervisor

Accepted by


Ronald Prinn
Chairman, Departmental Committee
on Graduate Students

WITHDRAWN
Lindgren
MASSACHUSETTS INSTITUTE
OF TECHNOLOGY
FROM
MIT LIBRARIES
MAR 22 1983

DOPPLER RADAR OBSERVATIONS OF

AN OKLAHOMA DOWNBURST

by

Marilyn Mitchell Wolfson

Submitted to the Department of Meteorology
and Physical Oceanography on February 18, 1983 in partial
fulfillment of the requirements for the degree of

Master of Science in Meteorology

ABSTRACT

Detailed Doppler radar observations of a thunderstorm along a cold front in Oklahoma on 13 April 1981 reveal the existence of at least one "downburst". They indicate that the downburst, a small scale intense downdraft which hits the surface and causes high winds, is a strictly low level phenomenon. The distinctive "bow" radar echo appears to be caused by cyclonic rotation of the storm and the "spearhead" echo appears to be due to cell formation along an occluded gust front ahead of the main storm cell.

A new hypothesis for the thunderstorm downburst is suggested which differs from previous theories that rely largely on thermodynamic arguments. It is proposed that increased low level convergence due to the thunderstorm outflow intensifies the ambient cyclonic vorticity which, in turn, induces the dynamic vertical pressure gradient responsible for the downburst.

Also, a technique for deriving the horizontal vector windfield from radial velocity measurements, using the constraints of irrotationality or nondivergence, is developed and tested. While the derived winds are not meant to indicate the real windfield, preliminary results show that they are more useful in inferring storm structure than simple contour maps of the Doppler velocity field.

Thesis supervisor: Dr. Kerry Emanuel

Title: Assistant Professor of Meteorology

CONTENTS

| | |
|--|----|
| 1. Introduction..... | 4 |
| 2. Review of Past Work on Downbursts..... | 6 |
| 3. Overview of the Synoptic Situation..... | 13 |
| 4. Doppler Radar Data Analysis..... | 18 |
| A. Plan View..... | 18 |
| B. Side View..... | 36 |
| 5. Two Dimensional Wind Field from Single Doppler Radar..... | 49 |
| A. Three experiments..... | 51 |
| B. Discussion of derived winds..... | 69 |
| 6. A New Hypothesis..... | 75 |
| 7. Conclusions and Future Work..... | 80 |
| APPENDIX A..... | 82 |
| APPENDIX B..... | 89 |
| APPENDIX C..... | 93 |
| Acknowledgements..... | 96 |
| References..... | 98 |

1. Introduction

The subject of this thesis is the downburst, a small intense downdraft at very low levels in a thunderstorm. Downbursts and the outflow of wind they cause at the surface are known to be responsible for several jet airplane crashes in the last ten years and there is some speculation that the July 1982 accident in New Orleans may also have been caused by winds from a downburst. The destructive nature of downbursts and the high risk they pose to the safe operation of aircraft near thunderstorms make their accurate prediction a very desirable goal. This will not be achieved, however, until the theoretical understanding of downbursts improves.

The 1982 Joint Airport Weather Studies (JAWS) observing experiment was organized in an attempt to gather data and learn more about downbursts. The JAWS project took place around the Denver, Colorado airport where, in 1975, a downburst related aviation accident occurred. Many downbursts were detected but most of them were of the type now being called "dry" or "cumulus" or "virga" downbursts. A distinction must be made between these and the "wet" or "thunderstorm" downbursts which are the subject of this study. The two phenomena are very different. They are easy to distinguish: the former come from benign looking cumulus clouds over the high plains and fall through a very deep and dry subcloud layer and the latter are associated with thunderstorms. Thunderstorm downbursts have been detected throughout the Great Plains and the Midwest, on the east coast, and in Florida, while the cumulus downbursts have only been reported over the high plains east of the Rockies.

In Chapter 2 of this thesis I review some of the past work on downbursts including observations and proposed theoretical explanations. Chapter 3 contains a brief overview of the synoptic situation leading up to the formation of the thunderstorm investigated here, and Chapter 4 contains a detailed analysis of Doppler radar data gathered while the downburst was occurring. Ten separate views of the storm at times no more than 7 and as few as 3 minutes apart during a 50 minute period represent better resolution than is available in any of the past observational downburst studies. In Chapter 5 a new technique is tested for estimating the horizontal windfield from single Doppler radar measurements, and in the second section of that chapter some features of the estimated windfields are discussed. Using the observations as a guideline, a new hypothesis for the downburst is developed in Chapter 6. Conclusions and suggestions for further work are presented in Chapter 7.

2. Review of Past Work on Downbursts

The word "downburst" was introduced in a paper by Fujita and Byers (1972) to describe the situation in which a thunderstorm downdraft becomes hazardous to the operation of jet aircraft. If the downdraft has a speed of at least 12 fps at 300 feet above the surface, which is comparable to that of a jet transport following the usual 3° glideslope on final approach, and an aerial extent 800 m or larger, which is big enough to have a noticeable effect on the aircraft (Fujita and Caracena, 1977), then it qualifies as a downburst.

One may rightly wonder what the difference is between the downburst and the well known, well researched thunderstorm downdraft. At first Fujita (1979) thought that they were essentially the same but that, in the same way a funnel cloud aloft is not called a tornado, a mid-level downdraft in a thunderstorm would not be called a downburst. The definition was later refined when it was decided that the downburst must induce "an outburst of damaging winds on or near the ground" (Fujita and Wakimoto, 1981) where "damaging winds" refers to winds that can be estimated on the F-scale (for which the minimum threshold is 18 m/s). These damaging winds can be either straight or curved but they must be highly divergent (Fujita, 1981). Thus, even in its most recent and more meteorological definition, the term "downburst" is meant to signify a potential human hazard. Whether or not it also signifies a distinct phenomenon in the atmosphere is a matter of some debate, and one which will be investigated in the current work.

Much effort has been spent relating specific radar echoes to ground damage and reports of severe weather. In the course of his

investigation of the airplane accident at JFK airport in June, 1975 Fujita (1976) associated damaging downburst winds on the ground with a "radar echo with a pointed appendage extending toward the direction of the echo motion" which he called a "spearhead" echo. "The appendage moves much faster than the parent echo which is being drawn into the appendage. During the mature stage, the appendage turns into a major echo and the parent echo loses its identity."

After further observational work a more general type of echo with which downbursts were associated was identified by Fujita (1978) as the "bow" echo which then takes the shape of a "spearhead" echo during the strong downburst stage and which sometimes develops a weak echo channel in the area of strongest winds. There is some question as to whether the downburst is simply associated with or actually causes these distinctive echo configurations. A schematic drawing of the bow echo evolution as proposed by Fujita is presented in figure 2-1 and radar images of a confirmed downburst thunderstorm in Illinois are shown in figure 2-2. Notice the cyclonic circulation north of the spearhead and downburst where Fujita has indicated a tornado. An extensive ground damage survey of that downburst thunderstorm on 6 August 1977 in Springfield, Illinois by Forbes and Wakimoto (1981) revealed many downbursts, microbursts (downbursts with dimensions less than 4 km), and tornadoes. Their results consistently show the strong cyclonic curvature and tornado paths to be on the north (left) side of the diverging wind pattern of the downbursts.

A study of radar intensity data associated with reports of tornadoes by Nolen (1959) led to the identification of the Line Echo Wave Pattern (LEWP). The LEWP was defined as a "configuration of radar

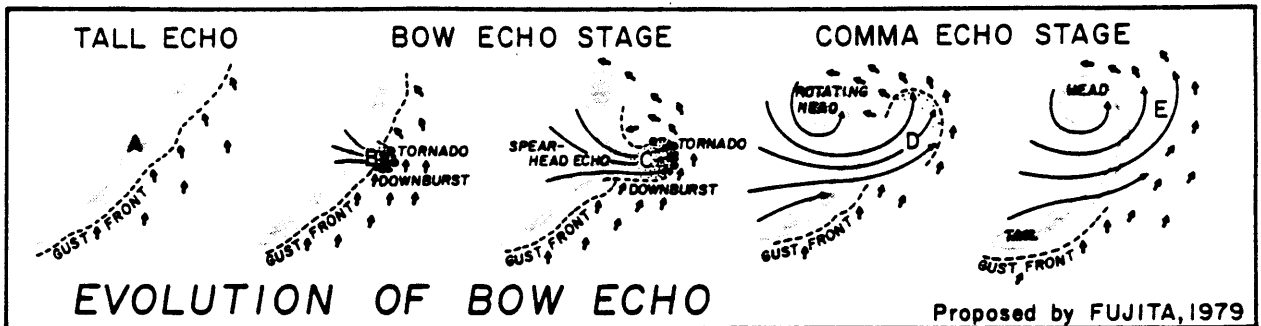


Figure 2-1 Evolution of bow echo proposed by Fujita in 1979. In his model a bow echo is produced by a downburst thunderstorm as the downflow cascades down to the ground. Finally the horizontal flow of a weakening downburst induces a mesoscale circulation which distorts the initial line echo into a comma-shaped echo with a rotating head. From Fujita(1981)



Figure 2-2 Radar pictures showing a bow echo which turns into a spearhead echo and then into a comma echo. During its spearhead stage, this bow echo produced a cluster of 10 downbursts near Springfield, Illinois on 6 August 1977. (25 n mi range markers)
From Fujita, (1981)

echoes in which a line of echoes has been subjected to an acceleration along one portion and/or a deceleration along that portion of the line immediately adjacent, with a resulting sinusoidal mesoscale wave pattern in the line." There is a definite similarity to the bow echo and, in fact, Nolen found many examples of the LEWP which had associated reports of high winds but not tornadoes. Hamilton (1970) was able to deduce a meso-low surface pressure area associated with the crest of the LEWP from the shape of the squall line as depicted on radar.

Fujita (1978) has documented downbursts associated with hook echoes, a distinctive configuration known to be a good indicator of at least a mesocyclone and often a tornado. He has documented a series of downbursts which all occurred on the south side of a mesocyclone moving from northwest to southeast across the Kansas-Missouri border, he has documented many twisting downbursts which show rotational as well as divergent wind patterns, and he has even inferred the existence of a downburst from the damage pattern left by a hurricane over land. It is difficult to ignore these coincidental occurrences of downbursts with strong cyclonic rotation. Yet most explanations for the downburst do exactly that.

Fujita (1976) and Fujita and Byers (1977) developed a model of the downburst thunderstorm which accounted for the spearhead echo. They proposed that the downburst is caused by the collapse of an overshooting top on a large tall cell. The potential energy of the cloud top is converted into kinetic energy of the descending air which, by virtue of its large horizontal momentum, moves faster than neighboring parts of the same echo. The downward motion is accelerated by the evaporation of water droplets into the dry air that must be entrained along the way.

The main downdraft in a mature thunderstorm is a result of the cooling of dry mid-level air within the storm and/or the cooling of sub-cloudbase air by evaporation. The downdraft produces an outflow of air beneath the storm, but the vertical velocities are weak when the cooled air reaches the surface. There is often a gust front at the edge of the outflow with associated wind shear and a dramatic temperature drop. The similarity between Fujita's proposed mechanism for downbursts and the mechanism known to produce the thunderstorm downdraft led some scientists to the conclusion that Fujita was observing ground damage caused by the gust front itself. As observations accumulated, it became clear that the gust front was one of the key ingredients but that the downburst was a smaller scale, separate phenomenon. Caracena (1978) suggests that a large downdraft may naturally contain an ensemble of small impulsive components of various intensities, and that downbursts and microbursts may simply be the stronger ones of these. He also notes that they may occur more commonly than one might expect from the relatively few published case studies.

A study was done by Caracena and Maier (1979) of a microburst associated with a thunderstorm which passed over the Florida Area Cumulus Experiment surface mesonet network. They concluded that the spearhead echo associated with that storm was "symptomatic of strong boundary layer forcing and moisture flux convergence". This, however, did not explain why or how microbursts occurred. The authors noted that a technique by Foster (1958), based on moist adiabatic descent of downdraft air consisting of a mixture of midlevel air and updraft air, failed to account for the strength of the observed winds. They suggest that the necessary additional sources of negative buoyancy might be "the

unmixed entrainment of environmental air into the rain shaft and/or the melting of a large quantity of precipitation".

Although downbursts come in many different sizes (Caracena, 1978; Fujita and Wakimoto, 1981) ranging from 1 km to 40 km with extremes of 0.1 km and 200 km, most documented thunderstorm downbursts are on the order of 5 km across and are much smaller and stronger than the main downdrafts. This discrepancy led Emanuel (1981) to speculate that downbursts may be due to a dynamically distinct mechanism. He suggests that downbursts are manifestations of the "penetrative downdraft" which could account for their strength and small scale. The potential for penetrative downdrafts inside a thunderstorm exists when cool dry air overlies cloudy air of high liquid water content. The updraft - downdraft configuration in a supercell thunderstorm may provide this setting. Emanuel is the first theoretician to suggest some connection between the storm rotation and the downburst although, in his scenario, the rotation serves only to trap air of high liquid water content and small vertical velocity directly below a region of inflowing potentially cold air, thus setting up a conducive environment for the penetrative downdrafts.

None of the aforementioned mechanisms have been demonstrated to be the actual cause of downbursts although they are all plausible. They do provide some suggestion of what to look for in the observations.

In summary, the recurring parts of the puzzle appear to be: a particularly strong cell within a line of thunderstorms; a bow echo or LEWP in the mature stage of the cell; a gust front; some small scale rotation; decay of the parent cell as the echo shape begins to resemble a spearhead; strong surface winds, the downburst, and maybe a tornado;

and a possible weak echo trench in the vicinity of the strongest winds. In these latter stages, the storm is decaying rapidly. The rest of this work will be concerned with trying to recognize these phenomena in the radar observations of an Oklahoma thunderstorm and with understanding just how they combine to produce the downburst.

3. Overview of the Synoptic Situation

On 13 April 1981 during the National Severe Storms Laboratory Spring Program a warm humid southerly airflow was present over Oklahoma, with a cold front oriented southwest to northeast moving into the state from the northwest. The surface analysis for 2300Z (1700 CST) or approximately five hours before the front came into the Norman, OK area is presented in figure 3-1.

Temperatures in the warm sector were in the low to mid-eighties while dew points were between 60°F and 70°F. Temperatures in the air behind the cold front were considerably lower, ranging from about 70°F close to the front to the lower fifties well back into the cold high pressure region. Dew points in the cold air were correspondingly lower, between 30°F and 45°F.

A sounding taken at Tuttle, OK (Tuttle is marked with a triangle in figure 4-2) shows warm moist surface air, a slight capping inversion at 850 mb and an approximately dry adiabatic lapse rate up to 500 mb (figure 3-2). This sounding was taken at 2005 CST, an hour before the thunderstorm arrived, and is representative of the pre-storm environment. The surface winds are light from the southwest but at slightly higher levels a southerly low level jet is present. The winds turn gradually to become more westerly and stronger with height.

The enhanced IR GOES-EAST satellite picture (figure 3-3) taken at 300Z (2100 CST) shows strong convection along the cold front. The most vigorous tall thunderstorms are located in Texas and on the Texas - Oklahoma border, while the cloudtops over Oklahoma are basically featureless. This is probably because the "blowoff" from the Texas

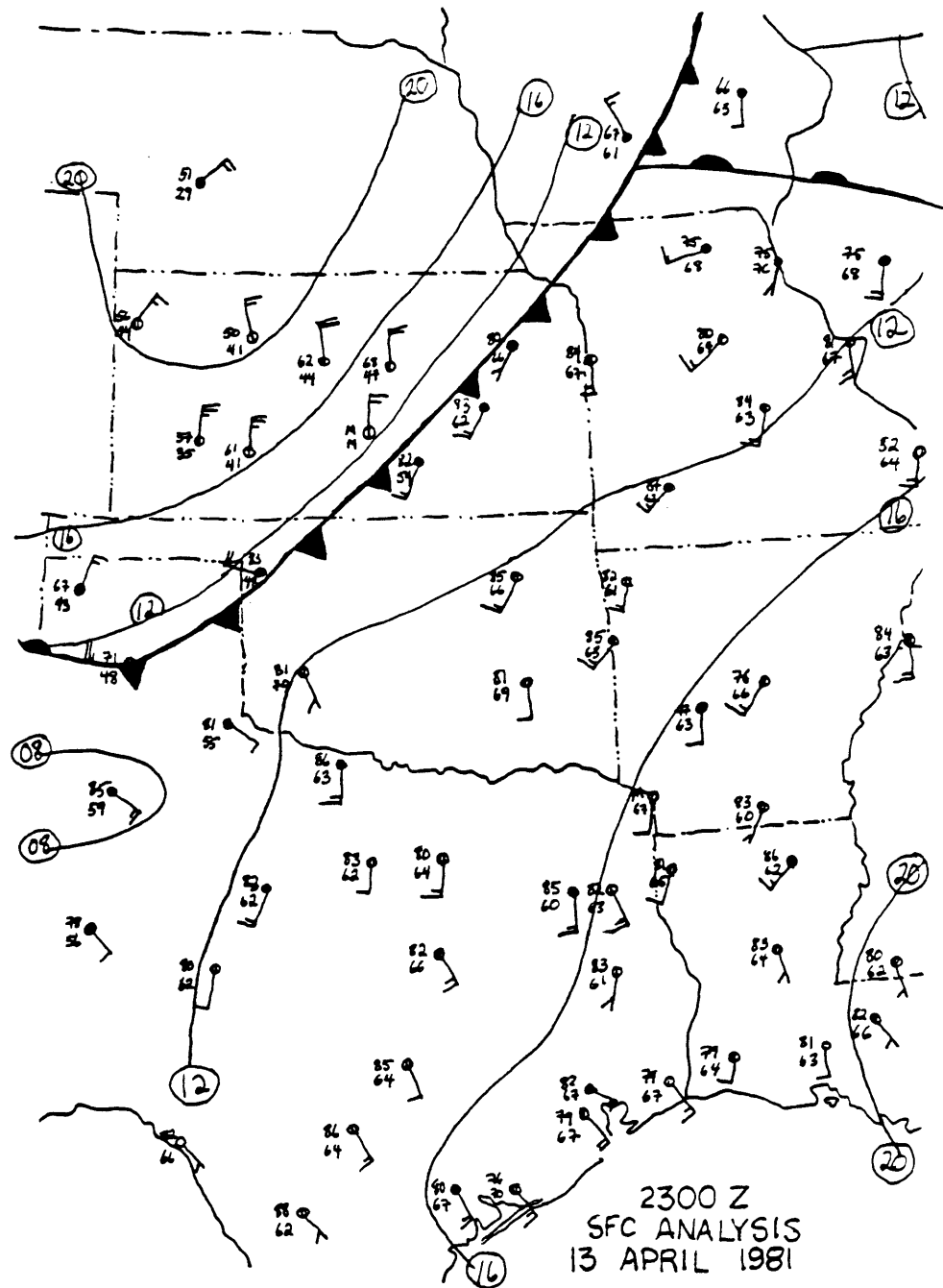


Figure 3-1 Surface map with all available stations plotted according to the conventional model. Temperatures and dewpoints are in °F. Isobars are labeled as the excess (in mb) over 1000 mb. This map was analyzed and kindly made available by John DiStefano.

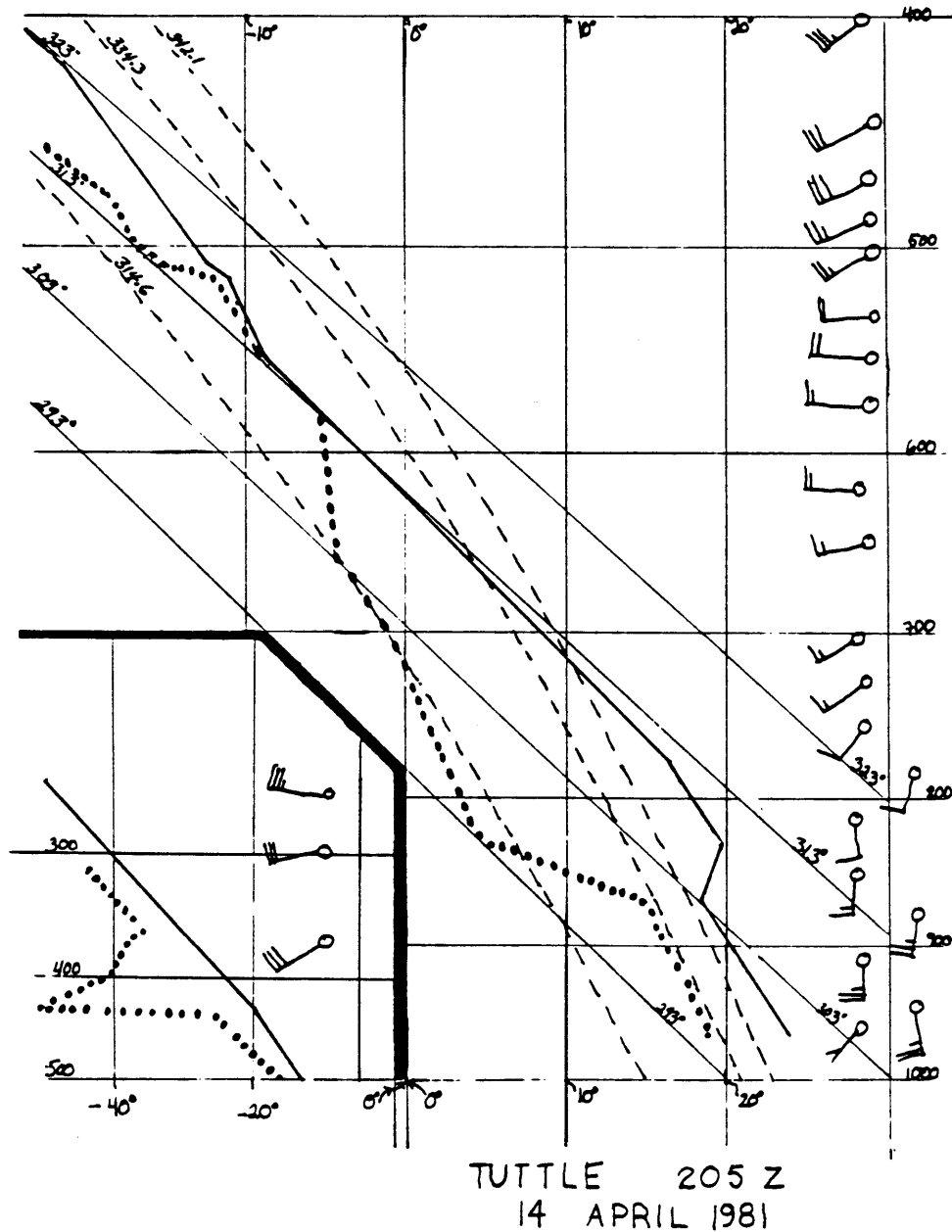


Figure 3-2 Tuttle sounding. The solid unlabeled line is the temperature sounding and the dotted line is the dewpoint sounding. Horizontal solid lines are pressure labelled in millibars and vertical solid lines are temperature in °C. Solid sloping lines are dry adiabats labelled in K and dashed sloping lines are moist adiabats.

(Plotted by
John DiStefano)



Figure 3-3 Enhanced IR satellite photo (MB curve) taken by the GOES - EAST satellite at 300Z on 14 April 1981

storm is blanketing and obscuring the tops of the weaker line of storms in Oklahoma. There is, however, some suggestion of a second point source in OK where the anvil appears to bulge out and then become narrow again to the northeast. Because of the obscuring "blowoff" from the Texas storm there is no evidence of extreme cloud top warming (8°C, Fujita, 1978) during the downburst or cooling afterward, nor is there evidence of any large rapid changes in the areal extent of the anvil.

4. Doppler Radar Data Analysis

Much information can be gained by examining the reflectivity and radial velocity fields observed by the Norman, OK Doppler radar (NRO) while the downburst was occurring. A preliminary overview of the evolution of the line echo can be obtained from the Norman WSR-57 radar images (figure 4-1). This information is valuable because it often represents the only radar coverage of a storm and much of the literature on downbursts relies on this type of representation.

Notice that at 2100 CST a strong circular cell is present and the line has begun to protrude south of that cell. The echo has reached the "bow" echo stage. By 2110 the echo has entered the "spearhead" stage and the LEWP is evident.

The results from NRO are extremely detailed in comparison with those from the WSR-57 radar. Ten tilt sequences were recorded during the fifty minutes between 2045 and 2135 CST and the rapidly changing nature of this storm required that all of them be analyzed. Details of the available coverage and the data analysis are contained in Appendix A. The results are plotted on a 50 km^2 grid in a Cartesian coordinate system with the origin at NRO. Both the Cartesian and radial (radar) coordinate systems as well as the location of the storm at various analysis times are shown in figure 4-2.

A. Plan View

A series of maps showing the evolution of the reflectivity and Doppler velocity fields at 1.0 km above the ground is presented in figures 4-3 through 4-12. Negative values of Doppler velocity signify

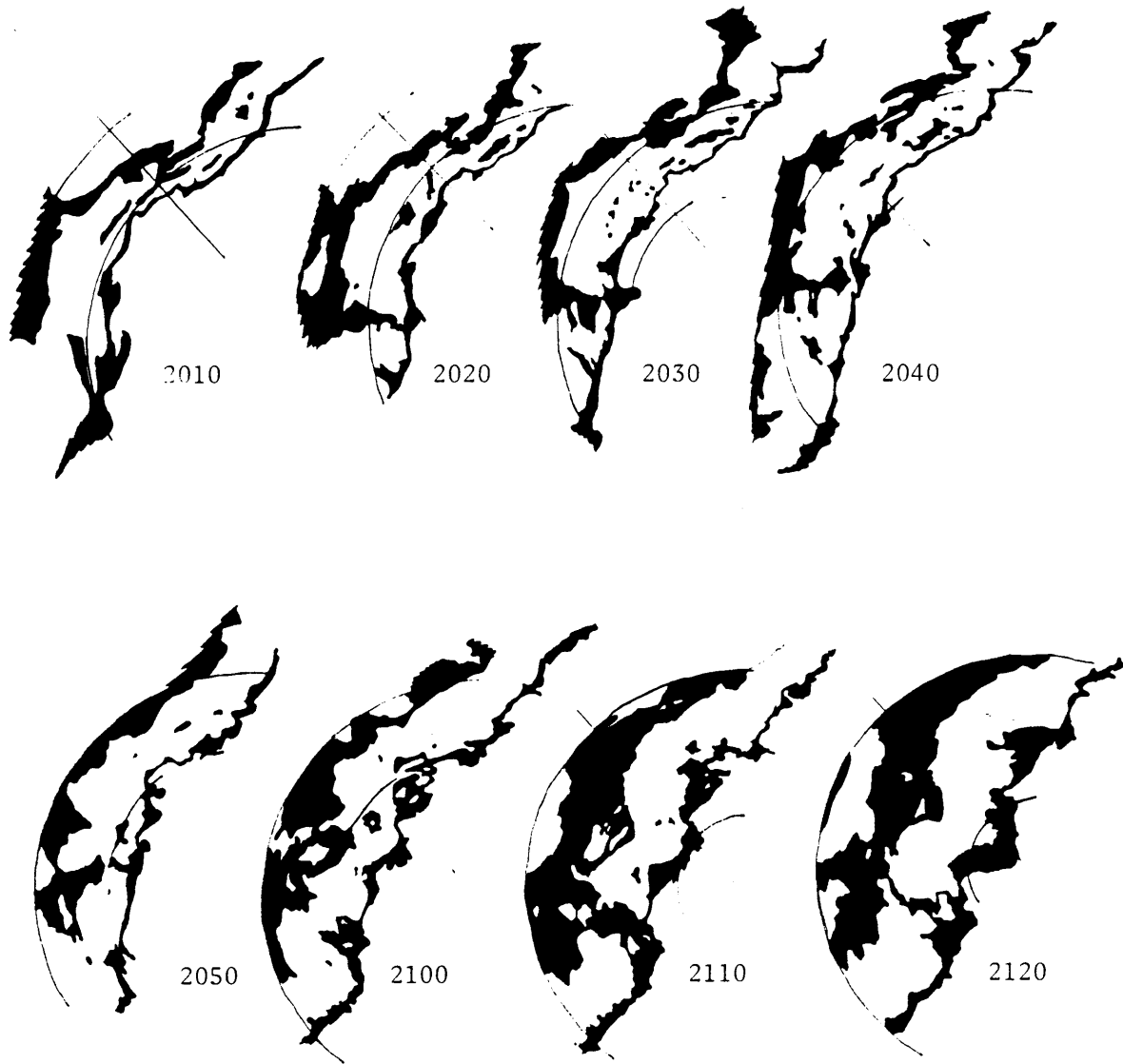

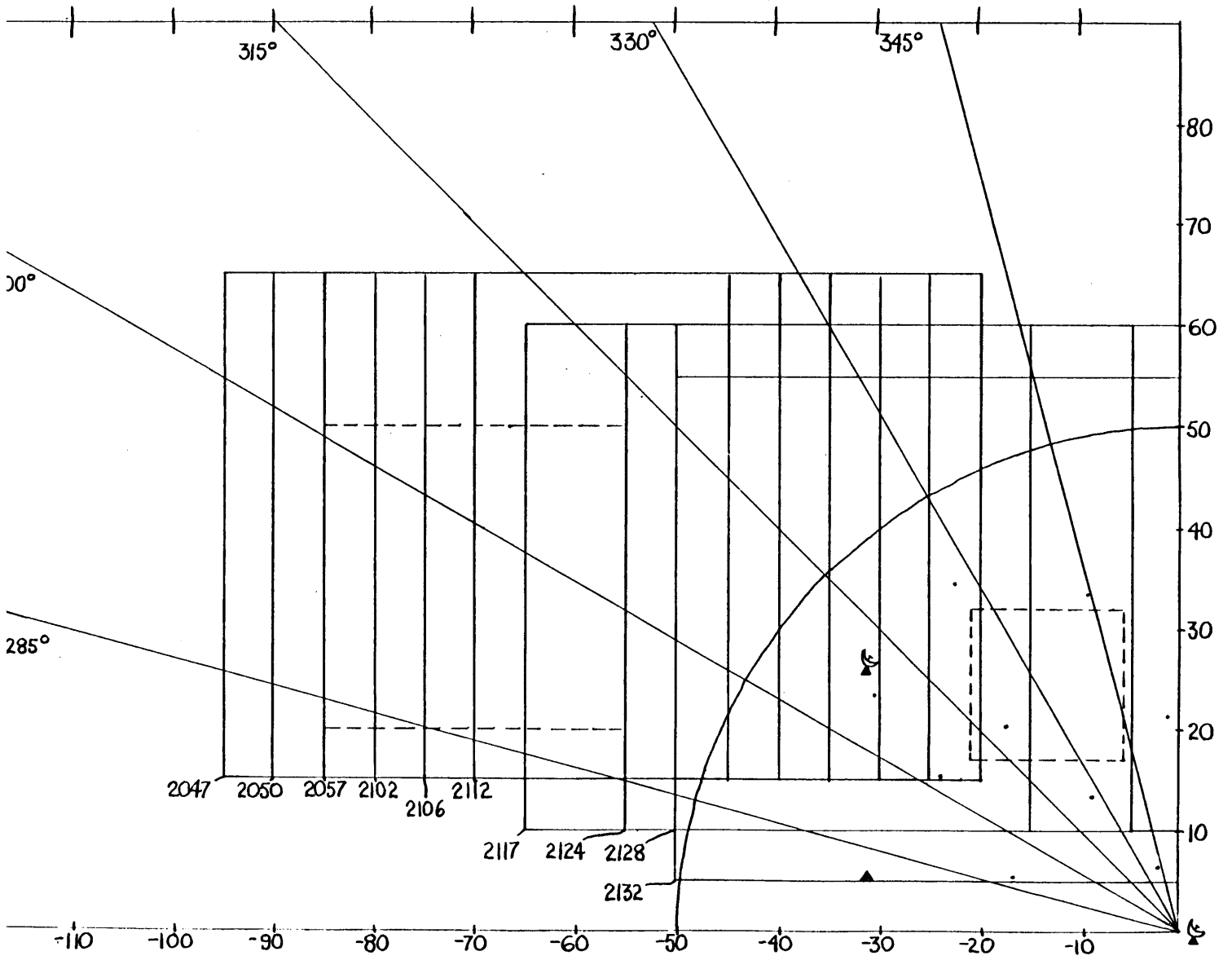


Figure 4-1 Norman WSR-57 integrated received power at the times shown (CST) on 13 April 1981. These are PPI displays at 0° elevation. The large arc in each picture is the 120 km range ring and the thin straight line is the 320° radial.

Figure 4-2 Depicted on the following page is the Norman, OK radar coordinate system used in displaying the analyses. The origin is at the Norman Doppler radar (NRO) and coordinates are labelled in km. The radials are labelled in degrees with 360° at due north. The lower left hand corner of each 50 km^2 box is marked with the time (CST) shown in that box in the following figures. The  symbol represents a Doppler radar, one of which (NRO) is located at the origin and the other of which is Cimarron (CIM) located at 310° and 41 km from the origin. The two dashed boxed show the spaces for which the 2-Doppler analyses were attempted. The left box, 30 square kilometers in area, was chosen for the 2045 CST analysis and the right box, 15 square kilometers, was chosen for the 2130 CST analysis. The small dots located between NRO and CIM are the surface mesonet network stations.



radial motion toward the radar.

The storm is very strong at 2047 CST and 2050 CST (figures 4-3 and 4-4) when reflectivity values greater than 55 dBZ can be found. Based upon analyses of much larger extent (not shown here) it is clear that there is a very well defined gust front oriented in approximately the east-west direction, as evidenced in figure 4-3 by the east-west line or arc of enhanced reflectivity which intercepts the right border at $y=35$. The gust front curves to become more parallel with the cold front slightly farther to the east. This thin line echo is thought by Wakimoto (1982) to be due to a "precipitation roll" which begins in the head of the cold outflow current. It may also be due to dust, insects, or a thermal discontinuity at the outflow edge. It is not clear which thunderstorm cell has produced the outflow responsible for this east-west oriented gust front but it is probably a cell to the northeast of the one depicted in figure 4-3, or perhaps it is a number of different cells along the front whose outflows have merged. There is another gust front present which is definitely due to the outflow from the depicted cell. It is oriented northeast to southwest and is evidenced by the tight reflectivity gradient from 15 to 40 DbZ (Wakimoto, 1982) on the southeast side of the high reflectivity core. In the following discussion I refer to these as two separate gust fronts although, as the cell evolves, this distinction becomes somewhat artificial.

At 2047 CST there is a closed 15 dBZ contour on the east-west gust front. By 2050 this has grown to a 25 dBZ closed contour and at 2057 CST (figure 4-5) there is no longer any distinction between this region and the main echo. The main echo has, however, changed shape

considerably. The rapid growth of this cell was probably due to the increased convergence of inflowing air near the junction of the gust fronts. In a less detailed view, this behavior might suggest the formation of a spearhead echo with the parent echo being drawn into the appendage. At the same time there is a southward protrusion and a suggestion of cyclonic turning of the outflow air behind the north-south gust front. This motion is particularly evident in the -25 m/s "isodop" (line of constant Doppler velocity) and in the increasing velocity gradient between 2047 and 2057 CST.

By 2102 CST (figure 4-6) the cell looks very different. The east-west gust front is still present and a new closed 15 dBZ contour has appeared. A "hole" has developed in the 45 dBZ contour behind the north-south gust front which corresponds to an increased area of maximum velocity toward the radar. The eastern portion of the -25 m/s isodop has become more rounded and extended southeastward while the northern edge has been deflected strongly southwestward suggesting a substantial increase in the cyclonic rotation. Note that the reflectivity field is less than 20 dBZ at the western edge of the depicted domain around $y=25$ and that a cell of greater than 45 dBZ is evident on the southern edge of the domain around $x=-68$.

At 2106 (figure 4-7) the "hole" in the 45 dBZ contour is still evident but the 40 dBZ contour has now protruded southeastward, and a small bullet shaped region of high radial velocities has developed in the same place. The east-west gustfront is characterized by a reflectivity cell of greater than 25 dBZ. The outflow air behind the gust fronts appears to be merging, suggesting an occlusion process. The weak reflectivity region at the southwestern side of the picture has

grown and has curved in an anticyclonic sense, although this does not appear clearly in the Doppler velocity field. Notice, also, the anticyclonic "hook" in the 40 dBZ contour.

The downburst, characterized by low θ_e and maximum wind gusts, is known to have hit the surface mesonet station just south of CIM (coordinates -30, 25) at 2110 CST (DiStefano, 1983). I suggest that the velocity maximum and 40 dBZ protrusion at 2106 are due to the downburst. The reflectivity minimum or "hole" at 2102 appears to be related to the downburst and may be an indication of a newly formed updraft. Note that these features are quite distinct horizontally from the dry region in the southwest.

At 2112 CST (figure 4-8) there is continued dry intrusion from the west and a suggestion of a "weak echo trench" or "spearhead trench" with the spearhead being the deflection of the reflectivity contours probably due to the downburst. It is not at all clear that the dry air to the west and the spearhead are causally connected. The storm has weakened greatly and even the 50 dBZ region is breaking up and shrinking in size. The lobe of high reflectivity extending southeastward with dry (less than 5 dBZ) air behind it is the old east-west gustfront. There may actually be another downburst occurring at this time at $x=-33$, $y=35$ where the reflectivity minimum exists in approximately the same place relative to the core of the storm and the gustfronts as did that at 2102 CST.

In the series of pictures from 2117 to 2132 CST (figures 4-9 to 4-12) the southeastern portion of the Doppler velocity field clearly shows cyclonic rotation of the contours about a point north of the curved finger of high velocities. This cyclonic rotation is confirmed

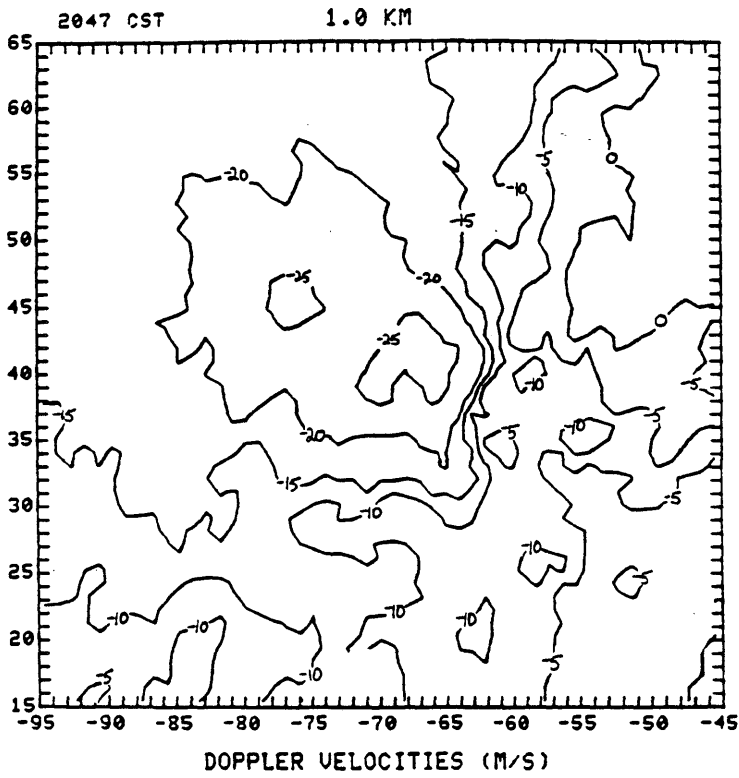
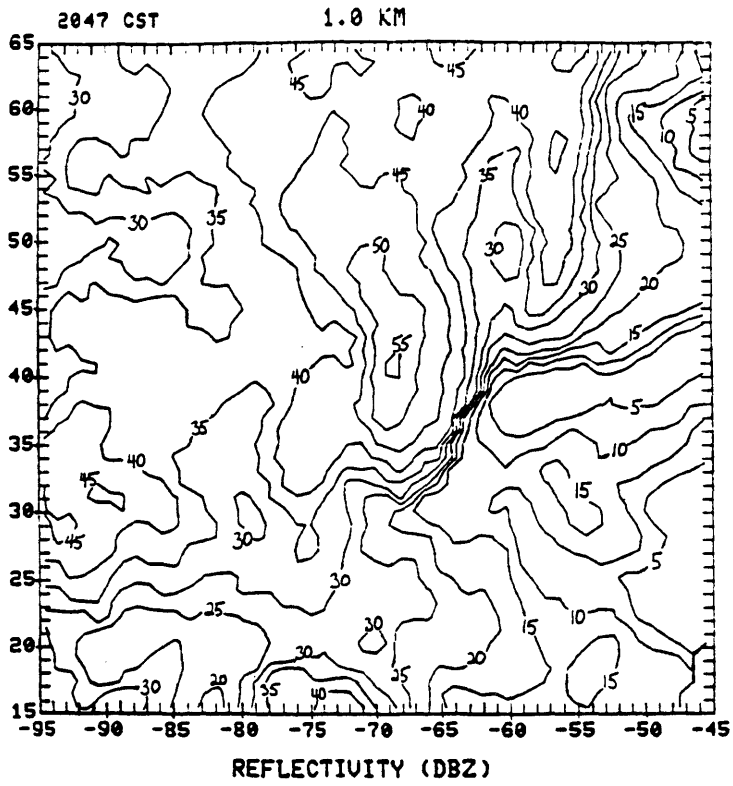


Figure 4-3

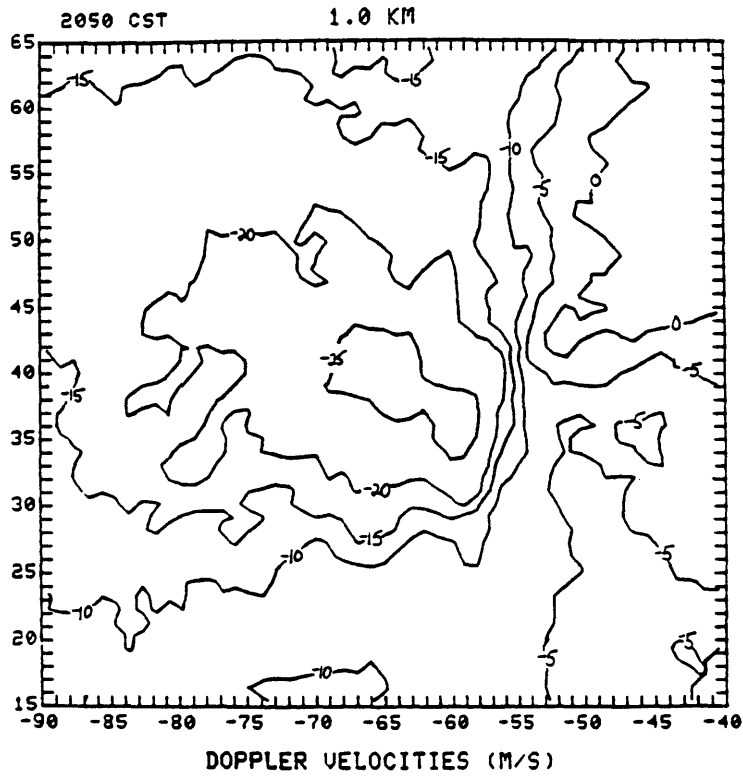
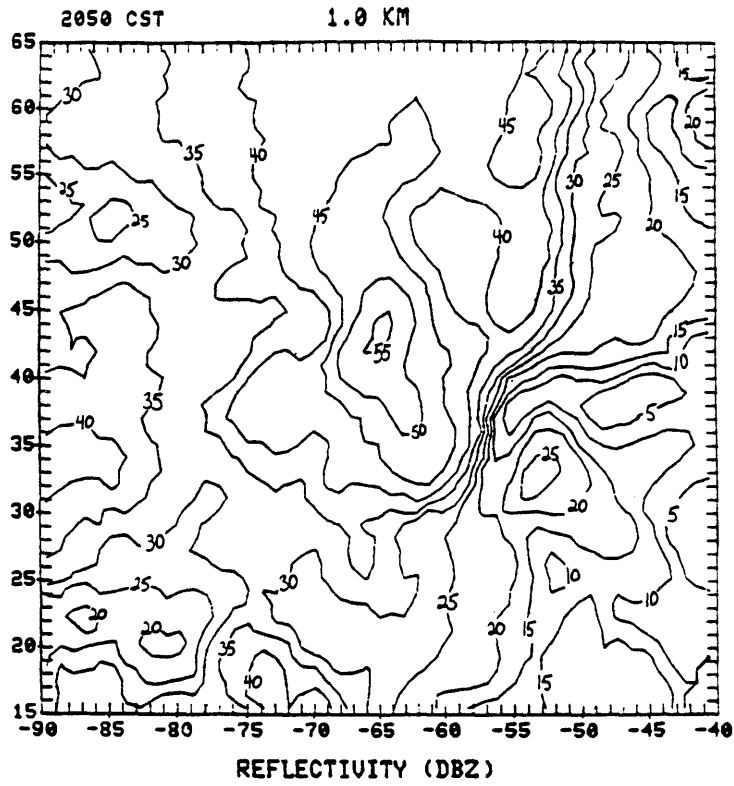


Figure 4-4

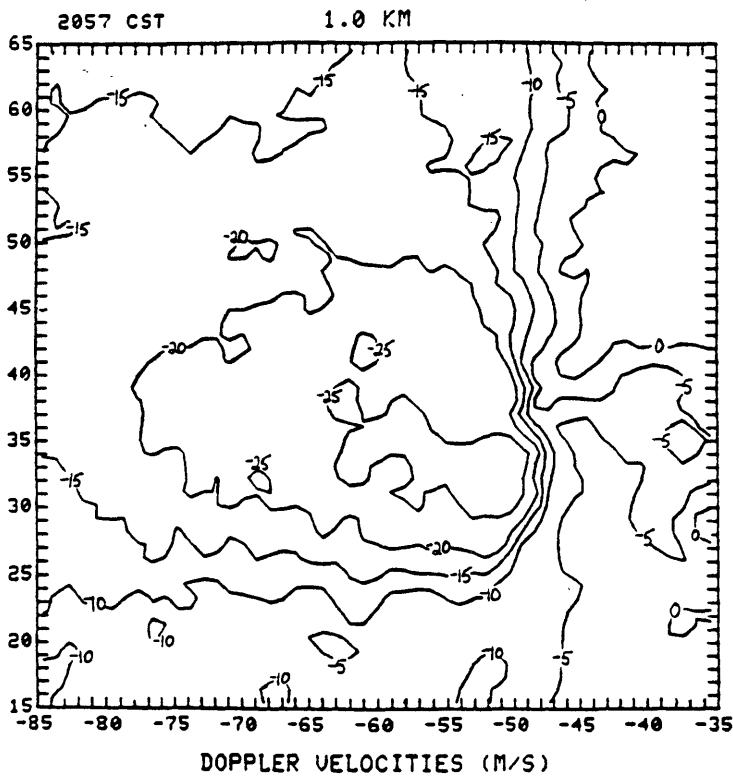
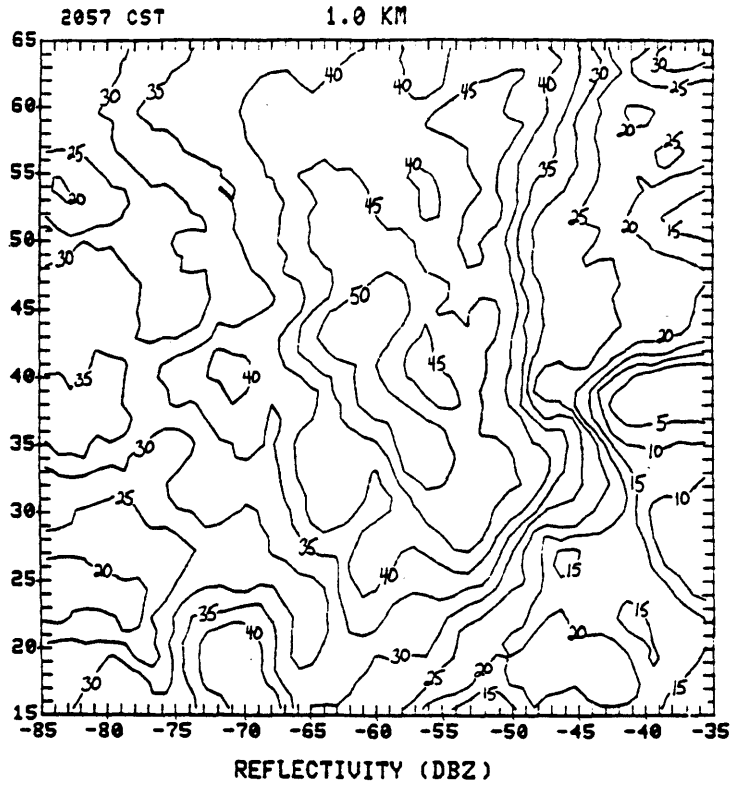


Figure 4-5

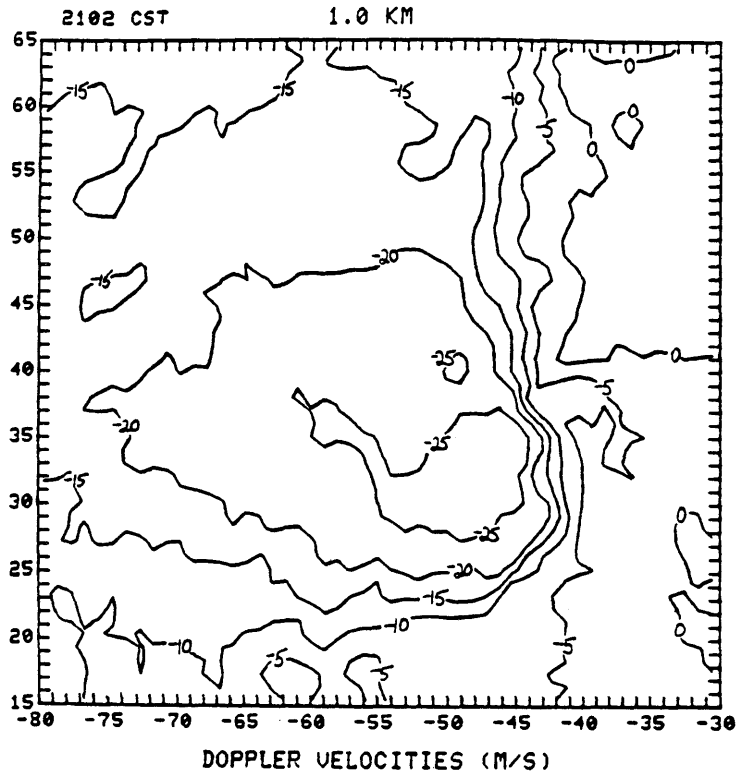
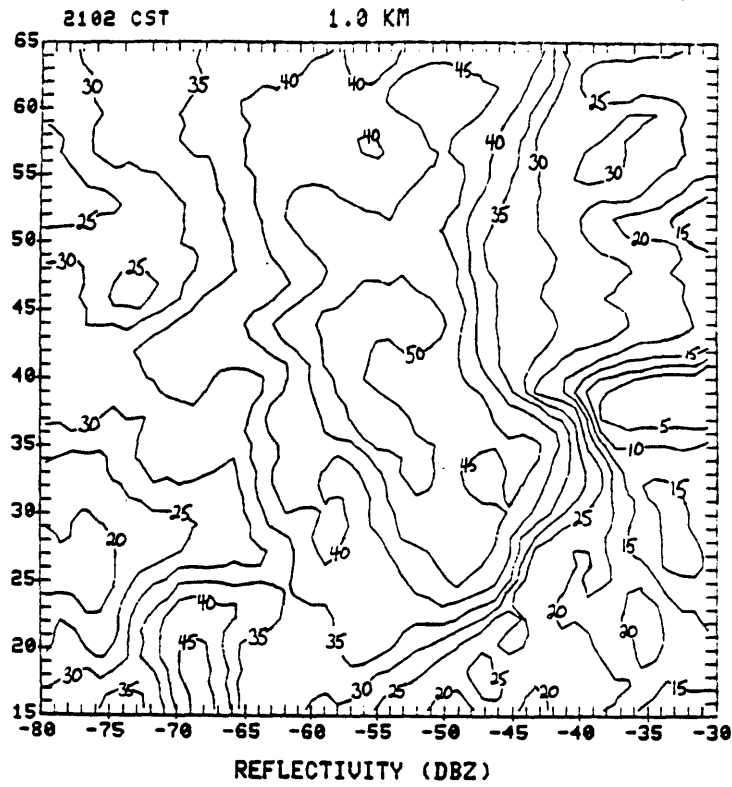


Figure 4-6

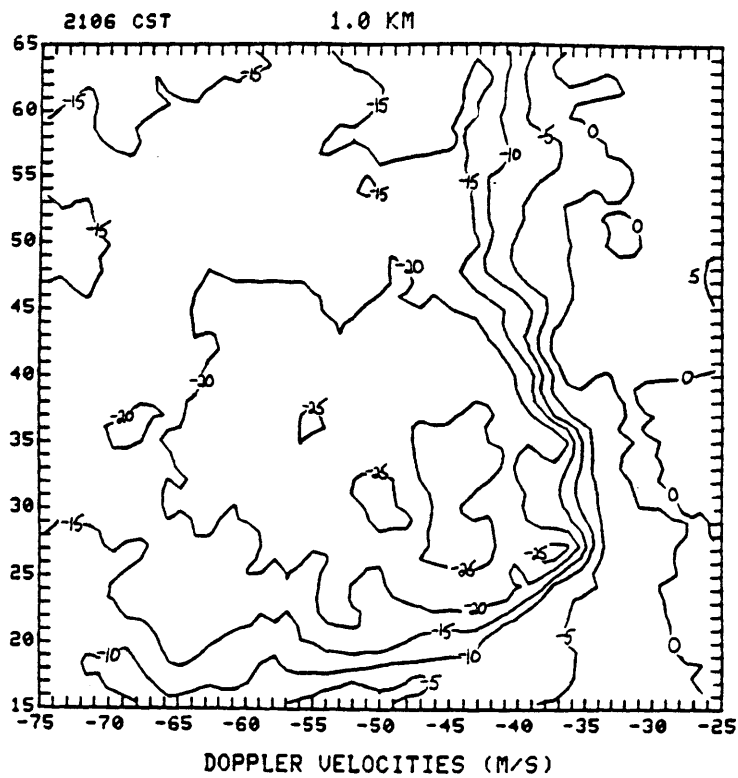
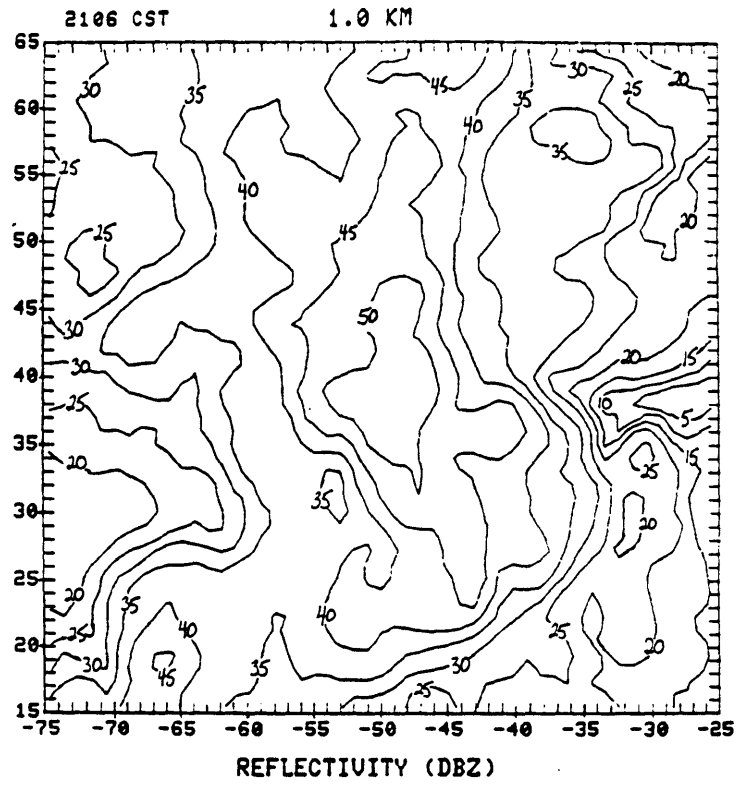


Figure 4-7

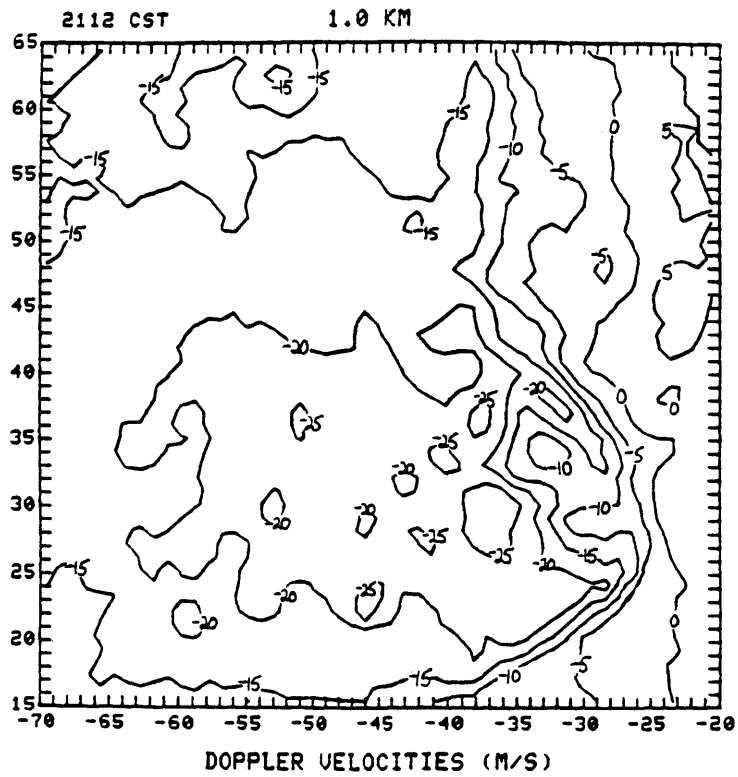
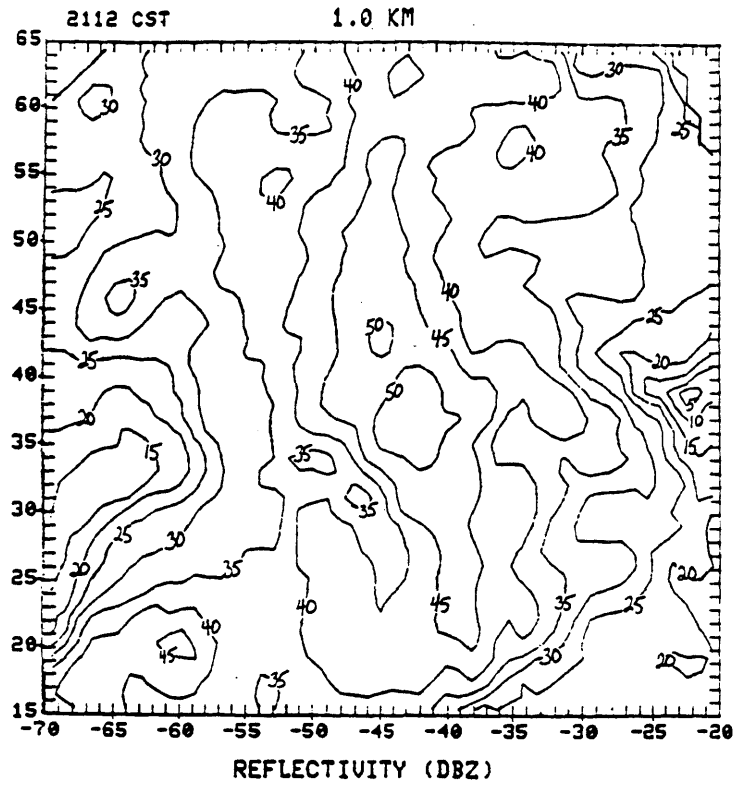


Figure 4-8

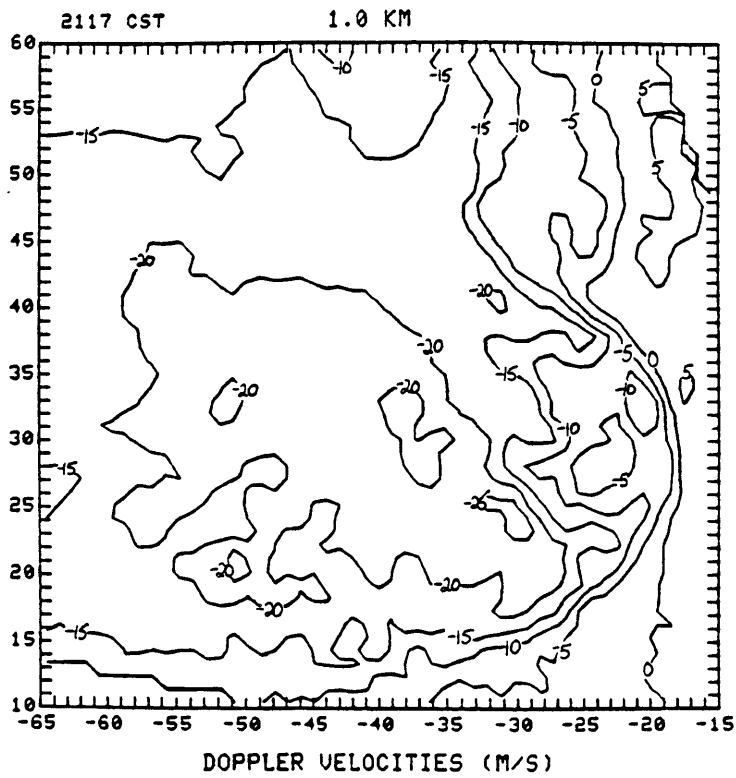
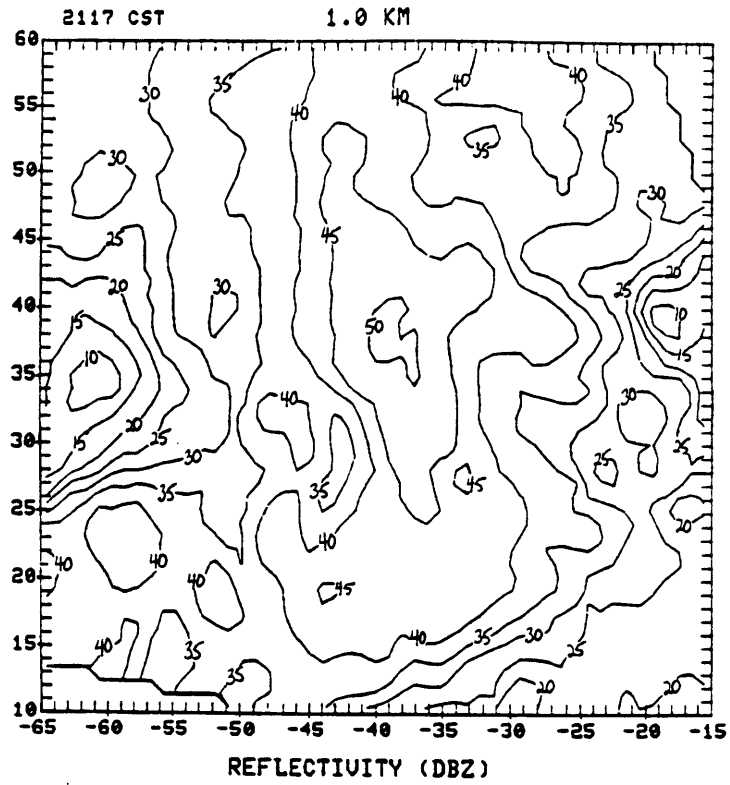


Figure 4-9

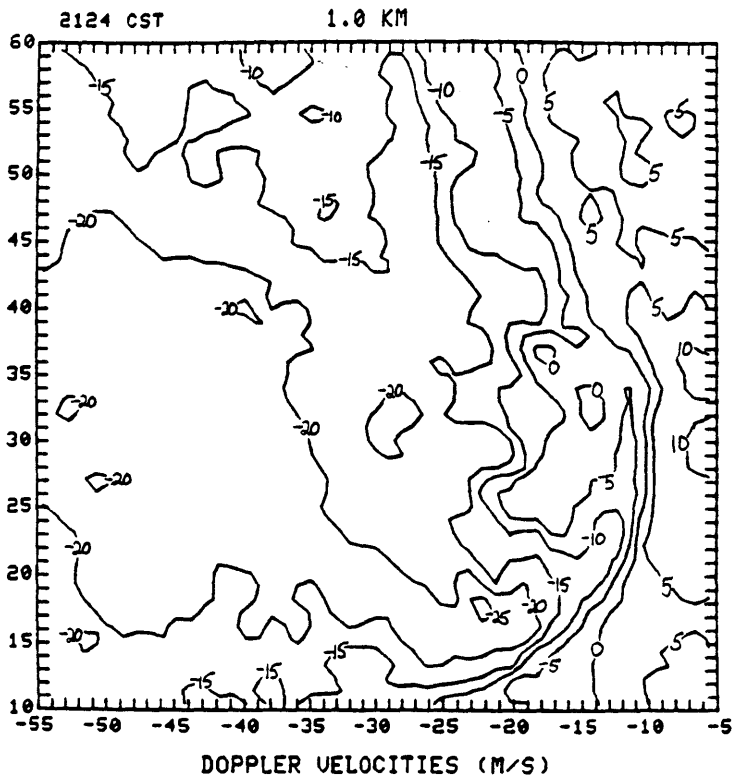
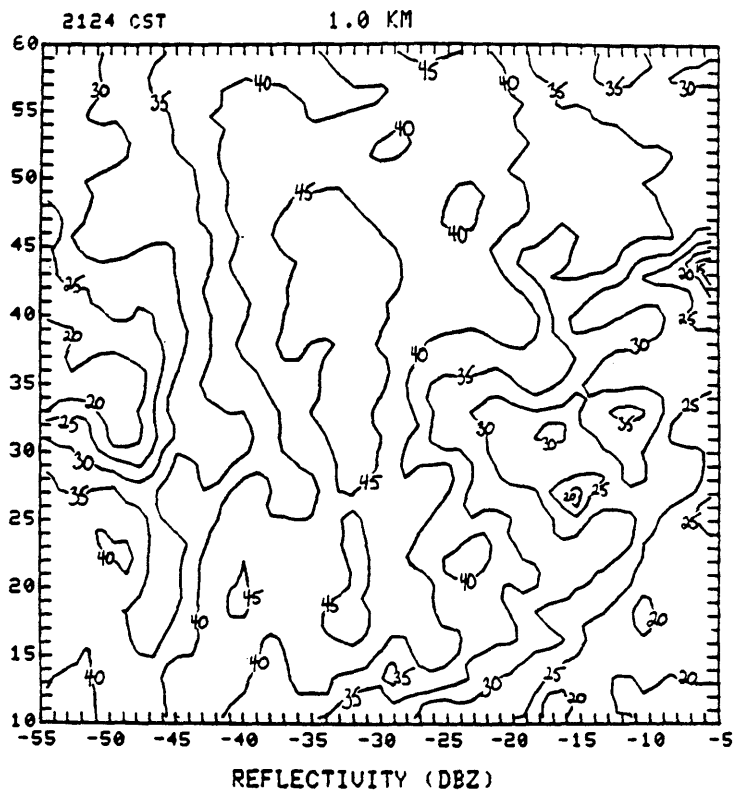


Figure 4-10

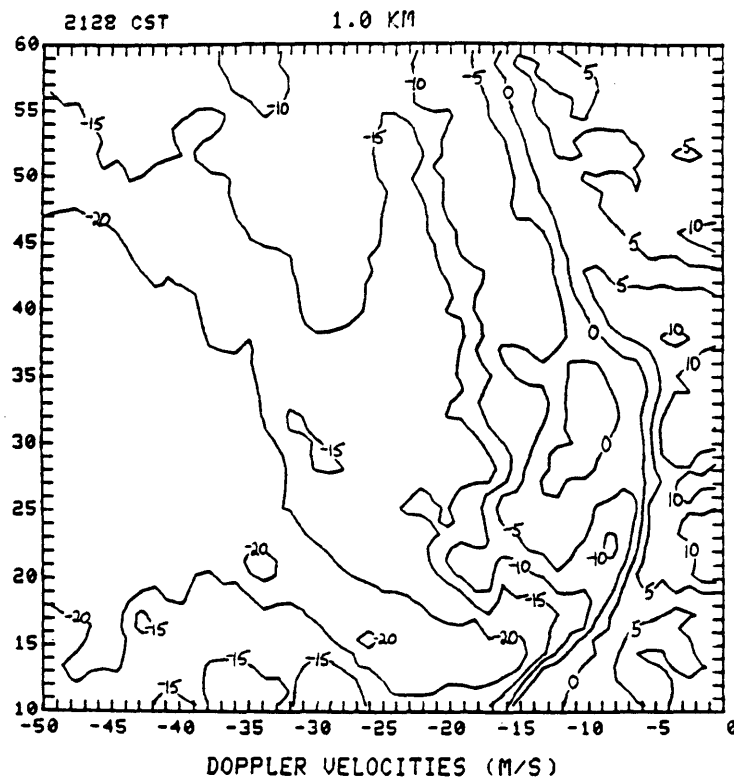
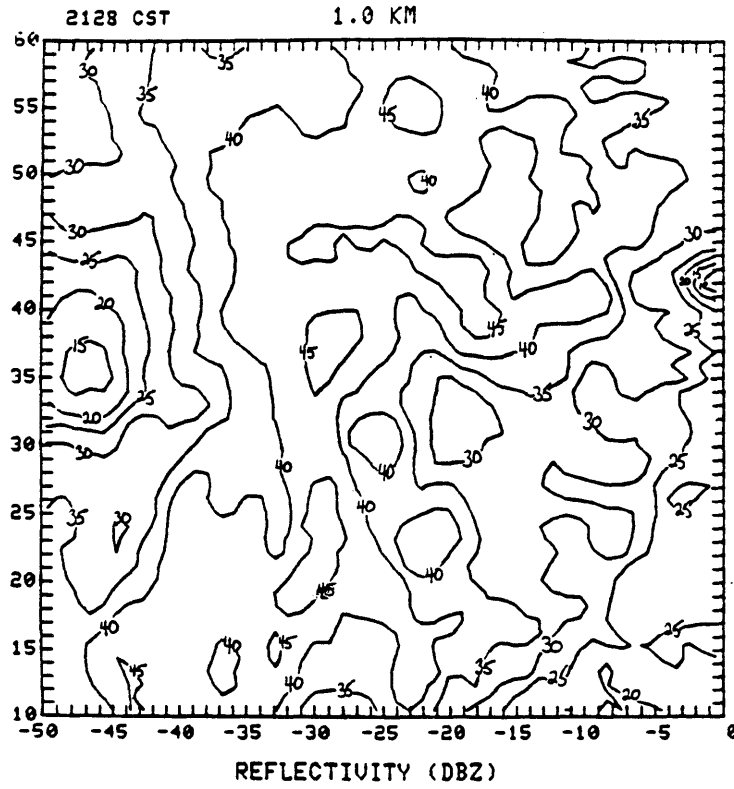


Figure 4-11

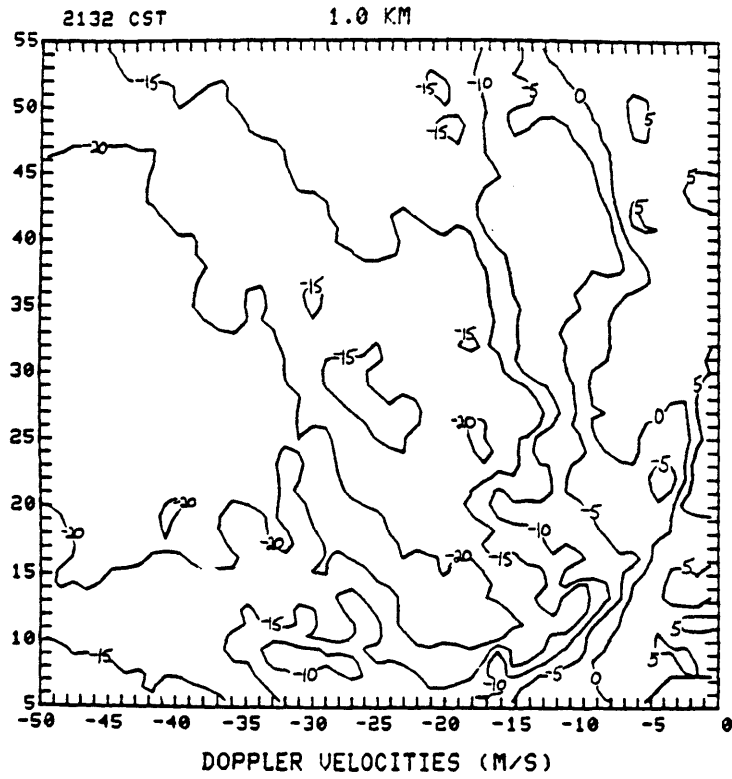
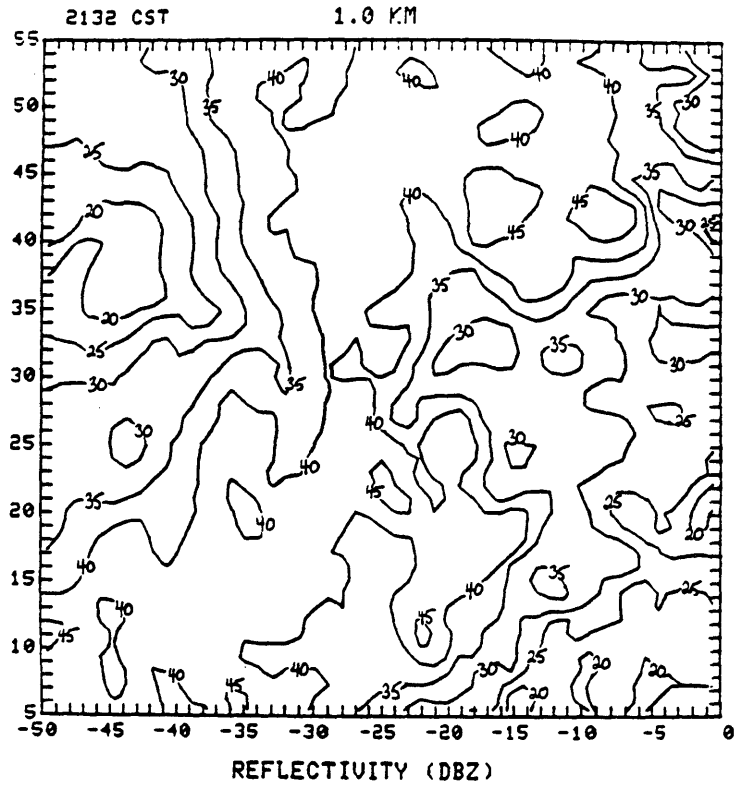


Figure 4-12

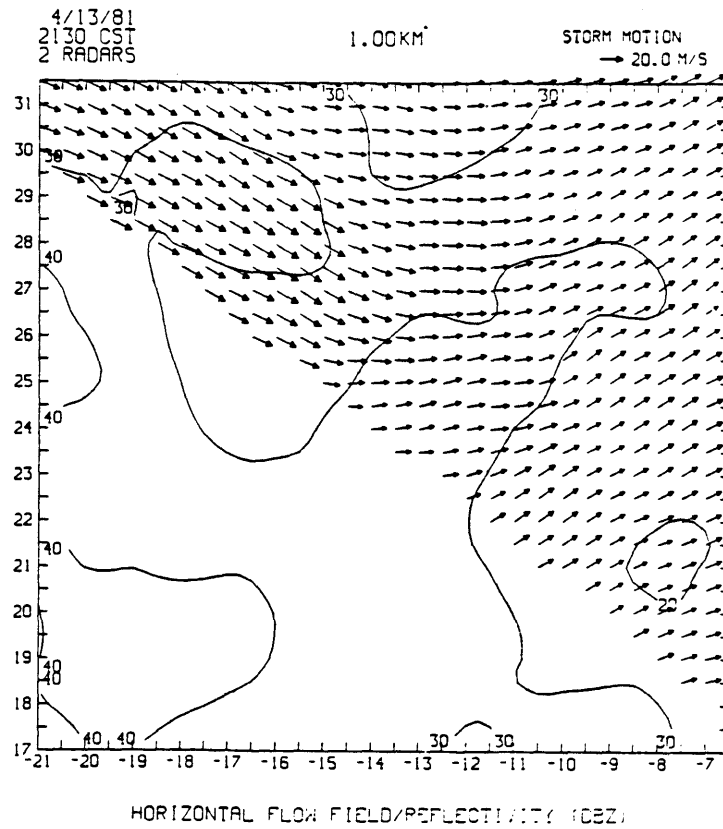


Figure 4-13 The 2-Doppler wind and reflectivity analysis for 2130 CST. The winds in the lower left portion of the domain could not be calculated accurately due to geometric factors.

in the partial wind field from the 2-Doppler radar analysis at 2130 CST shown in figure 4-13. (Details of that analysis can be found in Appendix B). The weak reflectivity region in the west continues to grow and, by 2128 CST, appears to have infiltrated in an anticyclonic manner what was the main core of the cell. The strong echoes in the southern region at 2102 (figure 4-6) have merged with the 40 dBZ region of the remnants of the main cell by 2124 (figure 4-10) and have become part of the "bow". Also, by 2124 the gust front structure is pretty much destroyed. The cell along what was the east-west gust front has grown to 35 dBZ and merged with the main storm fragments by 2128 while the strong reflectivity gradient associated with the north-south gustfront has spread out completely.

B. Side View

Figures 4-14, 4-15, and 4-16 are displays of reflectivity and Doppler velocities on vertical east-west oriented surfaces through the storm at three times (2102, 2106, and 2112 CST) during the occurrence of the downburst. The surfaces are 5 km apart in the north-south direction from $y=20$ to $y=50$ with two extra surfaces added in the vicinity of the downburst ($y=27$ and $y=33$). The isolines intersect the lower surface vertically because the $z=0$ data is taken to be exactly the same as that at $z=0.5$ km.

At 2102 CST (figure 4-14) the storm is still strong, and reflectivities aloft are greater than 55 dBZ at $y=40$ and $y=45$. The northeast-southwest oriented gust front is very clear in the lowest two kilometers from $y=25$ to $y=40$. At $y=33$ the vertical gradient of radial velocity is extremely intense at the front edge of the gust front. Note

the depression in the isodops between $x=-45$ and $x=-50$; the depth of the outflow layer is less at $y=33$ than to the north or to the south of that line. It was in this area that the "hole" appeared in the 45 dBZ contour (refer to figure 4-6).

At $y=40$, north of the gust fronts, the outflow layer is very different. Notice the intense kink in the isolines of both plotted variables at $z=2.5$ km on the eastern edge of the high reflectivity core. This suggests the existence of a strong updraft around which I believe there to be cyclonic motion (see Chapter 5, section B).

Also of interest in figure 4-14(B) are the intrusions of dry air aloft into the storm from the west. These appear at very regularly spaced intervals in the vertical (every 2 km) and suggest a possible wavelike structure. This dry air certainly appears to be furthering the decay of the storm.

At 2106 CST (figure 4-15) a quick glance shows that the storm has noticeably decayed in the last 4 minutes. There are now no areas of reflectivity 55 dBZ or greater. At $y=35$ (figure 4-15(B)) the "head" of the outflow current is very pronounced. This is the area of the occlusion where the gust fronts are merging and also appears to be a region of strong upward vertical motion, as evidenced by the Doppler velocities away from the radar. The downburst has hit the ground by this time as can be seen by the -25 m/s isodop at $y=27$ between the x -coordinates -40 and -35 .

This picture at $y=27$ is interesting for another reason. Both it and the picture for $y=25$ below it show a distinct downward protrusion of dry air from upper levels around $x=-48$. It is difficult to estimate the source height of this downdraft but it appears to be at least 6 km. At

this stage the downdraft appears to penetrate to the 2 km level. Judging just from the reflectivity contours, this formation looks very much like the vertical cross-section from which Fujita (1979) postulated the descent of air from a caved-in overshooting top all the way to the ground. It is also possible that this is an example of the "penetrative downdraft" of Emanuel (1981). At any rate it is clearly separate from the downburst at the leading (eastern) edge of the storm and it appears to be aiding greatly in the rapid decay of this cell.

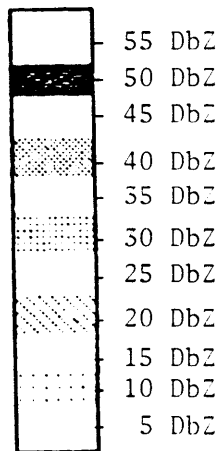
At 2112 CST (figure 4-16) the original downburst is evidenced by the -25 m/s isodop at $y=25$ and $x=-35$. From the surface analysis (DiStefano, 1983) the downburst is known to have crossed $x=-30, y=25$ at 2110 CST. The time discrepancy is due to the use of the midpoint in time to characterize this entire tilt sequence. I suspect that another downburst has occurred at $x=-33, y=35$ because of the strong vertical isodop gradient, the accelerated patch of low level air centered around $x=-30$, and the "hole" or "notch" that has developed in the 40 dBZ contour (refer to figure 4-8).

At this time as well there are downward protrusions of the reflectivity contours, perhaps due to downdraft activity, occurring in every picture from $y=20$ to $y=33$. Notice at $y=30$ there might be a dry thermal (versus a plume) centered around $x=-45, z=4.5$. There is also evidence that some of this dry air has arrived at the surface.

The dry intrusion from the west is clear at the left edge of figures 4-16(A) and 4-16(B). Judging from these pictures this air is moving into the storm cell not only horizontally from the west but vertically from above as well.

Figures 4-14 through 4-16 each consist of 3 separate pages, each with 3 side views of the storm at the specified time. Heavy solid lines are isodops labelled in meters/sec. Negative values signify motion toward the radar. Shading represents the reflectivity field in DbZ according to the code below. The abscissa represents the east-west direction and the ordinate, the vertical. Both axes are labelled in km in the NRO coordinate system. The y-coordinate of each picture is noted at the top of each frame.

REFLECTIVITY SHADING CODE



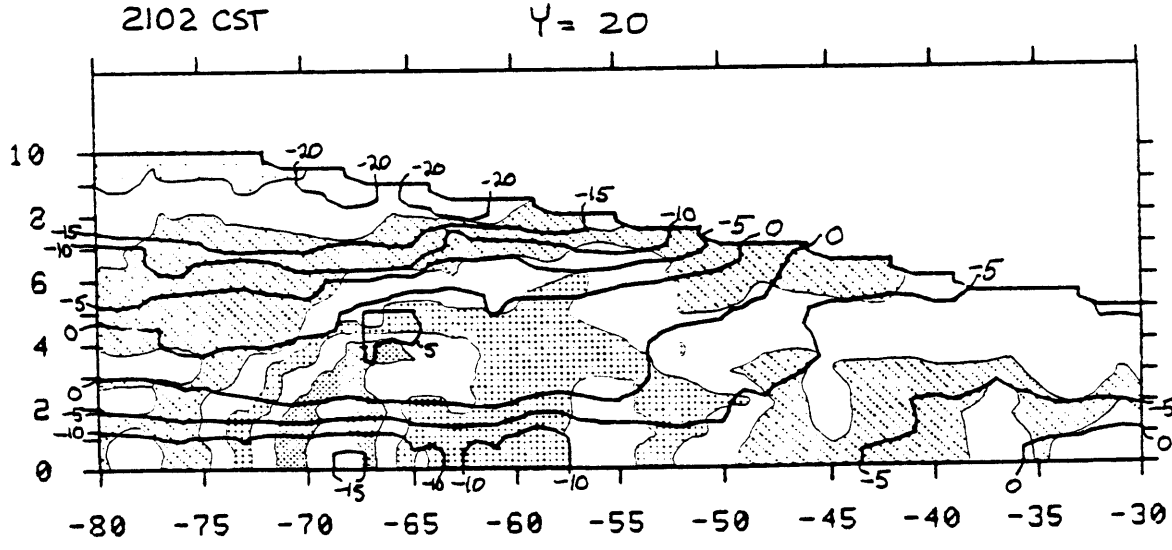
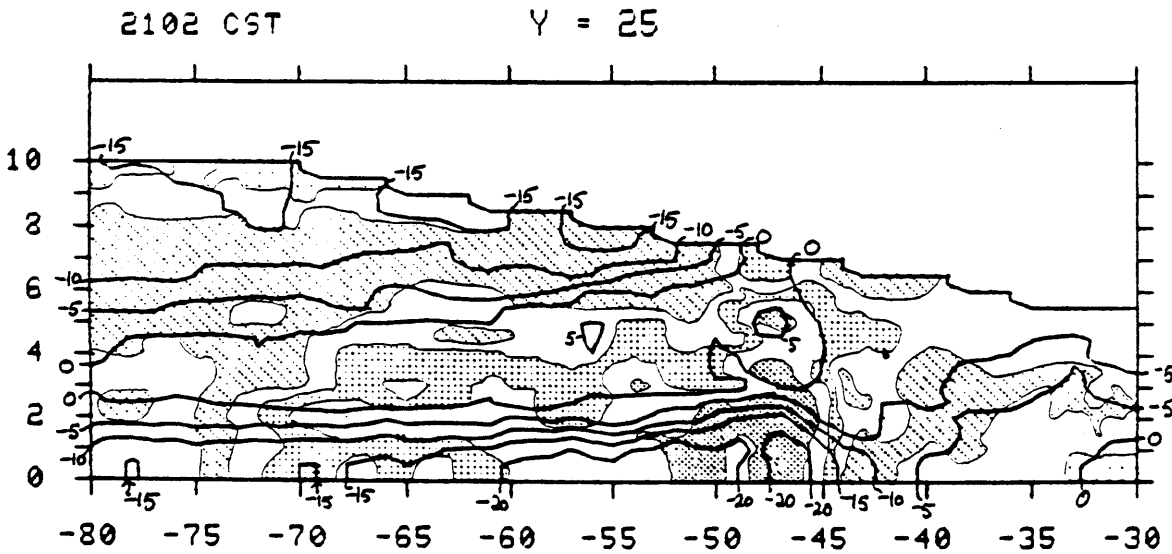
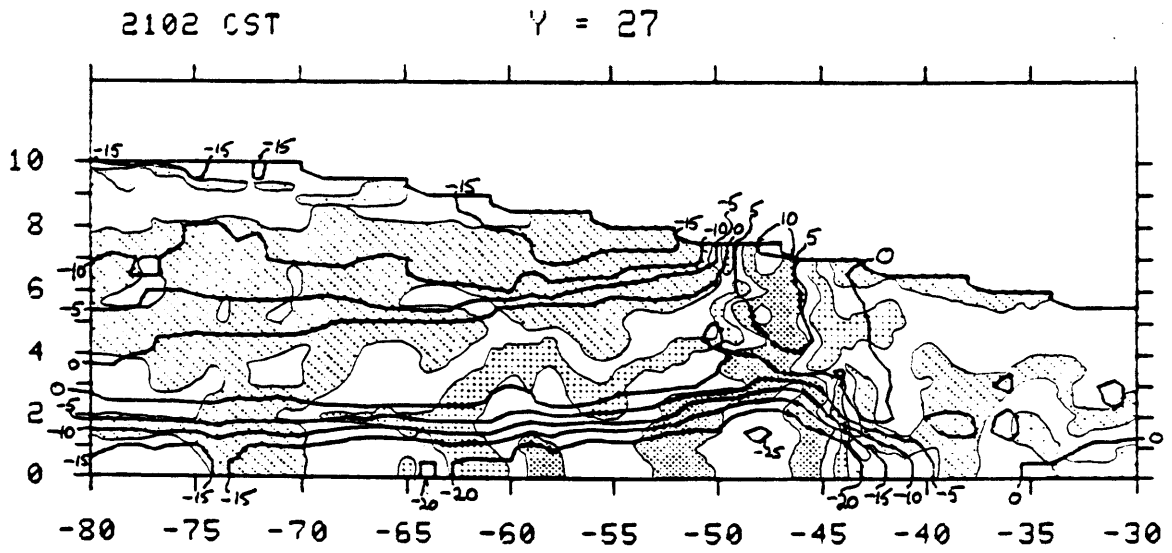


Figure 4-14 A

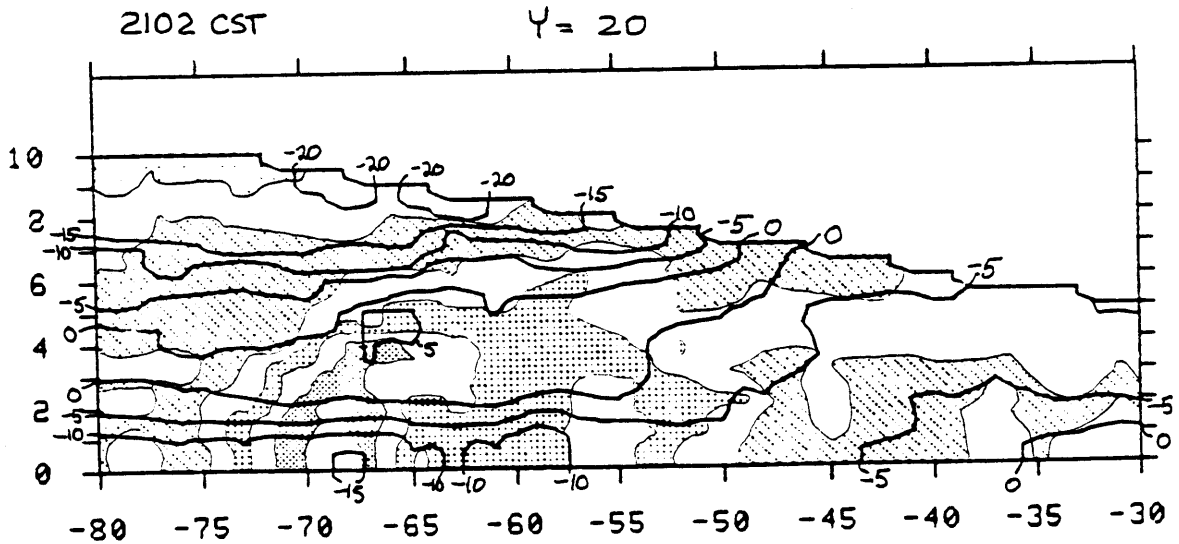
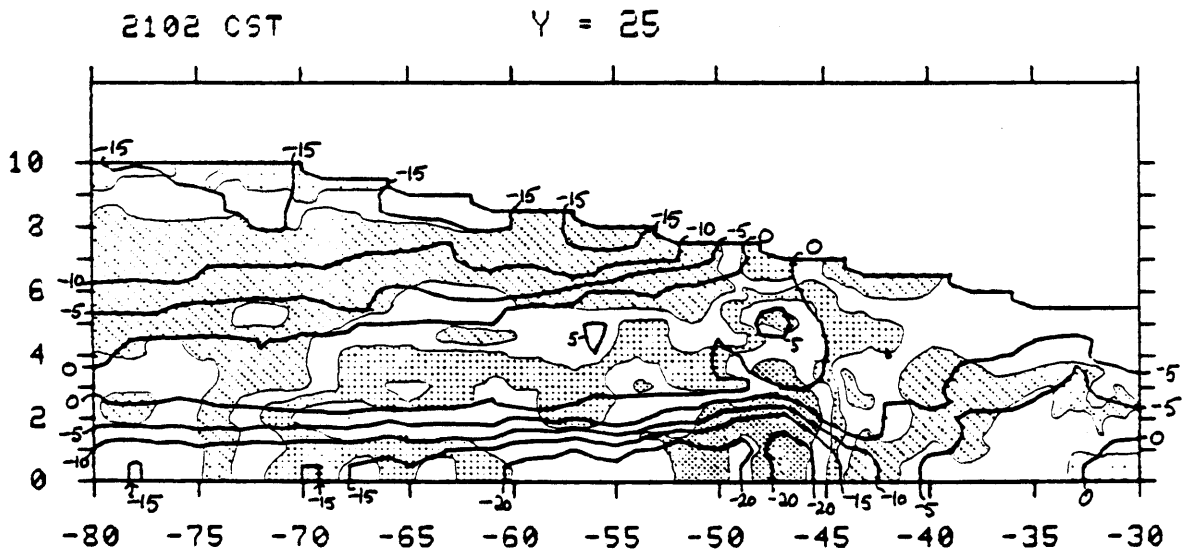
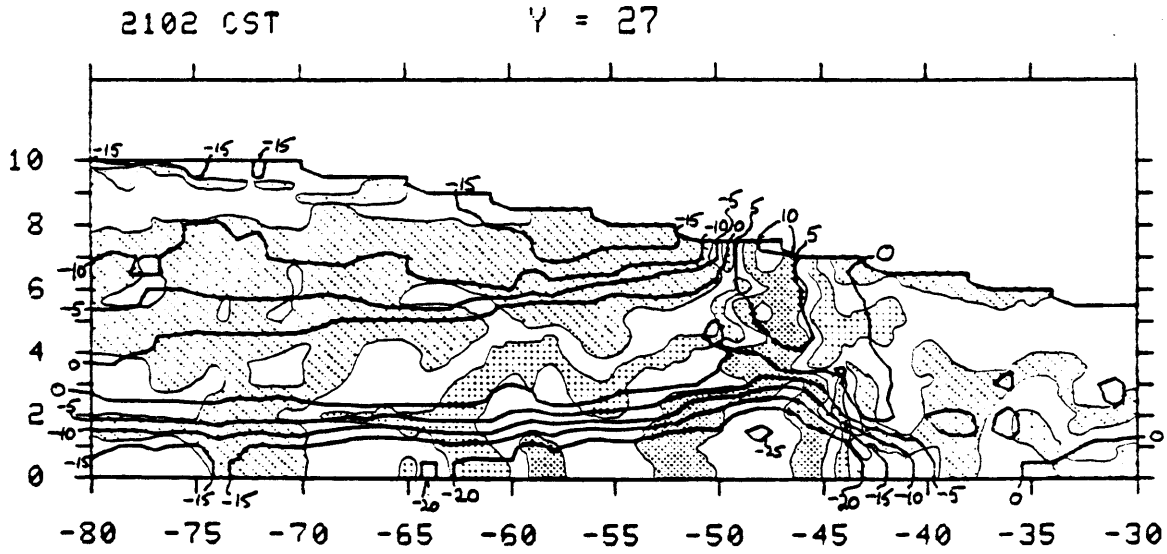


Figure 4-14 A

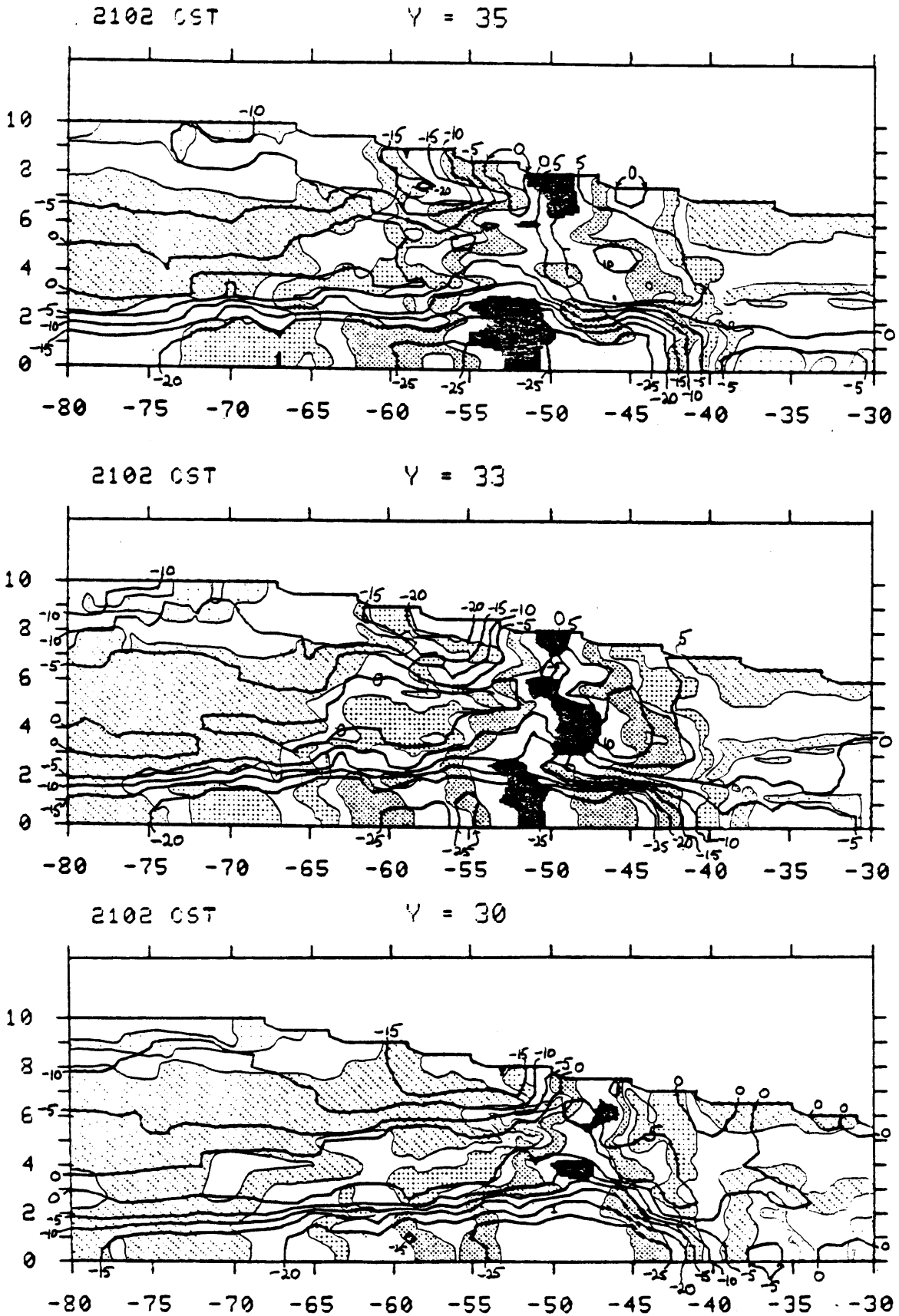


Figure 4-14 B

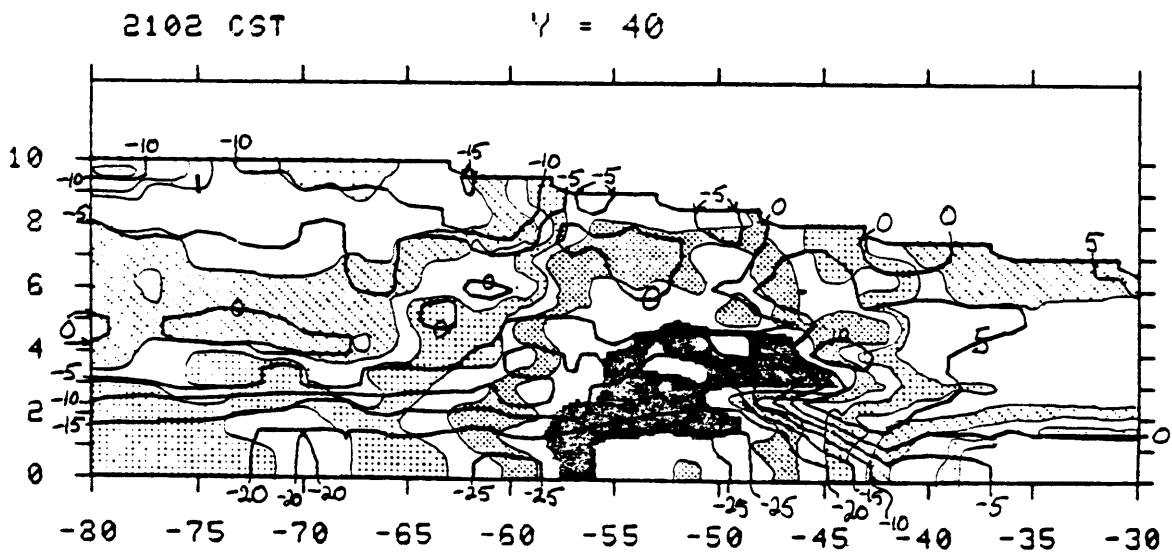
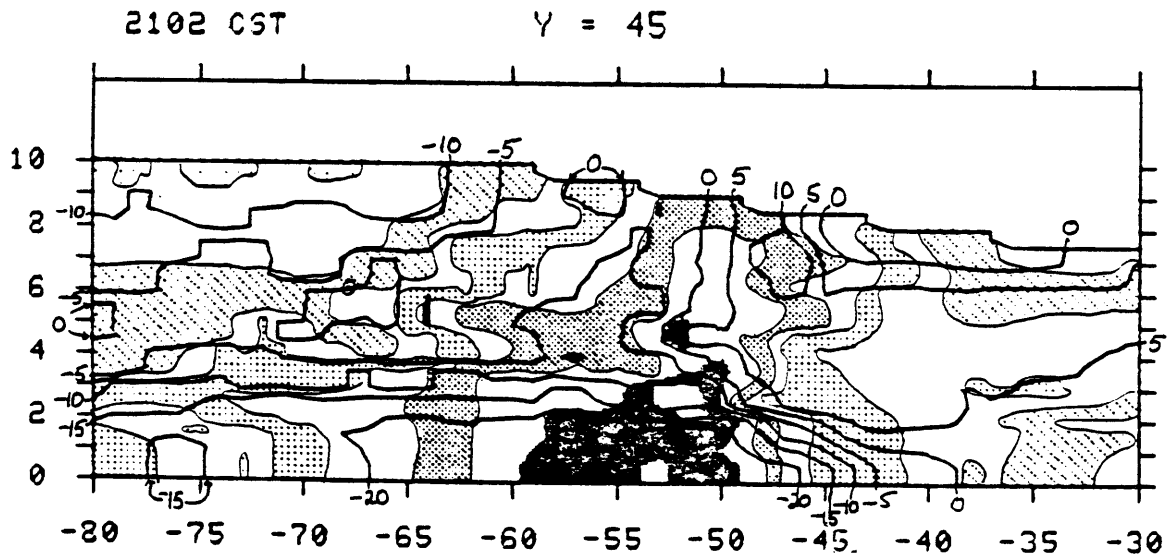
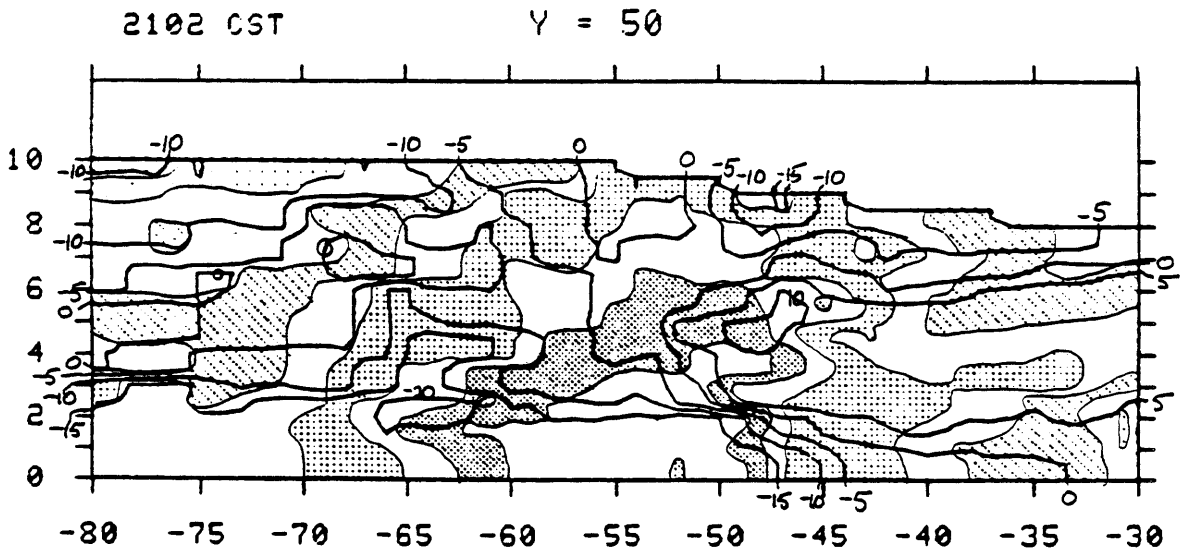


Figure 4-14 C

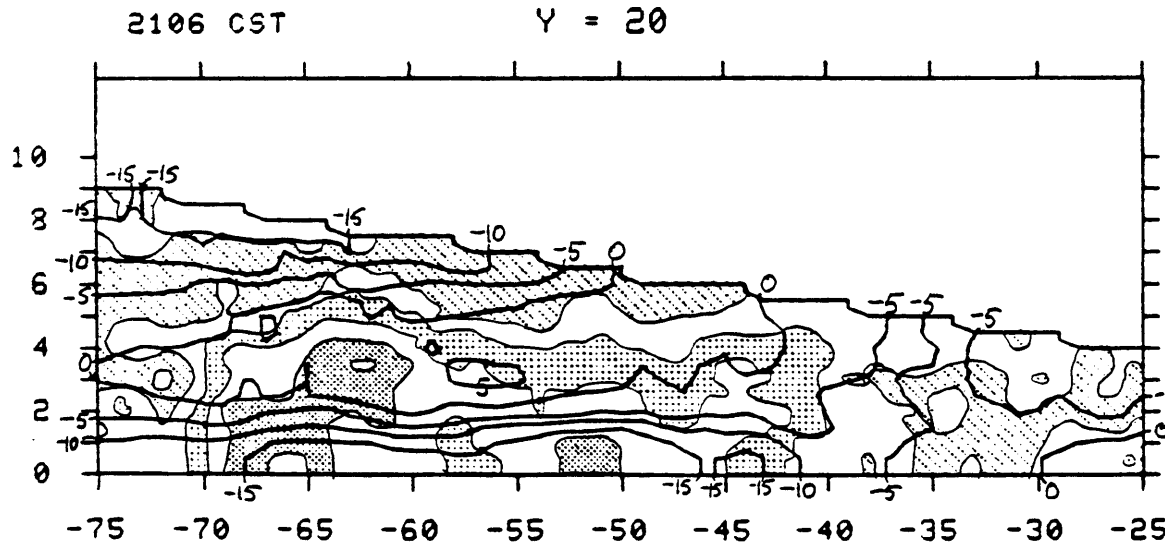
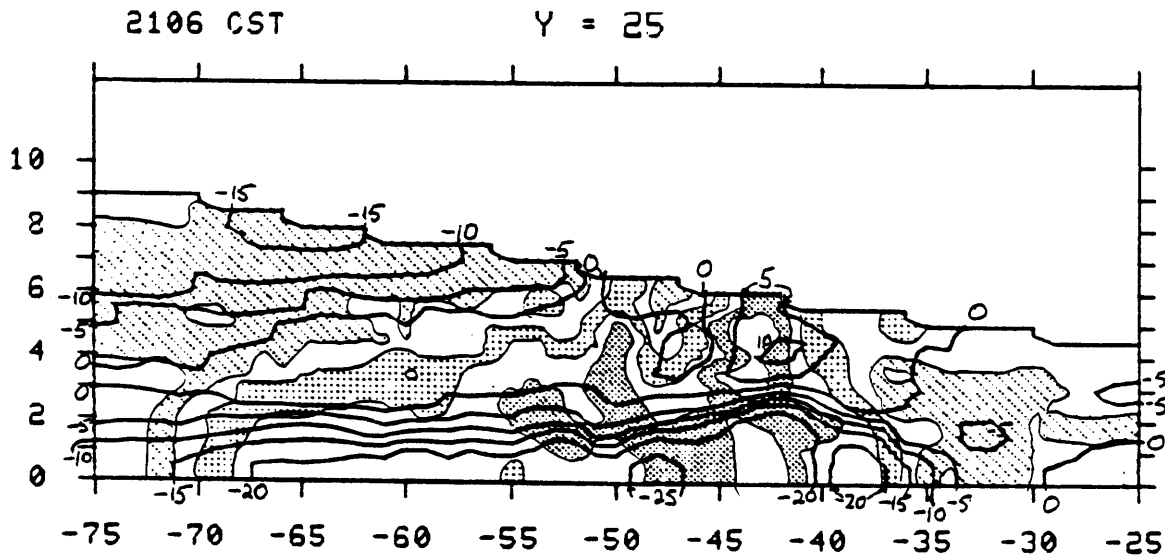
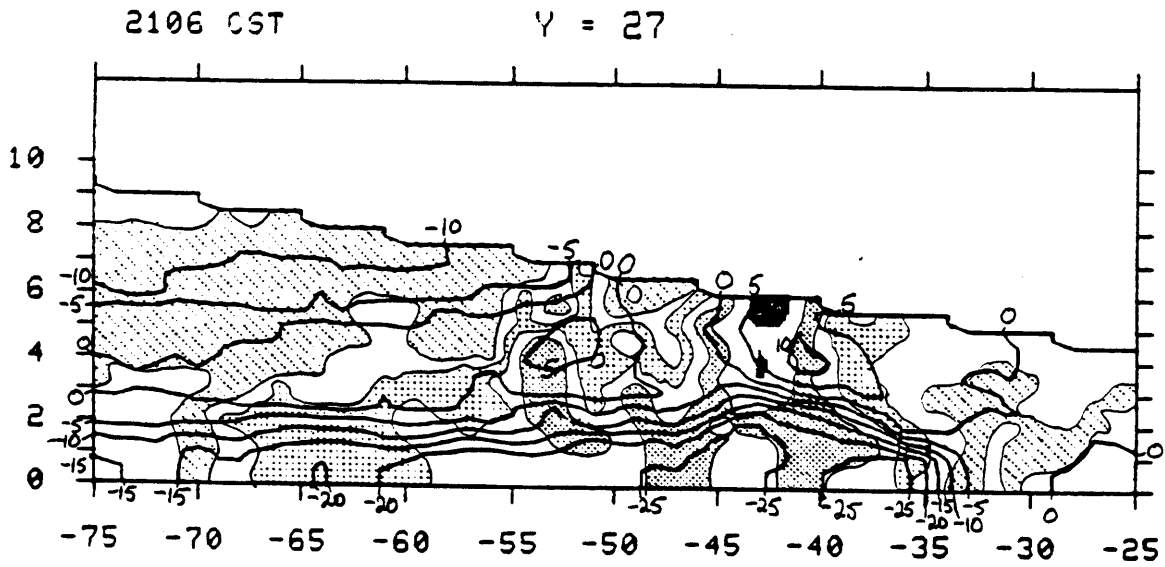


Figure 4-15 A

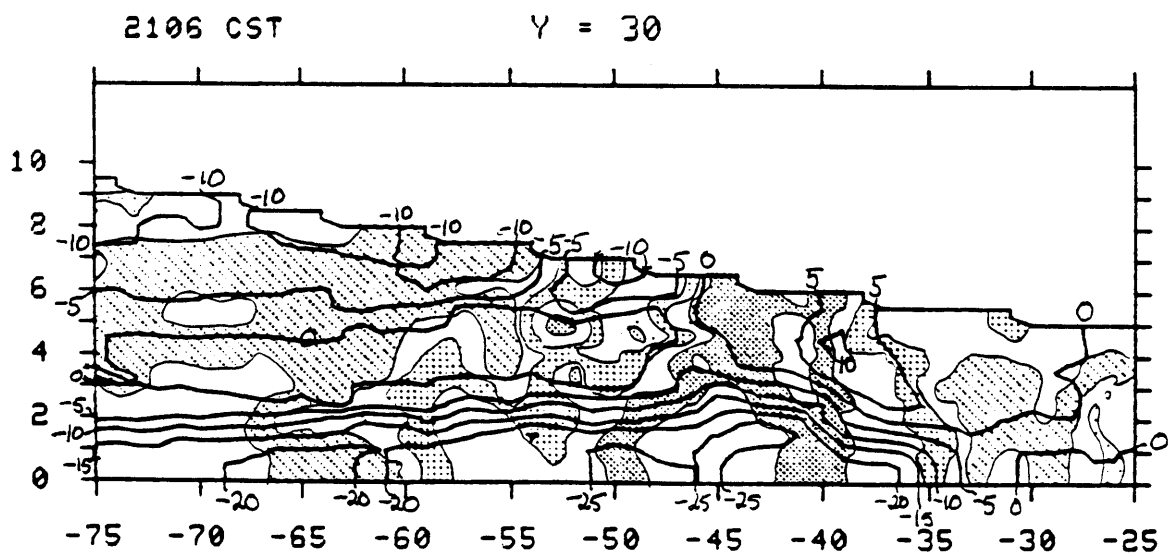
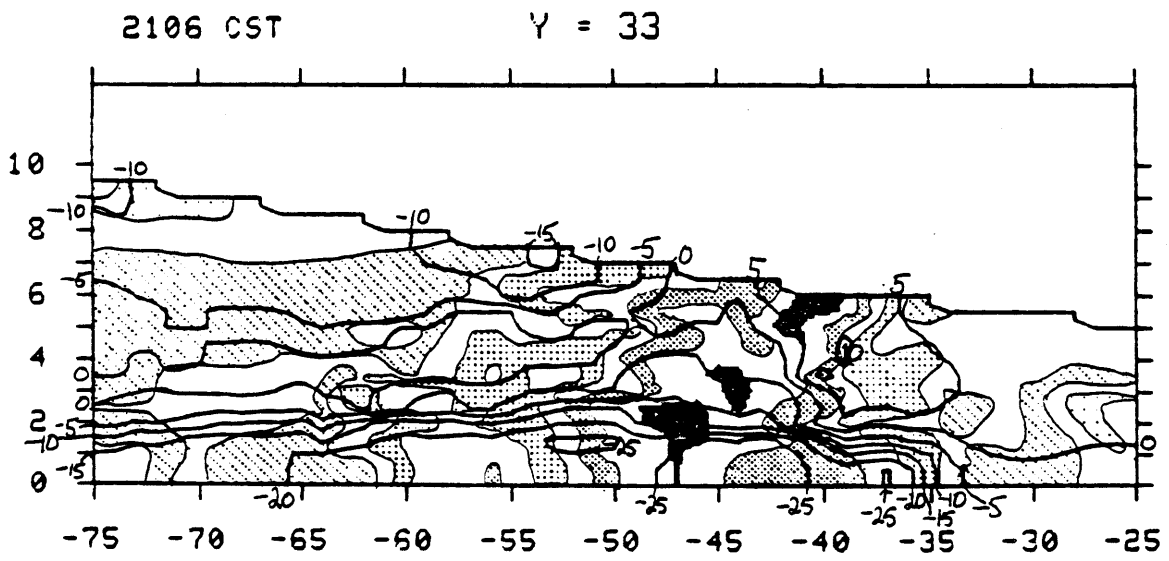
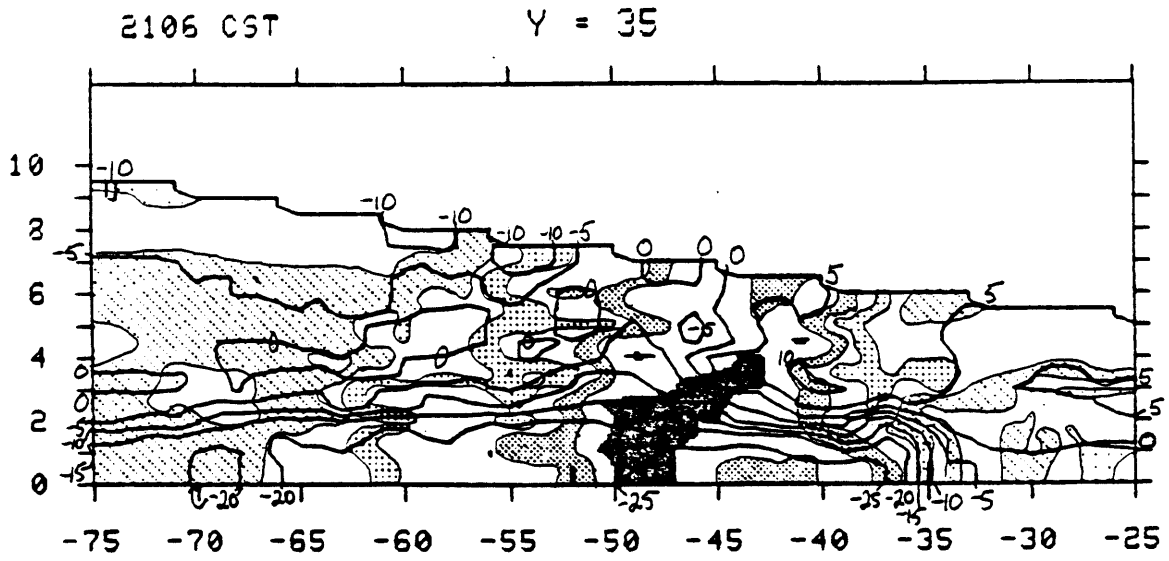


Figure 4-15 B

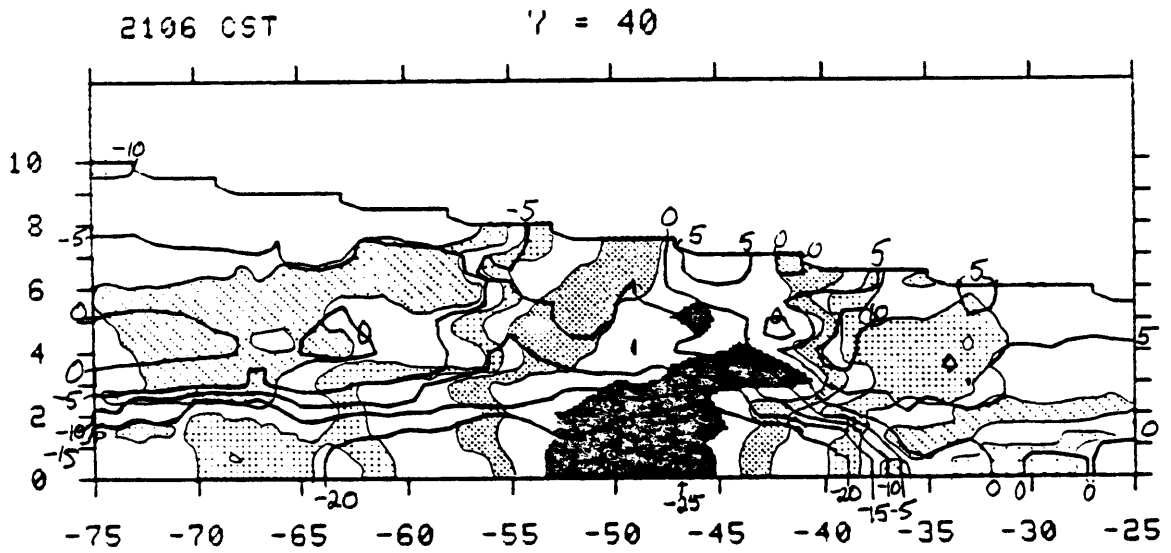
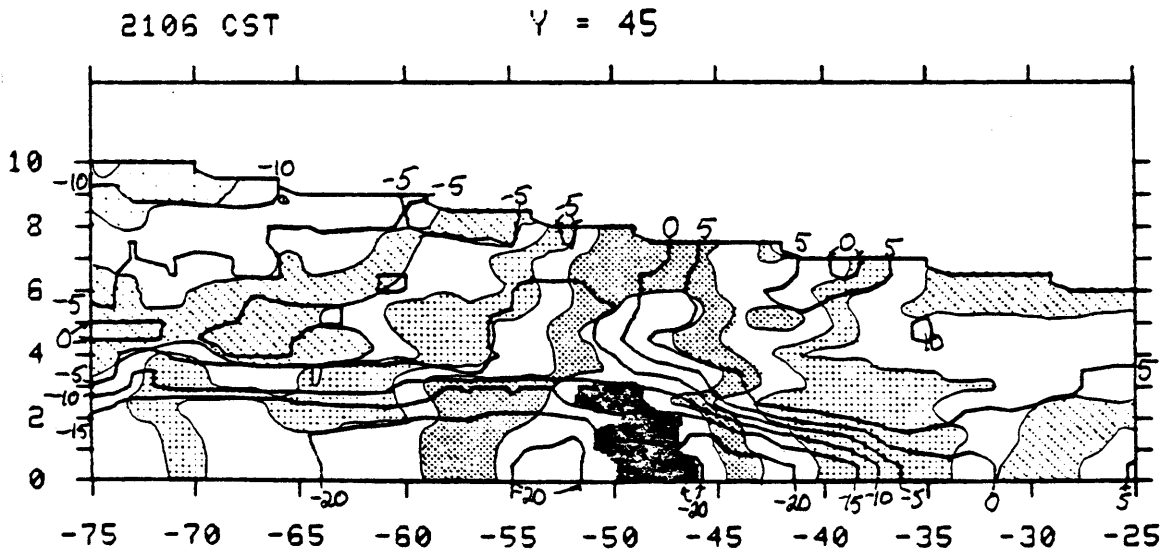
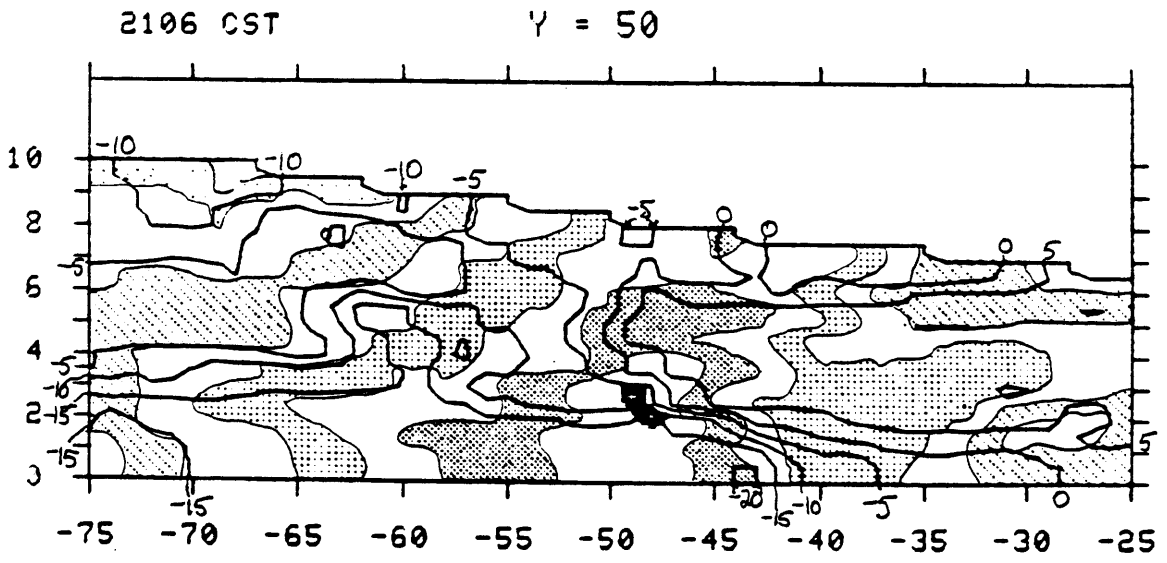
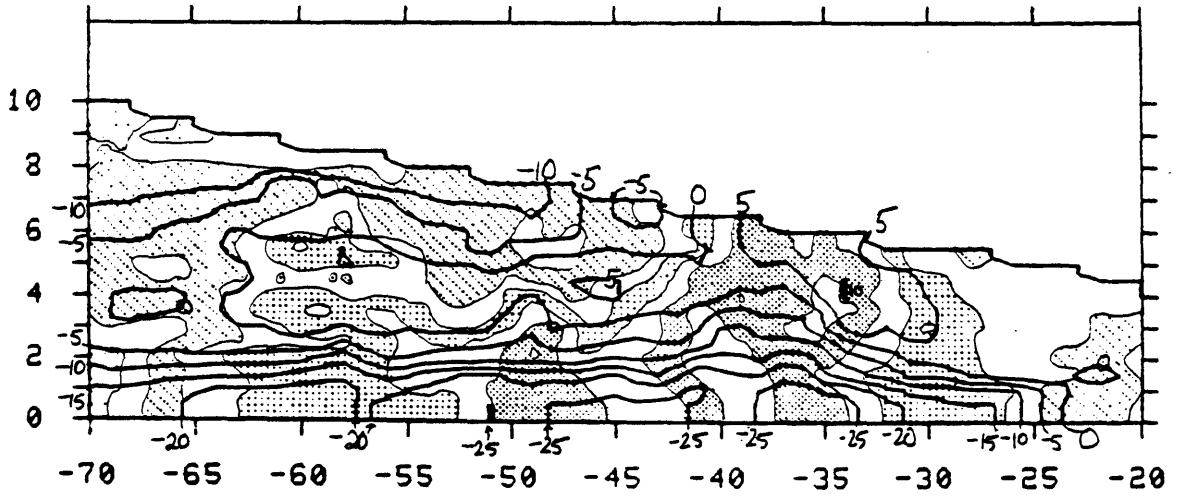


Figure 4-15 C

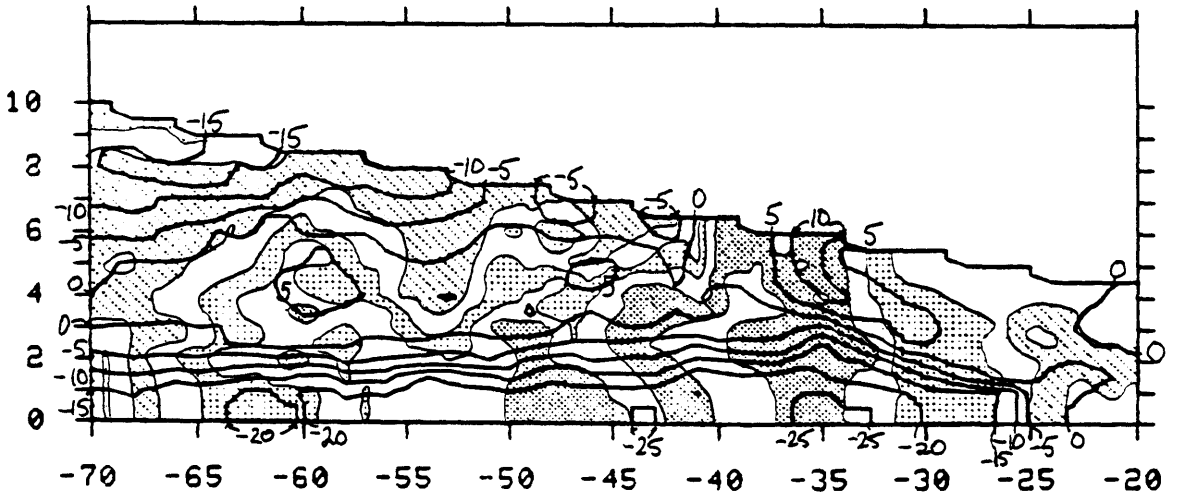
2112 CST

$\gamma = 27$



2112 CST

$\gamma = 25$



2112 CST

$\gamma = 20$

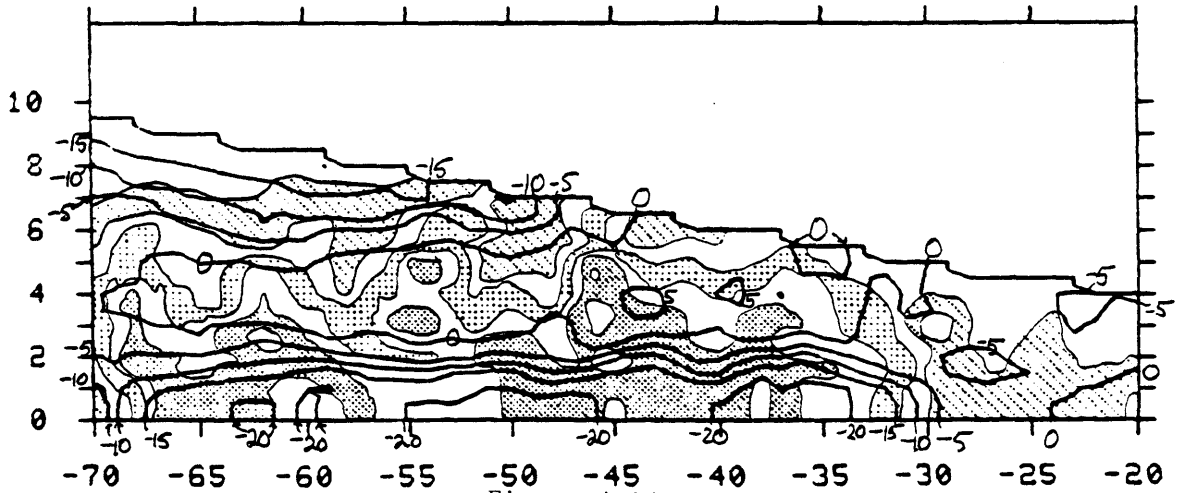
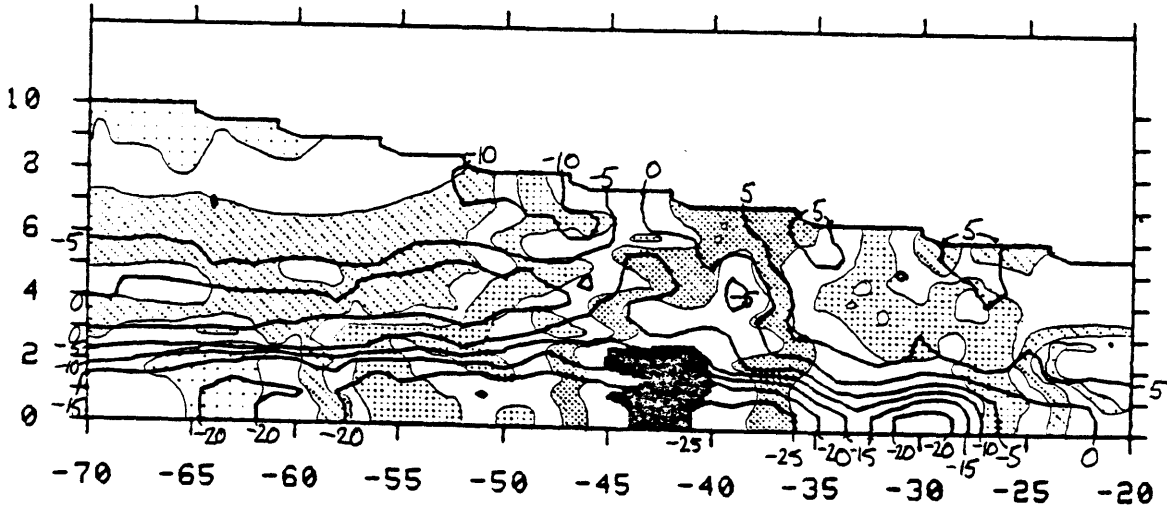
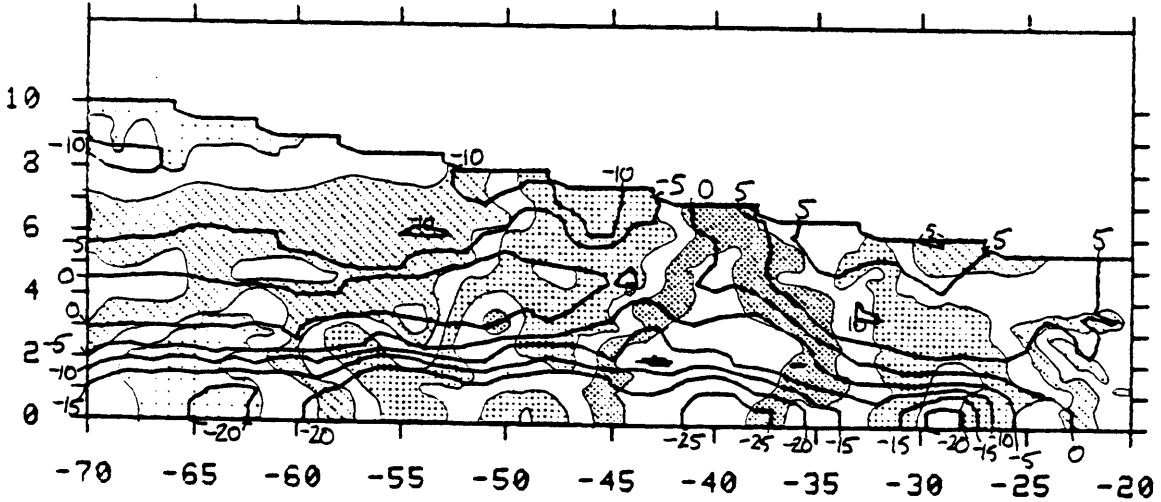


Figure 4-16 A

2112 CST $\gamma = 35$



2112 CST $\gamma = 33$



2112 CST $\gamma = 30$

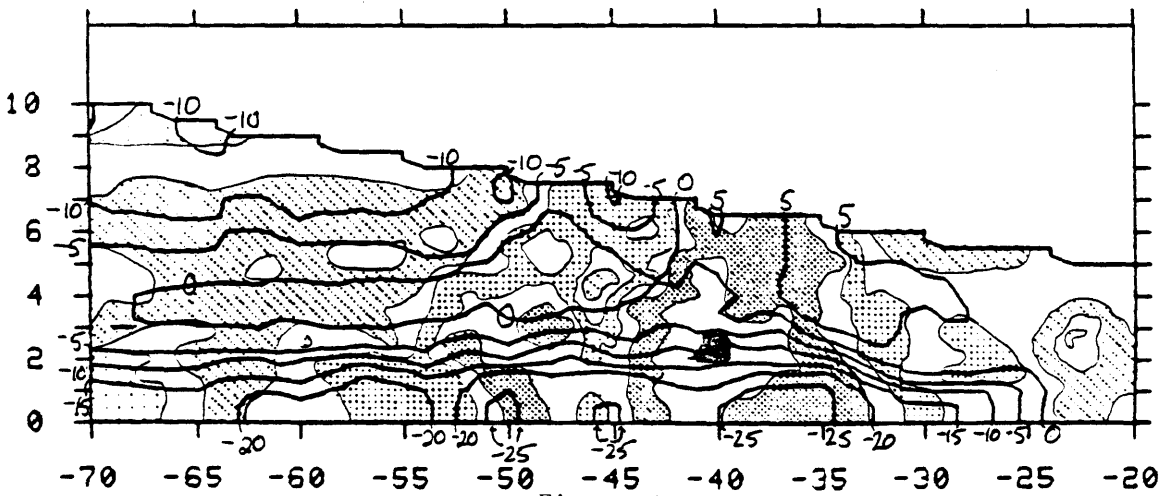
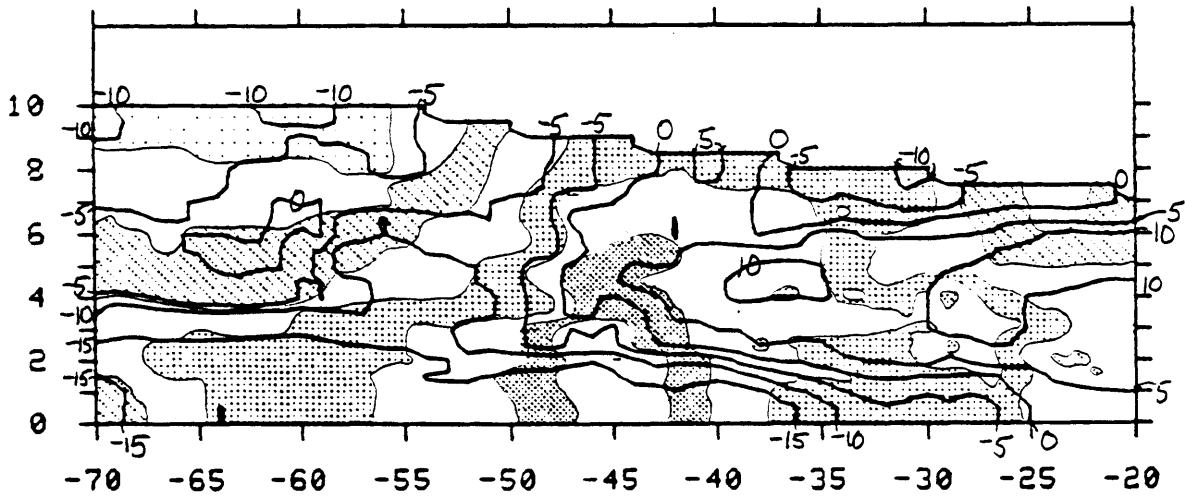


Figure 4-16 B

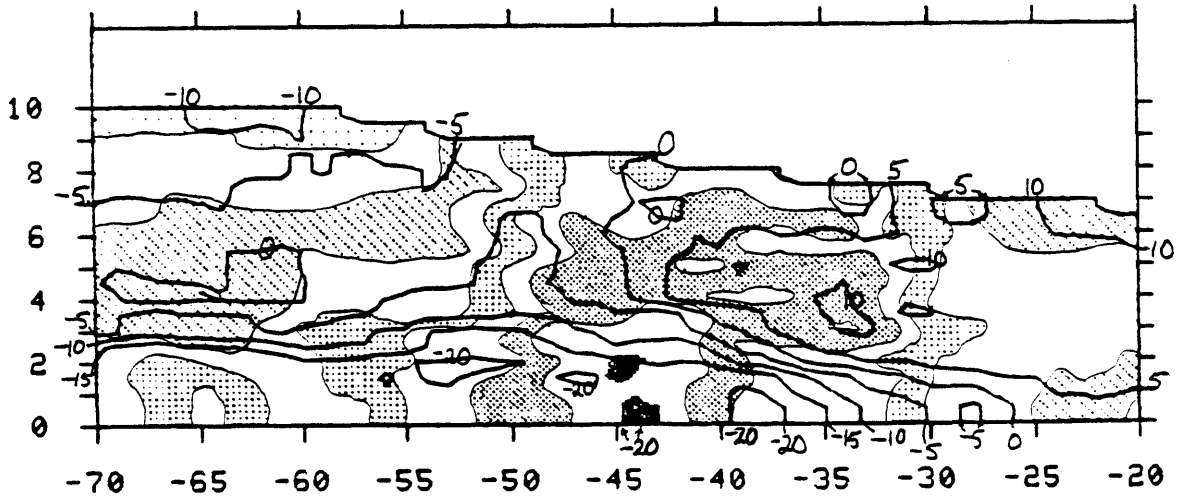
2112 CST

$\gamma = 50$



2112 CST

$\gamma = 45$



2112 CST

$\gamma = 40$

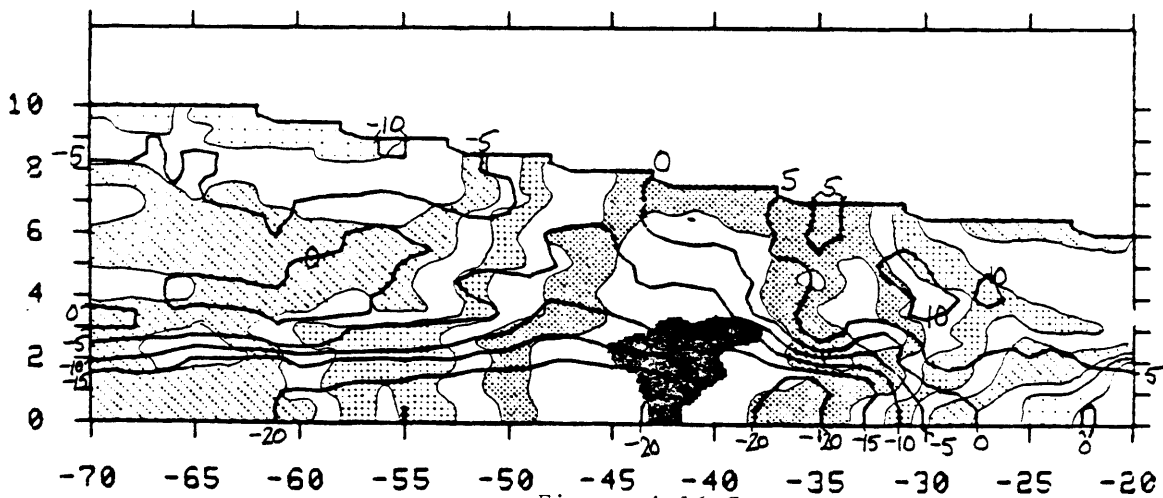


Figure 4-16 C

5. Two Dimensional Wind Field from Single Doppler Radar

In the last fifteen years, Doppler radar has proven to be a very useful tool for investigating storm scale meteorological phenomena. Horizontal wind fields have been successfully and accurately derived using two or more Doppler radars simultaneously. A single Doppler radar can only detect the radial component of the wind field; it does this, however, very accurately and with a resolution of better than one kilometer. Yet it is often the case and will more often be the case when NEXRAD is fully implemented, that data from only one Doppler radar is available for a storm. Since it is very desirable to obtain the full vector windfield it is not surprising that quite a few studies have been done which try, using various additional assumptions and hypotheses about the flow, to derive the two dimensional windfield from detailed single Doppler velocity data.

By far the most common assumption made is that the flow varies linearly around its value at a given point. If the data are collected around a full circle at each elevation angle (Velocity Azimuth Display) the magnitude and direction of the horizontal wind (Lhermitte and Atlas, 1961) as well as the mean convergence and stretching and shearing deformations (Caton, 1963; Browning and Wexler, 1968) can be derived. These techniques have been extended to conical sectors (Easterbrook, 1975) and full volumes (conical sectors or circles at more than one elevation angle) of radar data (Waldteufel and Corbin, 1979), but always the analysis involves the simplifying assumption of linearity or of harmonic variation in space, in which case a highly truncated Fourier series is used to represent the mean wind. These approximations may be

applicable to stratiform rain situations but not to small scale severe storms. The extreme smoothing inherent in those assumptions removes exactly the features of interest.

Another assumption that can be made is that the flow is unchanging in a reference frame attached to the storm. Then scans at different times can be treated as simultaneous scans of the storm by two or more Doppler radars. This could only work if the storm was extremely fast moving so that the time separation between scans was small but the difference in the mean direction of the storm from the radar was large. This technique could not work for a rapidly evolving, rather slowly propagating storm such as the one presented here.

In this thesis a different approach will be taken in deriving the two dimensional horizontal wind field. It can be easily shown (Holton, 1972, Appendix C) that any vector \vec{V} can be written as

$$\vec{V} = \vec{V}_{ND} + \vec{V}_{IR} \quad (1)$$

where \vec{V}_{ND} is a nondivergent vector satisfying

$$\vec{\nabla} \cdot \vec{V}_{ND} = 0 \quad (2)$$

and \vec{V}_{IR} is an irrotational vector satisfying

$$\vec{\nabla} \times \vec{V}_{IR} = 0 \quad (3)$$

The radar measures the radial velocity component in spherical coordinates. This is converted to the radial velocity in cylindrical coordinates by first taking at every point the horizontal component of the Doppler velocity (very close to what is actually measured at low elevation angle) and then interpolating the measurements onto surfaces of constant height. (See Appendix A for more details). Thus the horizontal wind field in cylindrical coordinates is

$$\vec{V} = V_{\theta} \hat{k}_{\theta} + V_R \hat{k}_R \quad (4)$$

where V_R is the known radial component, V_{θ} is the azimuthal component to be derived, and \hat{k}_{θ} and \hat{k}_R are unit vectors in the azimuthal and radial directions, respectively.

Expanding the right hand side of (1) into polar coordinates:

$$\vec{V} = [V_{\theta_{ND}} + V_{\theta_{IR}}] \hat{k}_{\theta} + [V_{R_{ND}} + V_{R_{IR}}] \hat{k}_R \quad (5)$$

A. Three experiments

Three different experiments have been performed. The first experiment makes the assumption that the observed flow is irrotational ($\vec{V}_{ND} \equiv 0$). Thus

$$V_{R_{OBSERVED}} \equiv V_{R_{IR}} \quad (6)$$

An irrotational flow will satisfy (3) which, together with a boundary condition, then defines $V_{\theta_{IR}}$. Writing (3) in polar coordinates gives

$$\left[\frac{1}{R} \frac{\partial}{\partial R} (R V_{\theta IR}) - \frac{1}{R} \frac{\partial}{\partial \theta} (V_{R IR}) \right] \hat{k}_z = 0 \quad (7)$$

Now the angular derivative of $V_{R IR}$ can easily be calculated at all points in R and θ . Since only the radial derivative of the unknown $V_{\theta IR}$ appears in (7) the partial derivative will be an ordinary derivative along a line of $\theta = \text{constant}$. Multiplying by R , (7) can be rewritten

$$\frac{d}{dR} [R V_{\theta IR}] = f_1(R, \theta_0) \quad (8)$$

along $\theta = \theta_0$, where θ_0 is a radial line and f_1 is the known angular derivative of V_R which can be thought of as a forcing function. The integration is a simple "marching" problem and requires only one boundary condition. I have chosen to specify $V_{\theta IR}$ at the inner line of constant radius, labelled C in figure 5-1, and integrate away from the radar. Alternatively, one could specify $V_{\theta IR}$ on line D in figure 5-1 and integrate toward the radar, although because the flow appears to be more quiescent along C it may be easier or less crucial to guess at the boundary condition there.

The second experiment makes use of the assumption that the observed windfield is nondivergent ($\vec{\nabla}_{IR} \cdot \vec{v} = 0$). Now the observed radial flow is defined as the radial component of the nondivergent flow. This flow will satisfy (2) which, with an assumed boundary condition, defines $V_{\theta ND}$. Following a similar line of reasoning to that used in deriving (8), the equation to be integrated in this experiment is

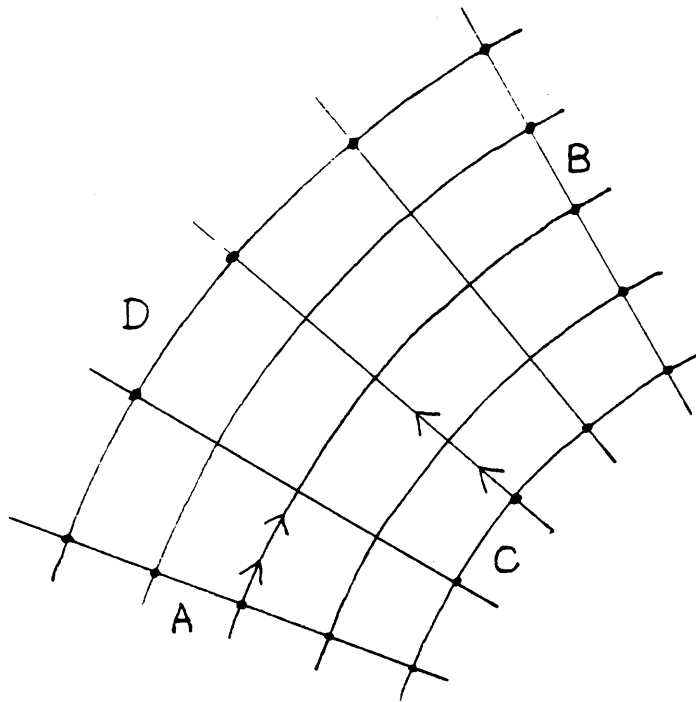


Figure 5-1 The polar grid used in deriving V_{θ} .
Integration proceeded from A to B
along lines of constant radius and
from C to D along radial lines.

$$\frac{d}{d\theta} [V_{\theta ND}] = \gamma_2(R_0, \theta) \quad (9)$$

where R_0 is a line of constant radius. $V_{\theta ND}$ was specified along A in figure 5-1 and the integration was done clockwise along lines of constant radius. Again, the integration could have been started along B and proceeded counter clockwise.

The boundary condition used at all altitudes shown in both experiments was a 6 m/s southerly wind chosen to correspond to the synoptic scale flow in the prestorm environment. This condition was imposed on V_{θ} only; in all cases the observed V_R was used.

Calculations of the horizontal divergence and the vertical vorticity of the 2-Doppler derived winds at 1.0 km are presented in figure 5-2 for the 2045 CST windfield (figure 5-4) and in figure 5-3 for the 2130 CST windfield (figure 4-13). They show that the low-level flow, at least at these times, is both rotational and divergent; the vorticity and divergence of the actual windfields are roughly comparable. Calculations by Ray (1976) of the vorticity and divergence in tornadic storms also show this to be the case. Thus the assumptions that the observed flow is either irrotational (experiment 1) or nondivergent (experiment 2) are clearly both wrong. The premise behind the third experiment is that they are wrong by roughly the same amount, that is, that they represent two extremes between which the real flow lies.

The third experiment, then, combined the first two to make a more "realistic" windfield which had both vorticity and divergence:

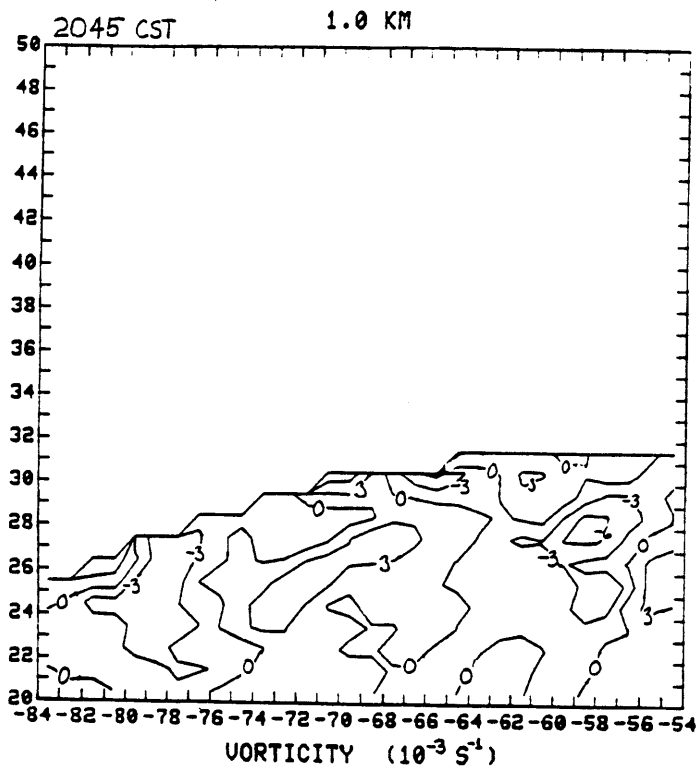
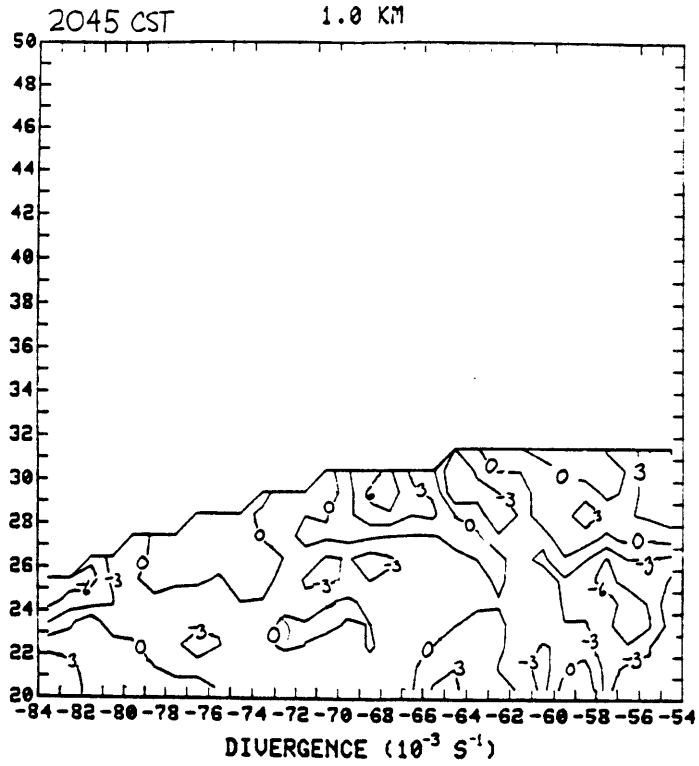


Figure 5-2

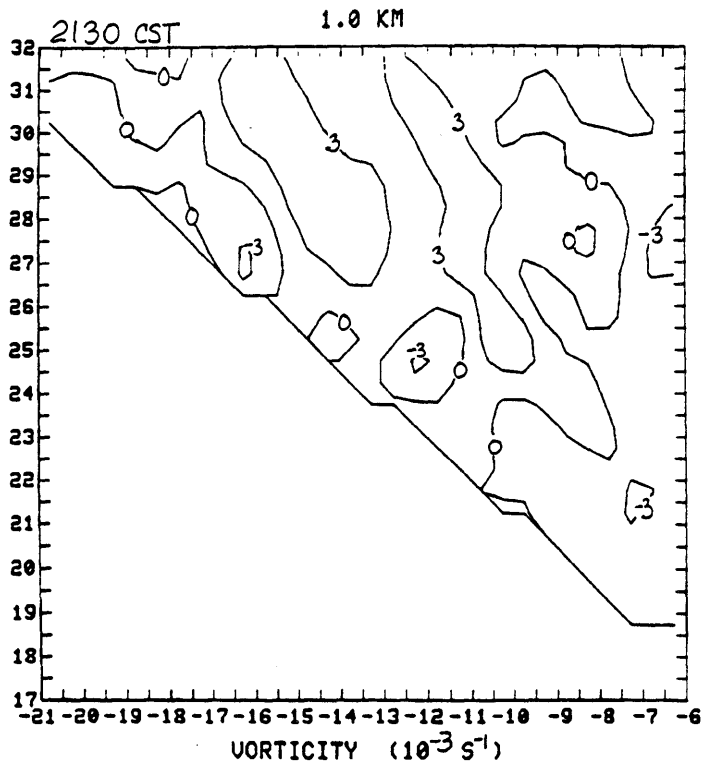
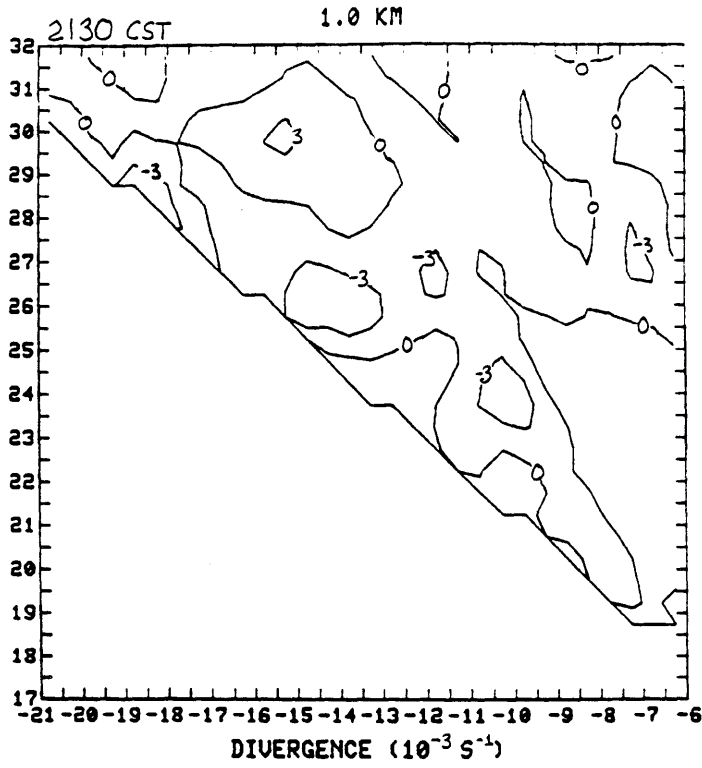


Figure 5-3

$$V_R = V_{R_OBSERVED} \quad \text{and} \quad V_\theta = \frac{1}{2} V_{\theta_IR} + \frac{1}{2} V_{\theta_ND} \quad (10)$$

Actually, this windfield is not realistic either; a windfield simulated in this way would correspond to the actual windfield only if the flow were everywhere constant. (In that case the division of the flow into irrotational and nondivergent components would be nonunique and basically useless.)

Features of the "NONDIVERGENT" and "IRROTATIONAL" windfields shown in figures 5-6 through 5-13 will not be discussed in detail although I do think they are worth examining. The windfields derived in the third experiment are presented and discussed in section B of this chapter. Even though they are known to be unrealistic, I believe that the results of the third experiment are more useful for recognizing characteristic flow patterns and inferring storm structure than simple contour maps of Doppler velocities, and that they qualify as valuable observational tools. Before the discussion of these windfields, however, a few more comments on the accuracy of these experiments are in order.

Accuracy

It is very difficult to get an estimate of the accuracy of the irrotational versus nondivergent assumption. A very rough qualitative comparison can be made at 2047 CST, at 1.0 km, between the partial windfield from the 2-Doppler analysis (figure 5-4) and the derived winds from single Doppler radar (figure 5-6). Notice that these latter wind fields are shown in 50 km² boxes while the 2-Doppler winds are shown in 30 km² boxes. (Appendix B contains more information on the

2-Doppler analysis.) Also, the reflectivity field is contoured every 10 dBZ but is unlabelled in the displays of the single Doppler winds. The values of reflectivity can be found by referring to the figures in chapter 4.

At least in this limited area it appears that the nondivergent approximation is somewhat more realistic than the irrotational approximation. It captures small scale (5 km) wavelike changes in windspeed and direction which are probably real. However, the divergent outflow and in particular the northerly component of the wind is better captured in the irrotational windfield. Figure 5-5 is included for comparison although it is known to contain unacceptably large errors in all but the lowest third of the diagram. Again, the resemblance to the nondivergent flow is qualitatively stronger than to the irrotational flow. This may be partly because the synoptic scale flow itself is quasi-nondivergent.

The accuracy of the boundary condition and of the numerical integration scheme also needs to be considered. As was stated earlier, the sensitivity of the derived windfield to the boundary condition on V_{θ} is small. A boundary condition of $V_{\theta}=0$ was imposed and the flow was compared with that derived using a boundary condition of $V_{\theta}=6$ m/s. The influence of the boundary condition was apparent close to the boundary but was negligible more than 10 to 15 km away. Thus the boundary condition will not cause large errors if it can be applied where the flow is either known accurately or where it is basically featureless. There is, however, a trade-off. Removal of the boundary from the vicinity of the depicted flow lengthens the path along which the integration must proceed.

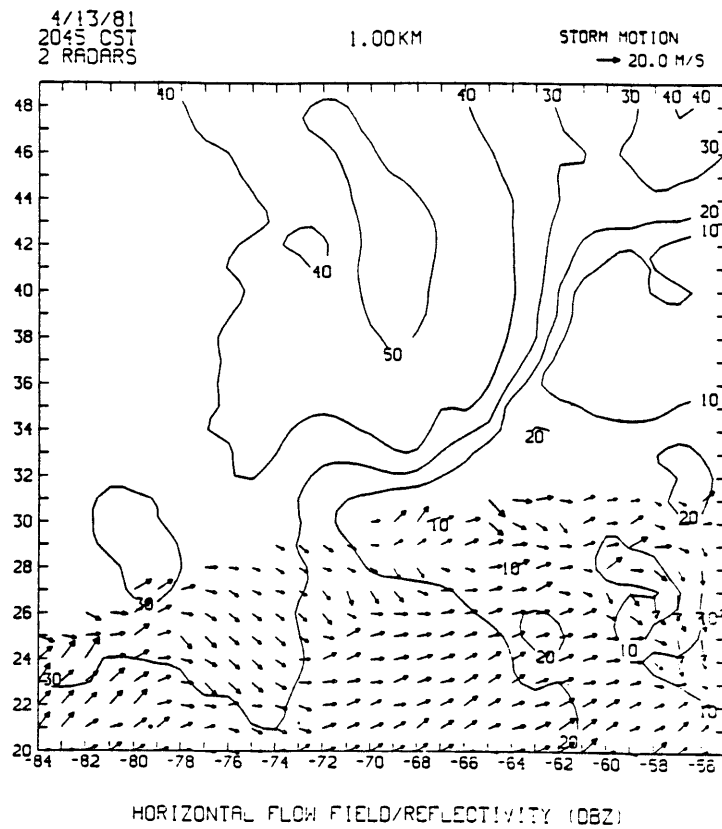


Figure 5-4 The 2-Doppler wind and reflectivity analysis for 2045 CST. The winds in the upper portion of the domain could not be calculated accurately due to geometric factors.

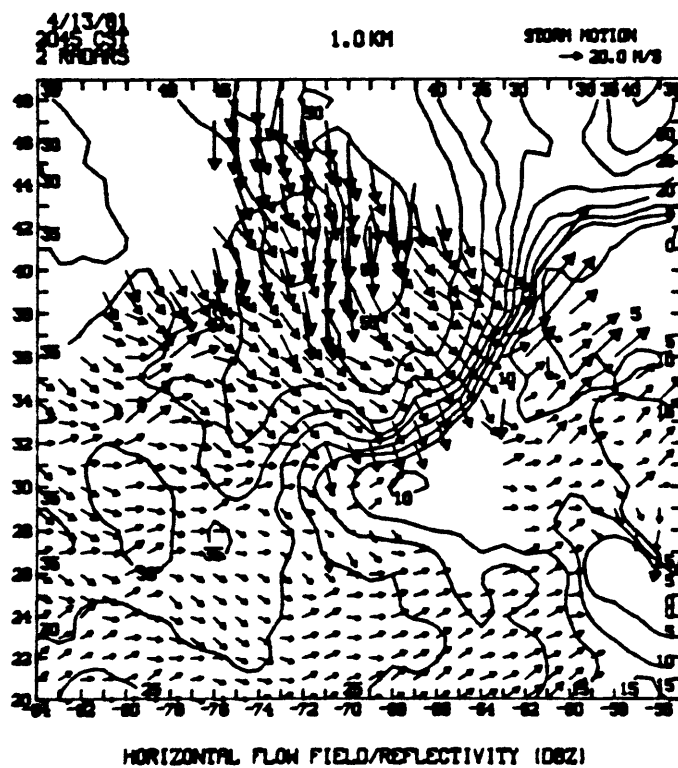


Figure 5-5 The 2-Doppler wind and reflectivity fields from a trial run. All but the lower third of the diagram contains errors known to be unacceptably large. This picture is included for qualitative consideration only.

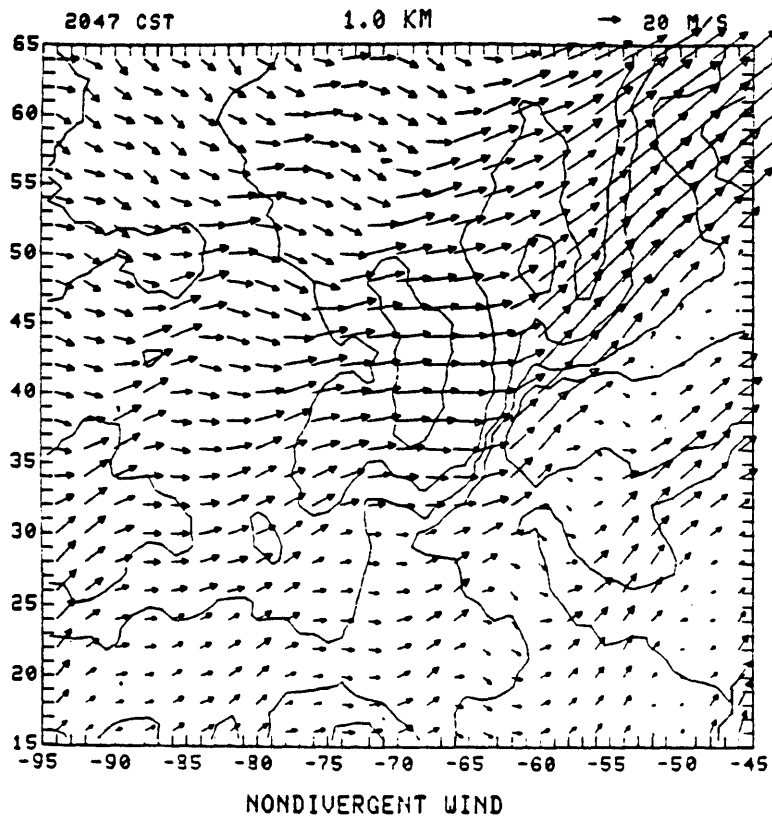
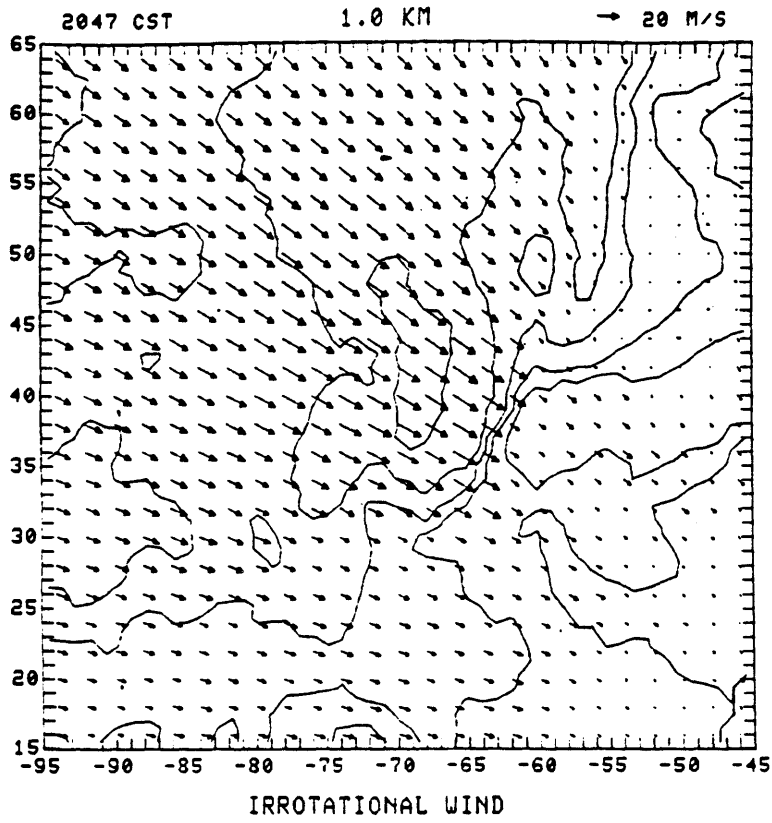
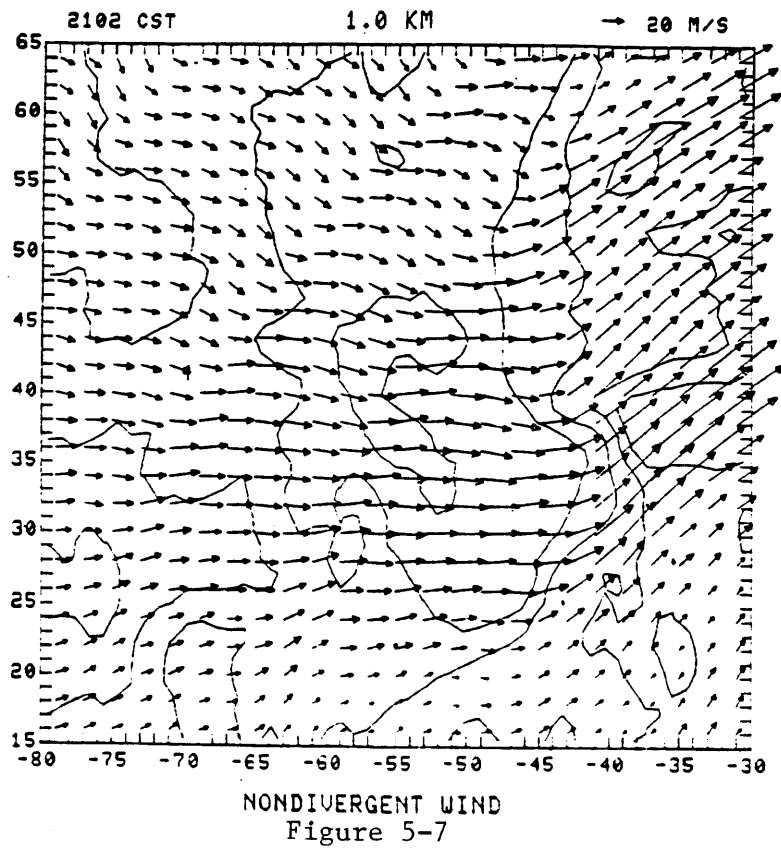
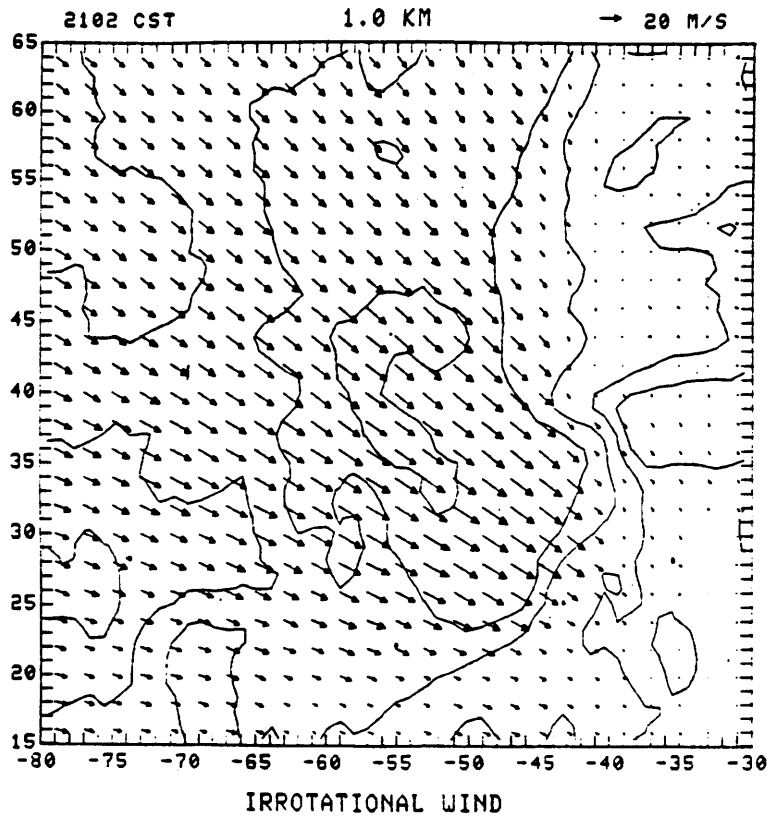


Figure 5-6



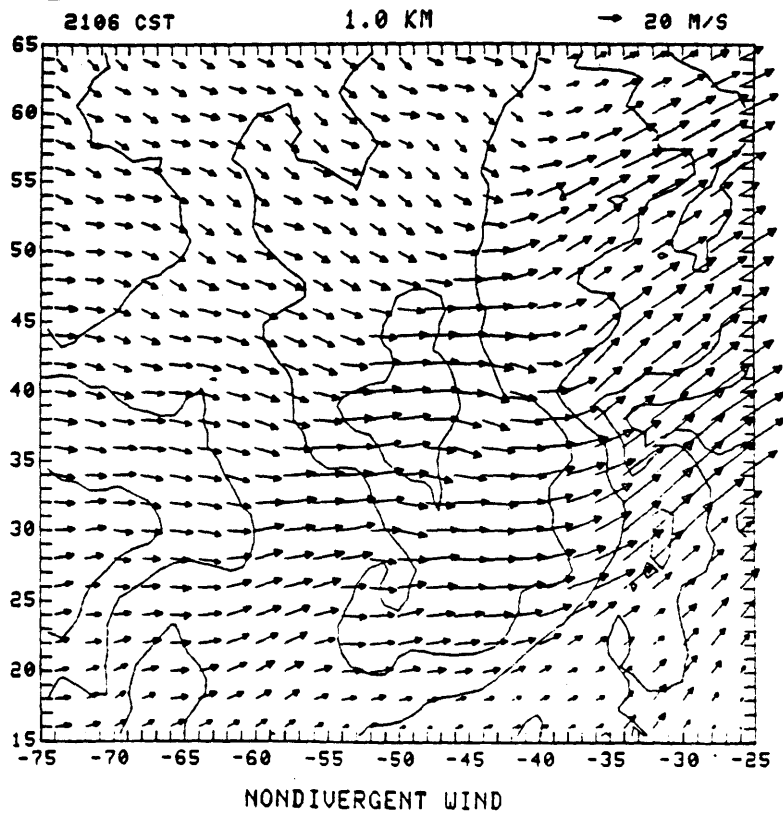
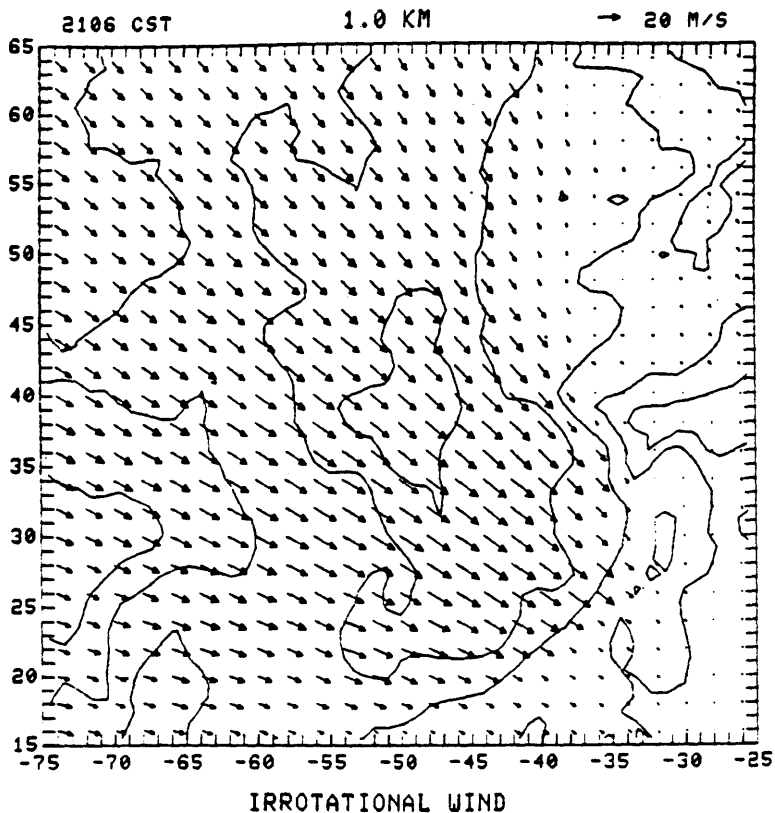


Figure 5-8

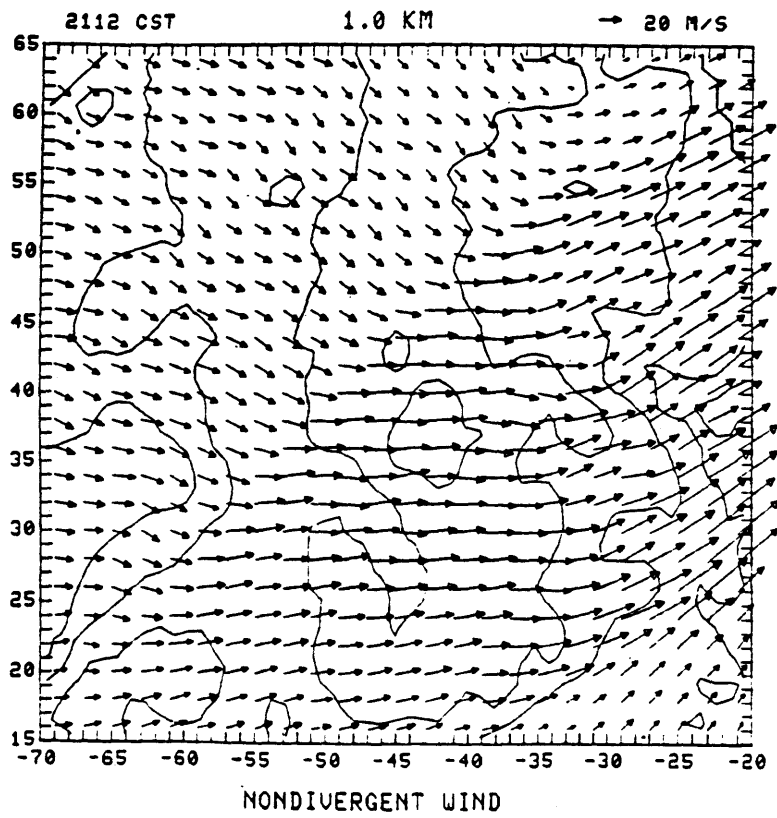
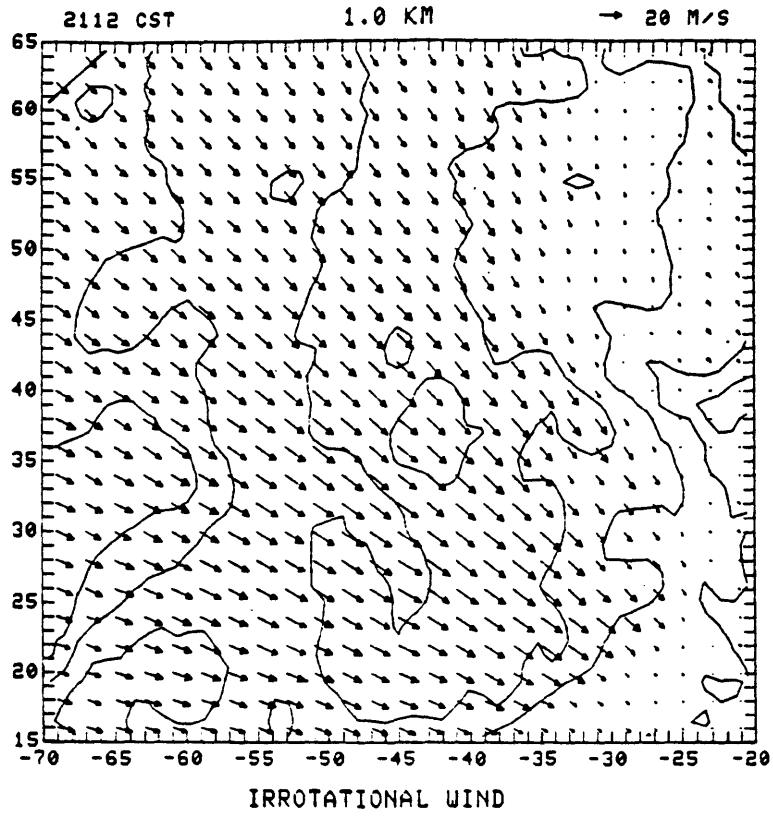


Figure 5-9

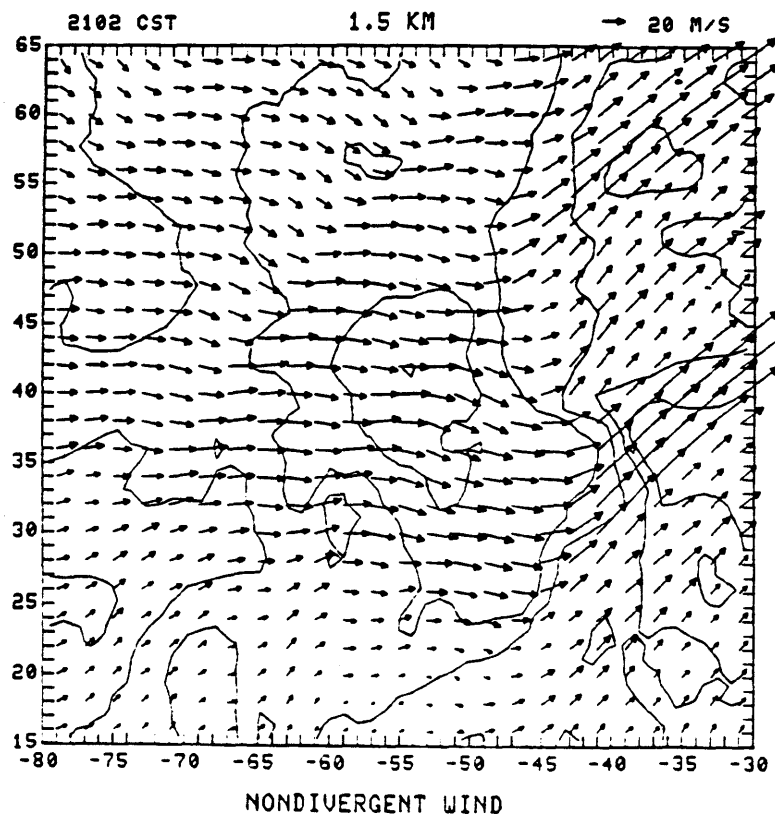
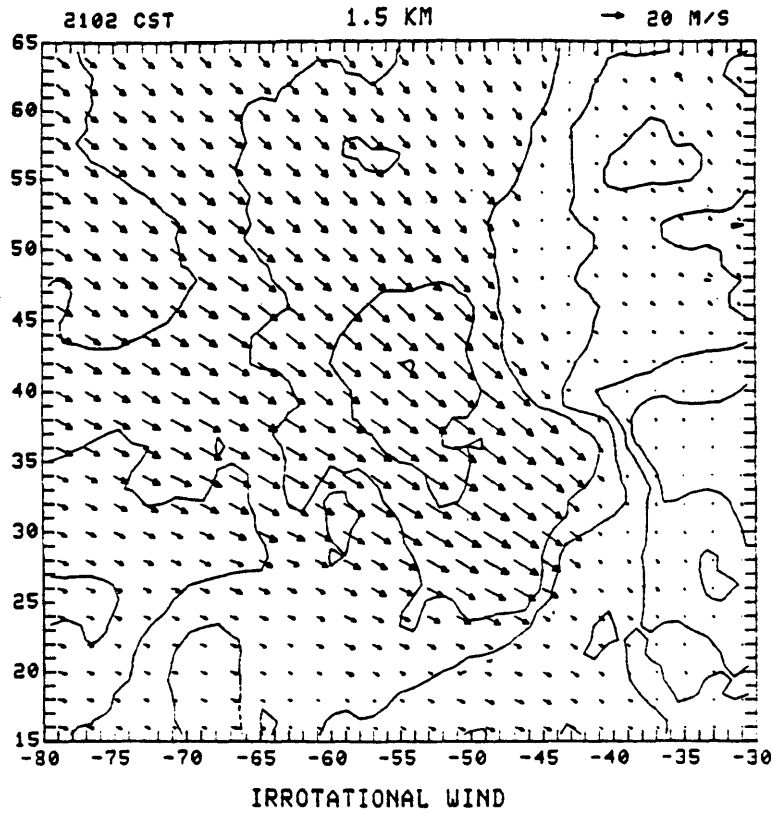


Figure 5-10

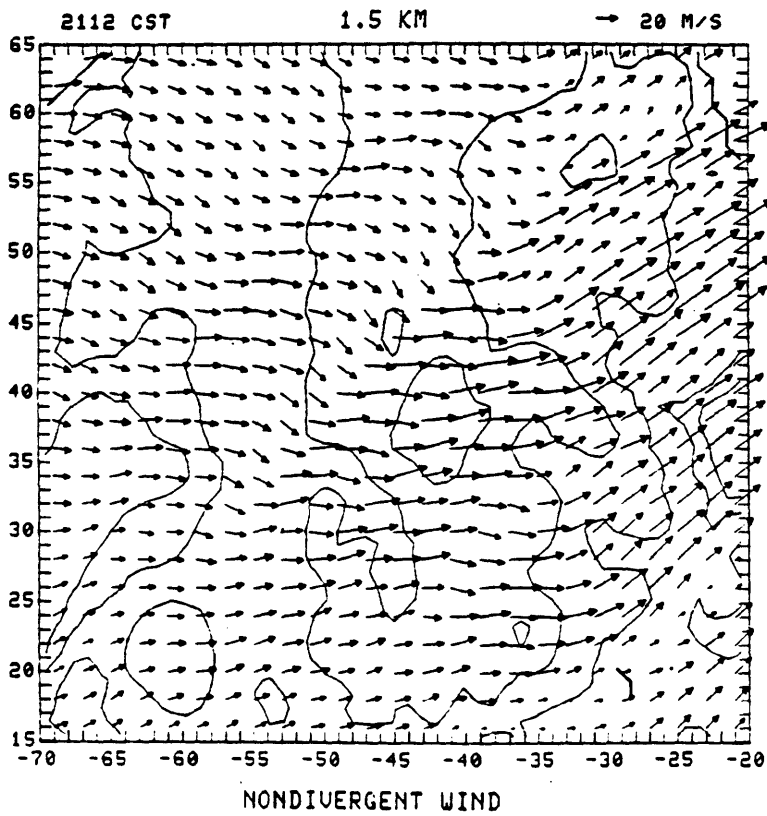
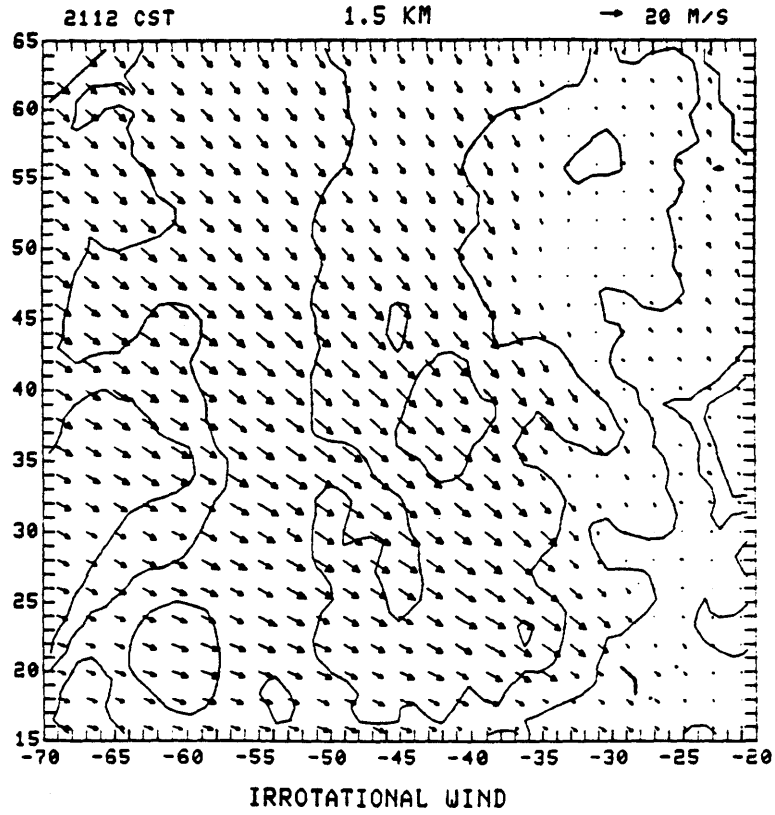


Figure 5-11

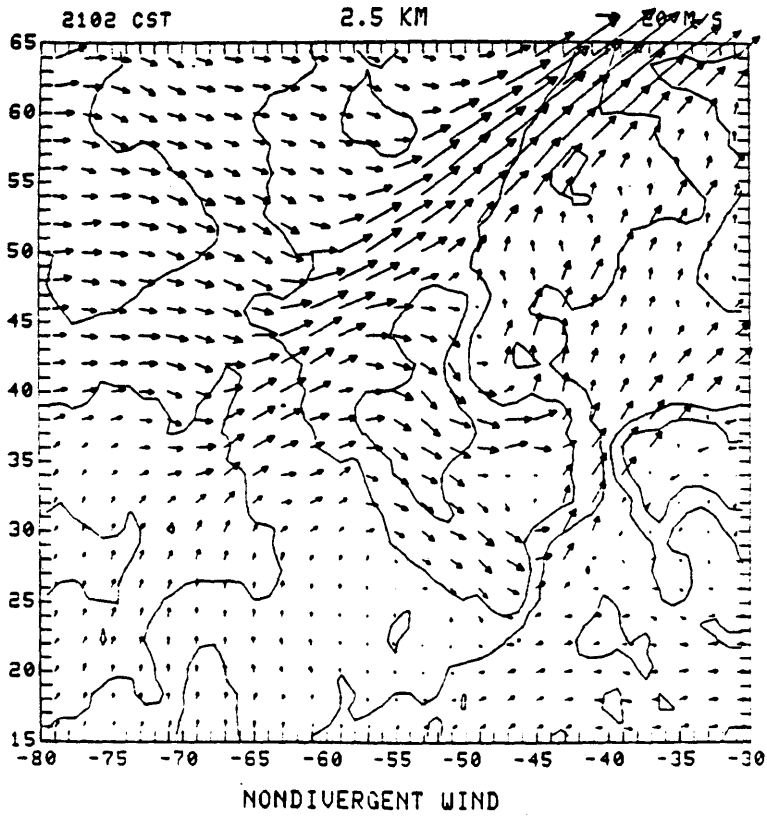
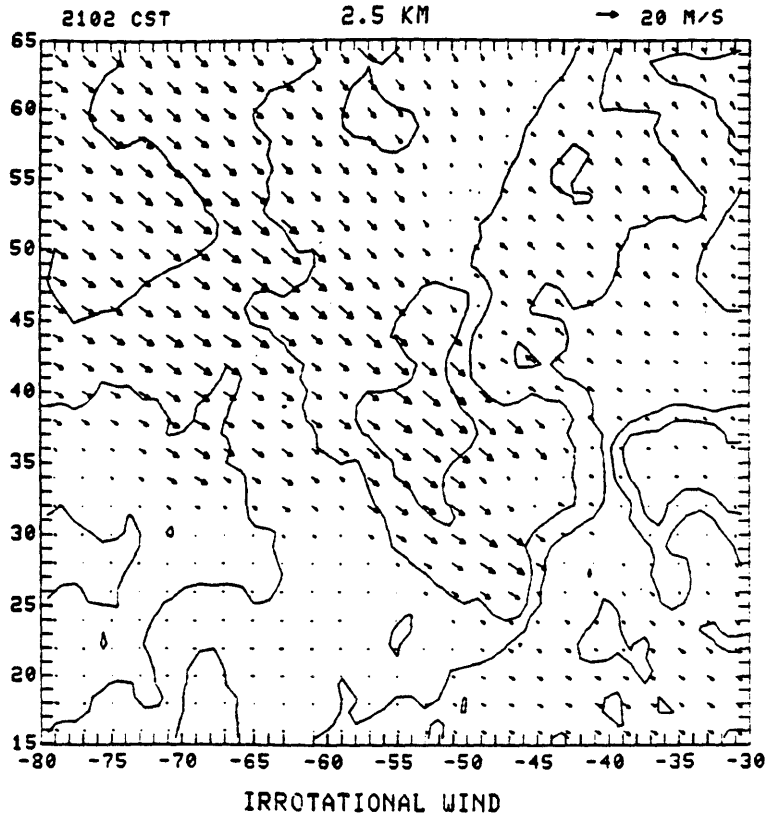


Figure 5-12

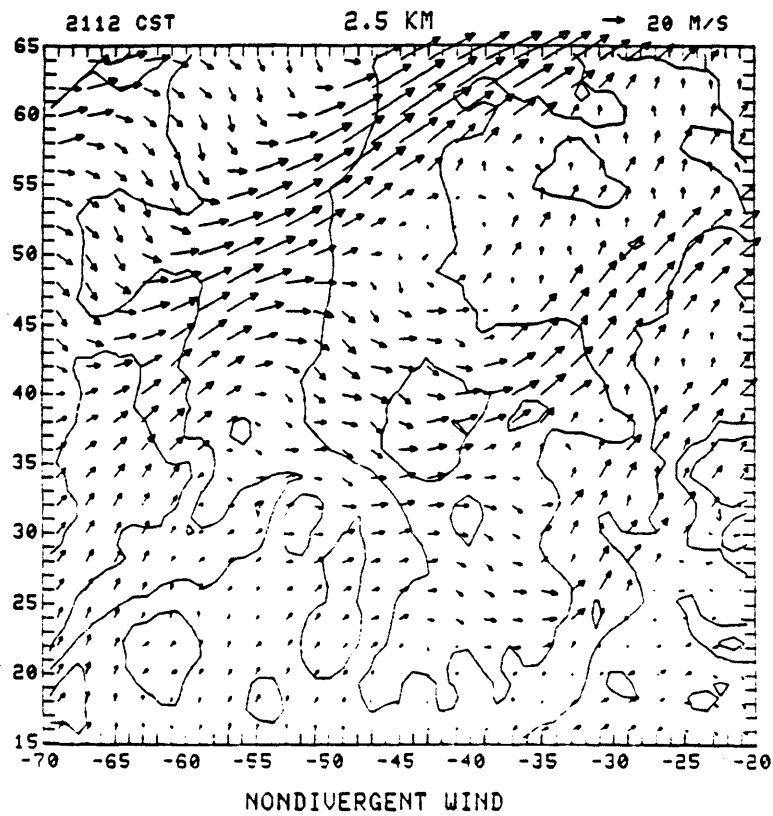
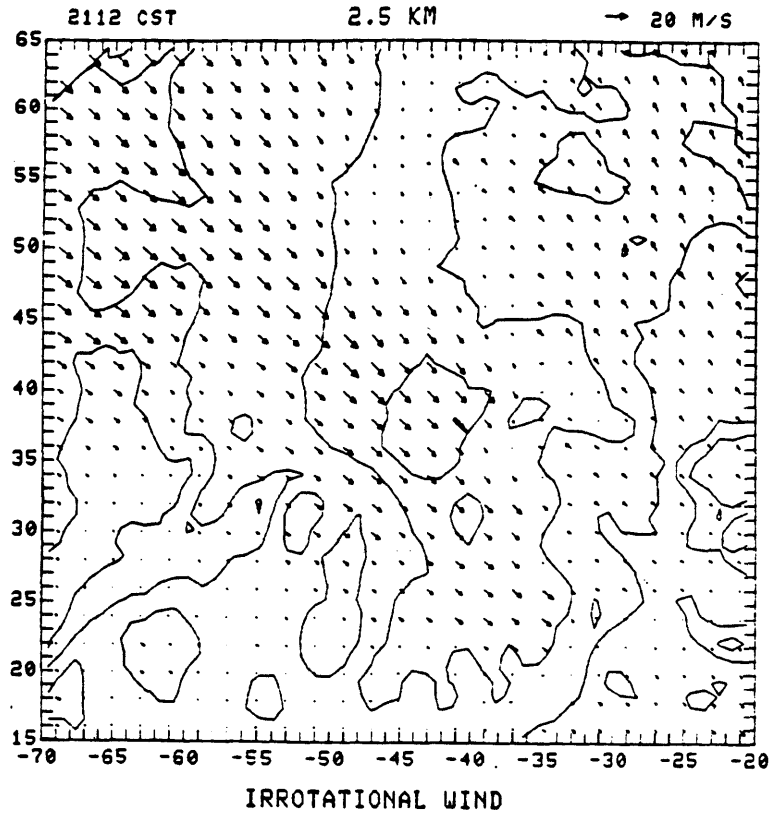


Figure 5-13

Accuracy in this numerical integration is indicated by how close the derived flow is to being either irrotational or nondivergent as the case may be. A test was performed using the radial component of a known divergent windfield and the constraint of irrotationality to derive the azimuthal velocity field. As one would expect, the errors were all in the azimuthal direction and they increased approximately linearly away from the boundary. The magnitude of the error was 20% of the magnitude of the wind at the end of the integration path.

If the boundary conditions are known fairly accurately, then the numerical accuracy can be improved by integrating first in from one boundary and then in from the opposite boundary. The results could be combined using the integrated value with the least numerical error as the true value at each point. This procedure has not yet been tested.

Before any real assessment of this entire technique can be made it must be tried on radar observations of a windfield that is known in detail from a multiple-Doppler analysis so that an extensive and quantitative comparison can be made.

B. Discussion of derived winds

Although the results from the "nondivergent" experiment at 2047 CST appear closer to the actual winds from the 2-Doppler analysis than the "irrotational" winds, my best estimates of the actual wind fields are those from the combined irrotational and nondivergent experiment and they are the only ones that will be discussed here. These are meant simply to give a qualitative picture of the flow and features mentioned below must only be considered heuristically. It is somewhat instructive to turn back to the pictures in the previous section showing the

separate flows to identify which features are more divergent and which are more rotational. Keep in mind that the radar would detect identical radial velocity fields for each of the three experiments. The mean storm motion has not been subtracted out of the displayed winds. The storm was, however, moving toward 110° at 18 m/s.

The following figures (5-14 through 5-17) largely speak for themselves but a few interesting features will be pointed out. There is evidence at 1.0 km (figures 5-14 and 5-15) of cyclonic curvature of the windfield in the upper right corners and gentle anticyclonic curvature in the lower left corners of the figures. The increase of cyclonic vorticity with time is also evident in the winds themselves and in the responding reflectivity fields. The downburst of low θ_e air and strong wind gusts hits the surface mesonet station at (-30,25) just south of CIM at 2110 CST. At this altitude the downburst signature consists of converging winds at the occlusion point of the gust fronts.

At 1.5 and 2.5 km only two times are shown, 2102 and 2112 CST. The flow at 1.5 km (figure 5-16) is basically very similar to that at 1.0 km, the main differences being that the magnitude of the velocities is smaller and the rotation is enhanced.

At 2.5 km (figure 5-17) the flow is generally weak but there is a dramatic "mesocyclone" in the northern portion of the displays. The air appears to be moving directly from this cyclonic circulation into the region of the downburst(s) at both 2102 and 2112 where it halts abruptly and becomes divergent. The flow appears to be diverted around solid obstacles at 2102 (-46,33 and -50,48) and at 2112 (-37,35 and -40,50). These are probably regions of strong upward motion, which is consistent with the radial velocity contours in figures 4-14 and 4-16.

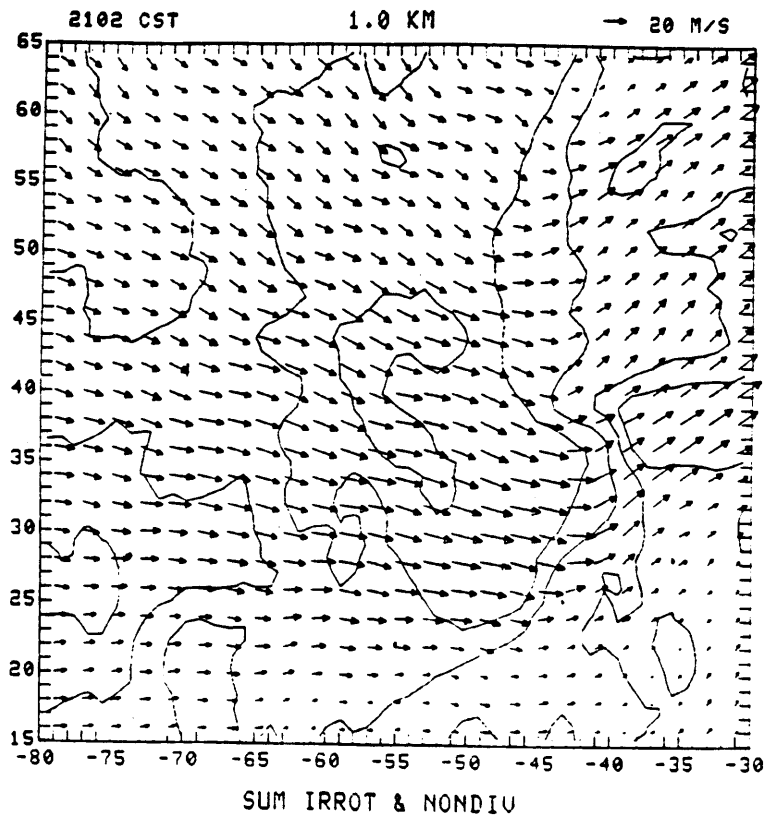
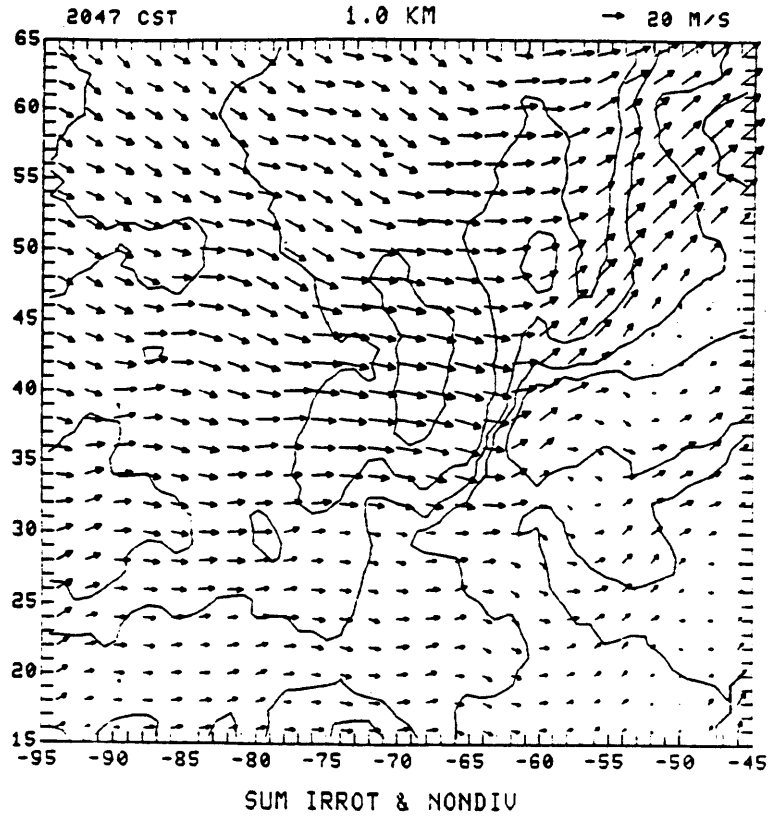


Figure 5-14

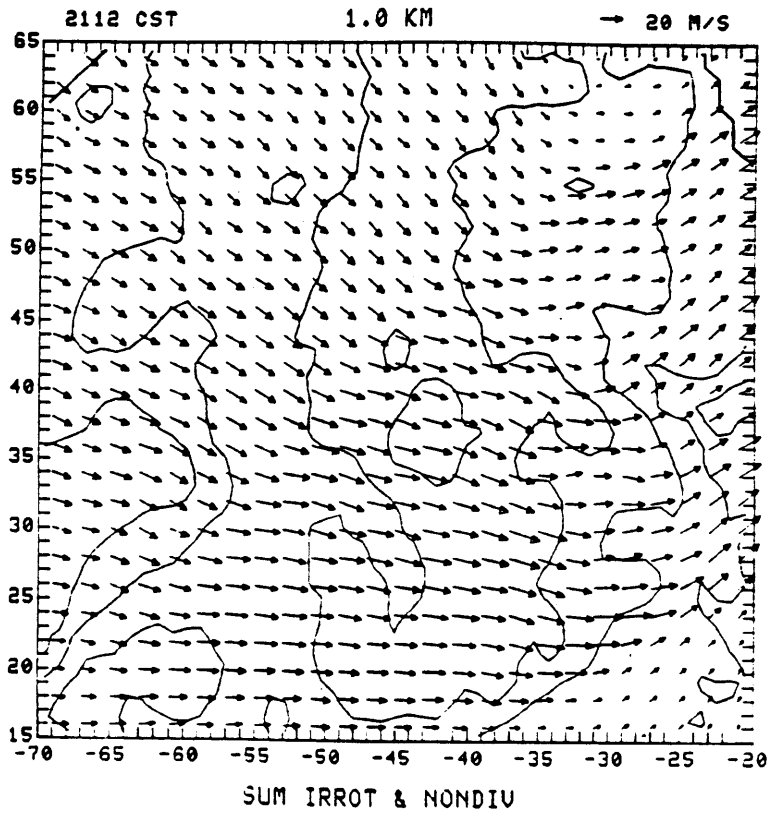
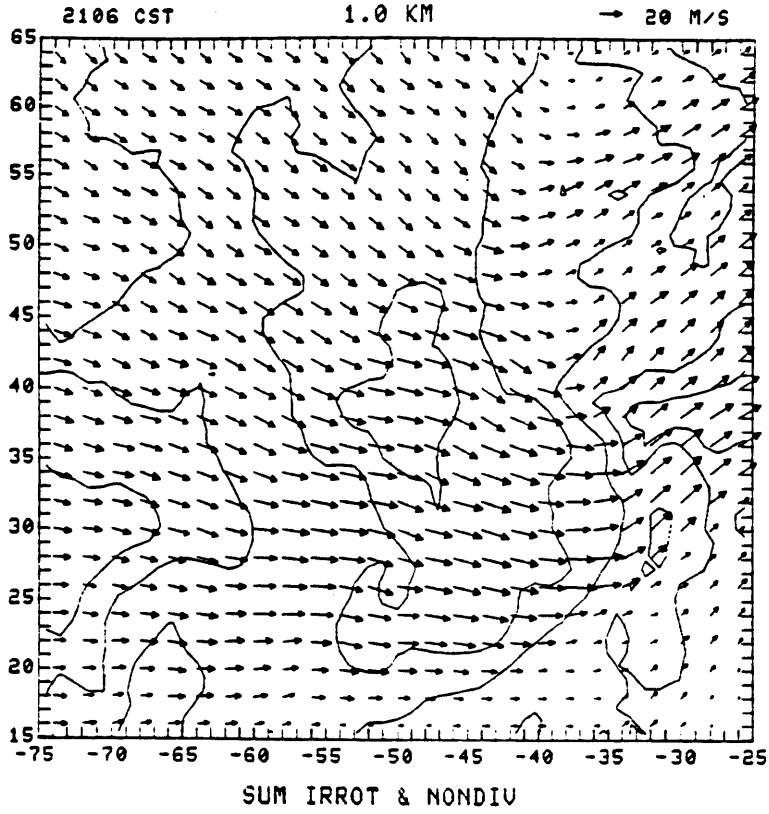


Figure 5-15

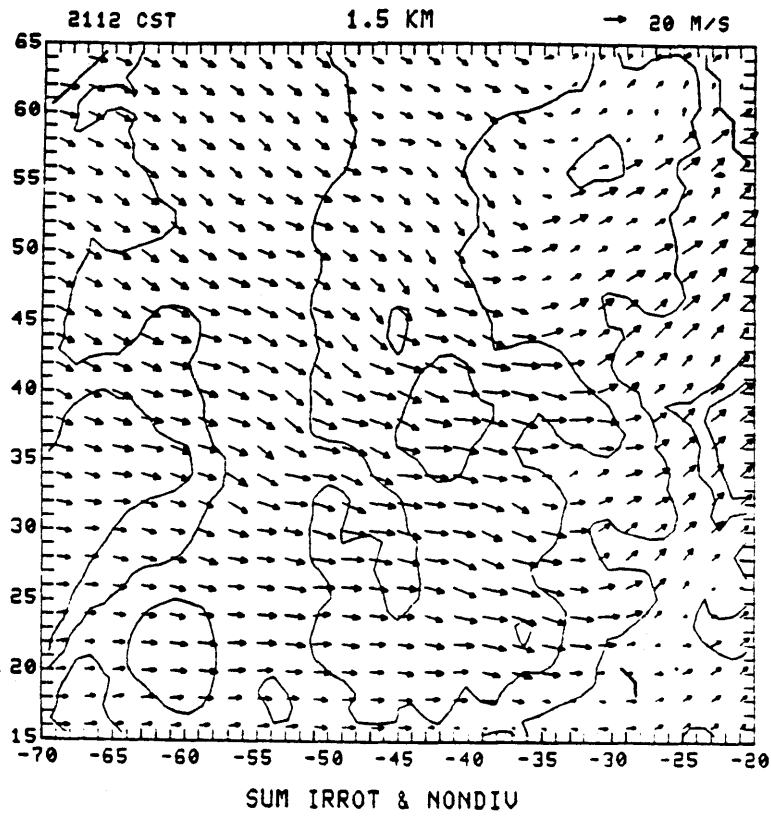
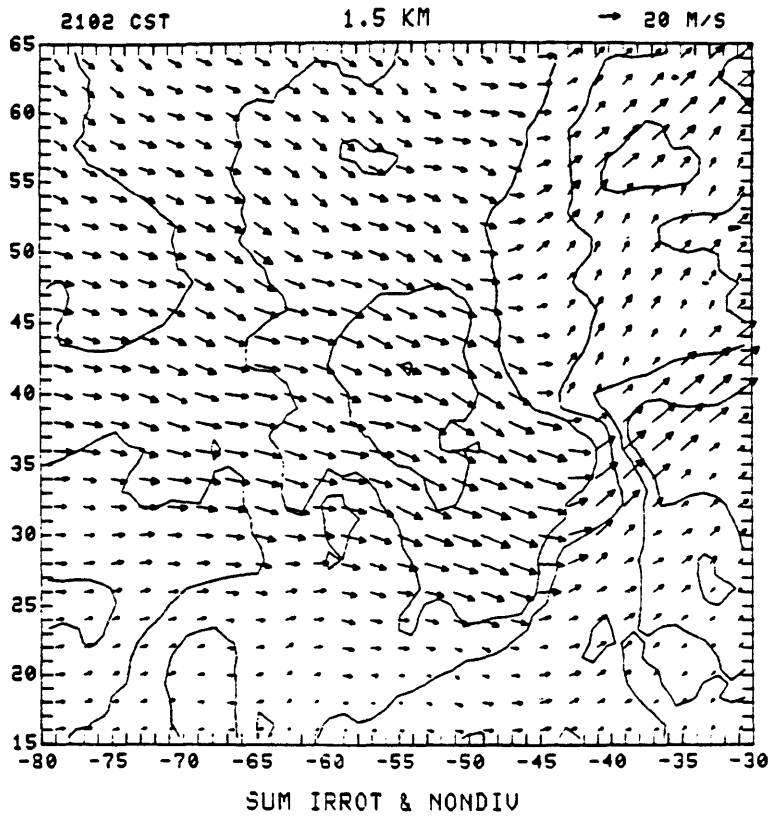


Figure 5-16

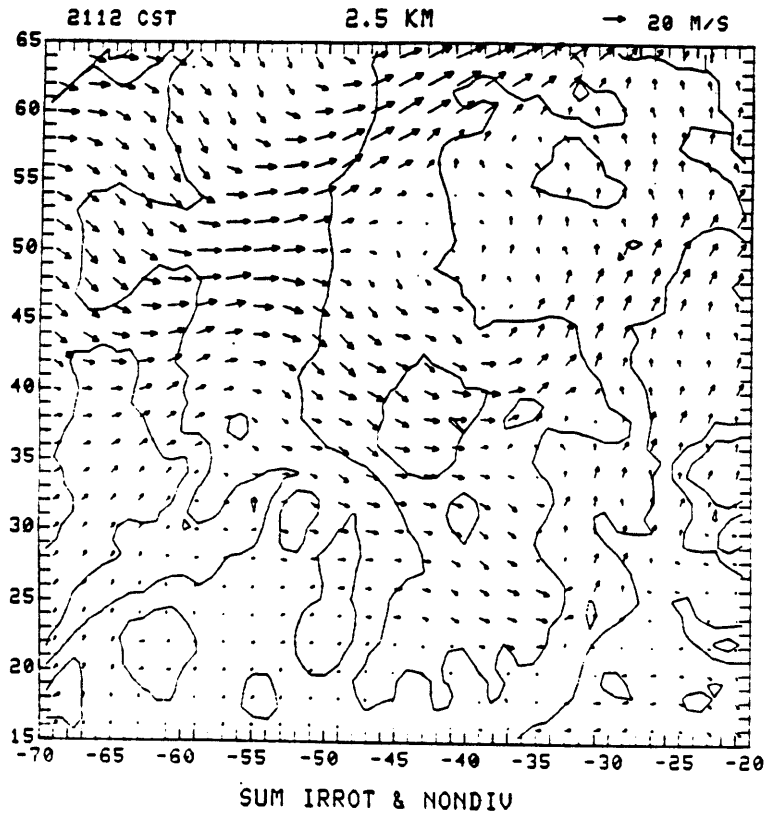
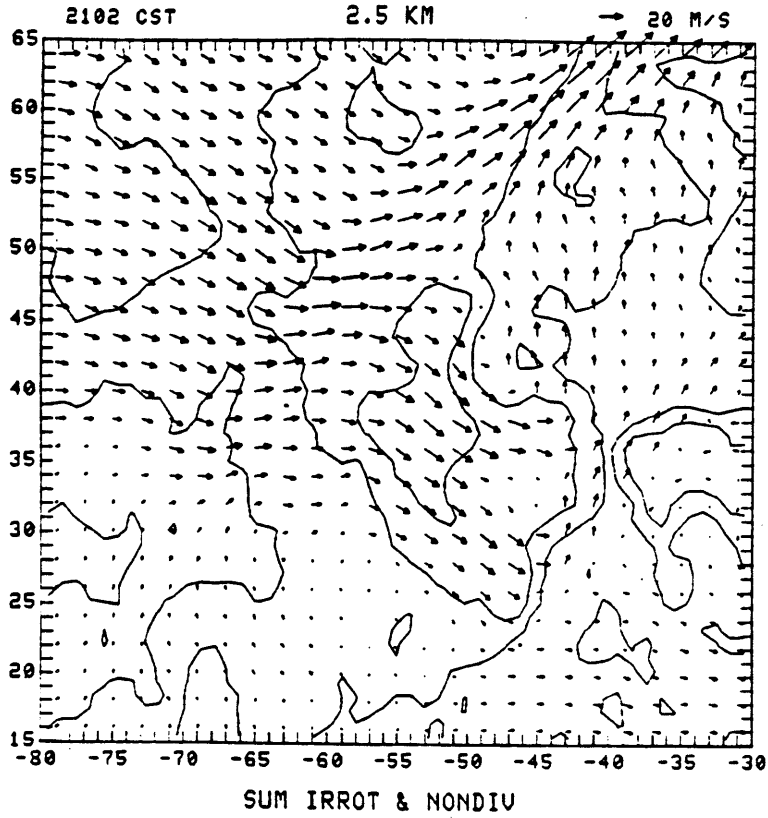


Figure 5-17

6. A New Hypothesis

In this chapter I present a new hypothesis, developed using the preceding Doppler radar observations as a guideline, for thunderstorm downbursts. It is different from previous hypotheses (see chapter 2) in that dynamic rather than thermodynamic processes are proposed to be responsible for the downbursts. This new hypothesis accounts well for the rotational characteristics of downbursts reported in other observational studies which have not been explained by the earlier proposals and it makes the connection between the LEWP, the bow and spearhead echoes, the cyclonic rotation to the north and the anticyclonic rotation to the south, the gust front, the hook echo, and the tornado. The proposed mechanism differs little from the mechanism determined, in a fine mesh (.25 km) numerical simulation by Klemp and Rotunno (1982), to produce a small scale "occlusion downdraft" near the tornadic region in a supercell thunderstorm. Appendix C contains a brief summary of their results. This new hypothesis is simply stated below and not proved, for although diagnostics may be performed, they are beyond the scope of this work.

The basic premise is that when a cell along a line or front becomes very strong and organized it begins to take on some "supercell" characteristics, particularly in its post-mature stage. Horizontal vorticity, which is present in the low level environmental shear and which is generated by the horizontal buoyancy gradients in the storm, is tilted into the vertical near the main updraft. Strong low level convergence, caused by the downdraft outflow from the collapsing cell, forces stretching of the now vertically oriented vortex tubes.

Significant cyclonic rotation begins at low levels and, as a result, the gust front begins to occlude. Anticyclonic vorticity is also generated but the cyclonic vorticity appears to be favored. The horizontal curvature of the flow due to the cyclonic rotation promotes downdraft intensification along the backside of the gustfront, especially near the circulation center, by dynamically inducing a vertical pressure gradient. This acts to rapidly accelerate air downward causing the downburst. The downburst might even form first at low levels and then extend upward as the flow adjusts to the dynamic pressure gradient. It should be noted that the vertical kinetic energy created in this way can only come from a redistribution of horizontal kinetic energy; this places an upper bound (a very generous one) on the attainable vertical velocities. A schematic diagram depicting the proposed mesoscale circulation responsible for distorting the radar echo and inducing the downbursts is presented in figure 6-1. Note that the streamlines in that figure indicate storm relative flow while all the velocity fields in the previous chapters indicated ground relative flow.

The configuration of the gust front, marked by the cold front boundary in figure 6-1, is very much like that in figure 4-6. There is an updraft denoted by a solid contour near the occlusion point of the gust front in 6-1 which is in a region of strong convergence. It was in a comparable region of the 13 April storm that cells ahead of the main storm cell were growing and subsequently merging with the main cell. It was also in this region that an updraft was inferred from the observations. The downburst, denoted by the small circular dashed contour in figure 6-1, is close to but south and west of the updraft and is behind the north-south oriented portion of the gust front, just as in

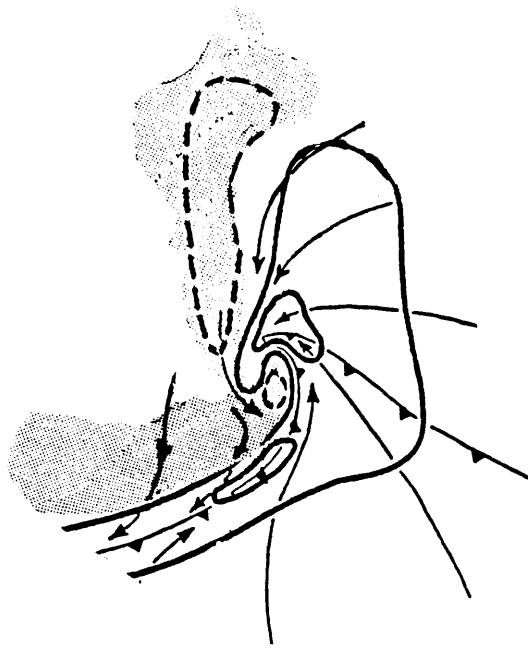


Figure 6-1 Proposed circulation inducing downbursts. Any similarity to figure C-1 is intended. Dashed contours indicate downdrafts, solid contours indicate updrafts. The stippled area represents reflectivity greater than 30 DbZ. The small scale downdraft in the "spearhead" is the downburst. Note that it is the mesoscale circulation which distorts the radar echo and induces the downbursts, not vice versa. Streamlines indicate storm relative flow.

figure 4-7. Notice also the cyclonic curvature of the flow around the updraft-downburst area and the anticyclonic curvature south and west of there.

The potentially cool and dry air (low θ_e) thought to characterize the downburst may well be a property of the entire thunderstorm outflow. It is likely that the low θ_e air is already in the boundary layer when the downburst occurs.

There are some differences between a strong convective cell along a front separating two distinct air masses with very different stability properties and an isolated supercell imbedded in unstable air which is largely horizontally homogeneous (except for perhaps an old outflow boundary or a dry line providing the initial forcing). The supercell creates its own temperature discontinuities at low levels while the horizontal temperature discontinuities of the line cell are partly of its own creation and partly due to the synoptic scale horizontal variations concentrated at the cold front. This may be why the line cell does not usually become strongly tornadic like the supercell storm. The stability of the air behind the cold front is too great and the storm rapidly decays when this air is circulated through the core.

In summary, I view the thunderstorm downburst as an inherently low level phenomenon, with essentially all of the important ingredients contained in the lowest 3 to 4 kilometers of the atmosphere. It will appear in the post-mature to collapsing phase of the cell's evolution. Dynamic vertical accelerations could well be an order of magnitude larger than thermodynamic (buoyancy) accelerations at low levels. It is apparently misleading to look for the "source height" of the downburst. It is induced by a horizontal mesoscale circulation at low levels which

nearly, or actually does, become tornadic. Although commonly thought to be mainly divergent, the downburst is really a rotational phenomenon. It is also apparently misleading to use conserved properties such as equivalent potential temperature or horizontal momentum to trace the downburst air; those properties only help indicate the source height of the outflow air from the whole storm.

This is a novel view of the thunderstorm downburst and it has not been proved. It does account for the observations and link phenomena which were known to occur simultaneously but were thought to be disconnected. Calculations must be done before its real relevance can be determined.

7. Conclusions and Future Work

The major thrust of this work has been the analysis and presentation of detailed Doppler radar data collected during an Oklahoma thunderstorm in which downbursts developed. The distinctive "bow" or wavelike radar echo associated with this type of thunderstorm was determined to be caused by the low level cyclonic rotation. The spearhead echo, identified as a pointed appendage in the direction of motion, was determined to be a cell growing along an occluded gust front ahead of the main storm cell. The growth of this cell is an indication of the increased convergence in the region of gust front occlusion.

A technique was also tested which provided an estimate of the horizontal vector windfield using the radial velocity measured by Doppler radar and the constraints of nondivergence and irrotationality. Although the resultant windfields can only be considered qualitatively, they did show a dramatic mesocyclone at $z=2.5$ km, north of the area where the downbursts were occurring.

Careful examination of the data at different times has led to the identification of low level convergence and vorticity as major factors in downburst development. A new hypothesis was presented which identifies tilting of horizontal vorticity into the vertical and a subsequent increase in cyclonic rotation as the crucial elements in creating the dynamic pressure gradient proposed to be responsible for the downburst.

Since all the observations to date have been viewed with thermodynamic mechanisms in mind as the cause of the downbursts, I believe it would be fruitful to review them in light of this new

hypothesis. Estimates need to be made of the rate of vorticity production, the curvature of the flow, the dynamic vertical pressure gradient, and the total vertical acceleration in the vicinity of the downburst. A detailed, general scenario needs to be developed for the evolution of the thunderstorm downbursts for, although the thunderstorms themselves are fairly predictable and easy to track, the accurate prediction of the downbursts has eluded meteorologists.

The theoretical work on thunderstorm downbursts has barely begun. Although the analogy is not complete, it may be possible to exploit some of the work which has been done on supercell storms, mesocyclones, and tornadoes, with a few modifications, to help understand the line cell circulation. The reason why some frontal storms do become tornadic while others induce downbursts but do not become tornadic needs to be understood.

Once the downburst pattern is well recognized, future data gathering experiments can be designed specifically to observe them. I caution the meteorological community against drawing sweeping conclusions about downbursts in all parts of the country from the results of the JAWS experiment. The dry downbursts and microbursts observed there are hazardous and difficult to predict but they are perhaps characteristic of that local environment. Theoreticians must not channel all of their efforts into understanding dry downbursts while the more common and equally hazardous thunderstorm downbursts go unexplained.

Appendix A.

The data analyzed in chapters 4 and 5 was collected by the Norman, OK Doppler radar (NRO). The radar transmits at a wavelength of 10.52 cm with peak power of 750 kw. The pulse repetition time for the radar can be varied and two different values, 768 μ s and 1075 μ s, were used during the time period of interest.

Available coverage

Table A contains information about the available radar coverage from NRO for the period from 2045 CST to 2135 CST on 13 April 1981. The contour maps of chapter 4 and the derived horizontal wind fields of chapter 5 are identified with a characteristic time, e.g. 2047 CST, which is approximately the midpoint of the given tilt sequence. The actual starting and ending times as well as the labelled times are shown in Table A.

In all cases the radar began the scanning sequence at the lowest elevation angle and proceeded sequentially to the highest elevation angle in increments which varied from 0.4 to 1.0 degrees. Thus the data at low elevation angle was always collected slightly earlier than the labelled time and data at high elevation angle, slightly later. The direction of rotation of the radar alternated between clockwise and counterclockwise, scanning first from, say, 250° to 20° at a given tilt and then scanning back from 20° to 250° at the next tilt. Azimuth and elevation information is also shown in Table A.

TABLE A

| Labelled time | Start time | End time | Min elev | Max elev | # diff elev | Min azm | Max azm |
|------------------|---------------|-------------|-------------|-------------|----------------|------------|------------|
| 2047 | 204530 | 204850 | 0.4 | 4.6 | 7 | 250° | 20° |
| 2050 | 204900 | 205119 | 0.5 | 2.0 | 4 | 255° | 20° |
| 2057 | 205551 | 205825 | 0.4 | 6.1 | 9 | 255° | 20° |
| 2102 | 205948 | 210349 | 0.5 | 10.0 | 14 | 255° | 20° |
| 2106 | 210438 | 210729 | 0.5 | 6.9 | 10 | 255° | 20° |
| 2112 | 211044 | 211415 | 0.5 | 9.3 | 13 | 265° | 30° |
| 2117 | 211603 | 211842 | 0.5 | 6.9 | 10 | 265° | 30° |
| 2124 | 212246 | 212606 | 0.4 | 8.5 | 12 | 265° | 30° |
| 2128 | 212643 | 212956 | 0.5 | 10.2 | 12 | 265° | 30° |
| 2132 | 213034 | 213400 | 0.5 | 10.1 | 12 | 265° | 30° |

Data Analysis

The data analysis procedure can be divided up into two main parts, editing and interpolation.

1.Editing

The first step in the editing process was to automatically remove velocity estimates with a signal-to-noise ratio less than -1 Db. More typical thresholds might be higher (5-10 Db) but because the returned power from the gust front region was weak and velocity estimates for that region were desired, the lower SNR value was used.

The second step was to check the data for range aliasing. Range aliasing can occur when significant power is returned from areas beyond the unambiguous range interval. This range interval is the maximum radial distance at which a transmitted pulse can be scattered and returned to the radar before the next pulse is transmitted. When echoes from beyond this interval are received (second trip echoes) they are referenced by the radar to the most recently transmitted pulse. If the second trip echo is comparable to the first trip echo then the velocity estimate for that point will be contaminated. Instead of trying to correct this problem the velocity data at a point was disregarded if the second trip echo was not at least 10 Db weaker than the first trip echo.

The third and final step in the data editing procedure was to check for Doppler velocity aliasing. When the true velocity exceeds the unambiguous velocity limits ($\pm V_u$) the radar detects an aliased velocity which is within those limits. The detected value differs from the true value by $2V_u$ or a higher multiple of $2V_u$. Aliased velocities are easy to find: the velocity values will change abruptly in the radial

direction from $-V_u$ to $+V_u$ or vice versa.

Several automatic schemes for detecting velocity aliasing have been reported which take advantage of this abrupt change in velocity in the radial direction. In my case, however, the velocity dealiasing was simply done manually. A manual check of the data must be performed even when an automatic procedure is used in order to detect dealiasing and other editing failures.

2. Interpolation

The radar collects data in a spherical coordinate system but because the earth's surface is curved and the atmosphere's index of refraction changes with height, the true height z of a data point will not simply be the slant range, R , multiplied by the sine of the elevation angle (Φ). Since the surface of the earth is always taken as $z=0$, the distance D from the radar to a data point $(x,y,0)$ along the curved earth will likewise not simply be $R \cos \Phi$.

The equations used to compute z and D were taken from Brown, et al (1981) and are given below.

$$z = E \left\{ 1 + \left(\frac{R}{E} \right)^2 + \frac{2R}{E} \sin \Phi \right\}^{1/2} - E \quad A1$$

and

$$D = E \arcsin \left(R \cos \Phi / (E + z) \right) \quad A2$$

where R , D , z , and Φ have been defined above and E is 1.33 times the sum of the earth's radius and the radar height above sea level. Spherical

geometry can then be used to compute the x and y coordinates of the data point.

Once each data point had been assigned a set of Cartesian coordinates the interpolation to a regularly spaced Cartesian grid with the origin located at NRO was performed. Grid spacing was 1.0 km in both horizontal directions and 0.5 km in the vertical.

The data value assigned to each regular grid point was a distance weighted average of all data that fell within an oblate spheroidal volume surrounding that point. The vertical influence radius was chosen to be 0.75 km and the horizontal, 1.0 km. A Cressman weighting function W_j (Cressman, 1959) of the form

$$W_j = \begin{cases} \frac{R^2 - D_j^2}{R^2 + D_j^2} & D_j \leq R \\ 0 & D_j > R \end{cases} \quad \text{A3}$$

was used, where D_j is the distance from the j th datum to the regular grid point and R is the influence radius given by

$$R = \frac{R_H R_Z}{(R_H^2 \sin^2 \psi_j + R_Z^2 \cos^2 \psi_j)^{1/2}} \quad \text{A4}$$

where

$$\psi_j = \arctan \left[\frac{z_j}{(x_j^2 + y_j^2)^{1/2}} \right] \quad \text{A5}$$

R_H and R_Z are the horizontal and vertical influence radii, respectively, and x_j , y_j , and z_j are the coordinates of the j th datum relative to

the gridpoint.

The weighted gridpoint average of a quantity \bar{Q} (Doppler velocity or reflectivity) is then given by

$$\bar{Q} = \frac{\sum_{j=1}^N W_j Q_j}{\sum_{j=1}^N W_j} \quad A5$$

where N is the total number of data within the influence volume.

It is very common to assume that the storm is in a steady state during the radar data collection period (about 4 minutes) so that the observations can be translated horizontally by a distance proportional to the difference in time between the actual data detection time and the reference time for that particular tilt sequence. Thus the mean storm motion must be determined, usually by visually correlating radar scans at a given elevation. This procedure was NOT carried out in this analysis for the mean storm motion was different at different altitudes as well as in different areas at the same altitude and the steady state assumption was questionable. However, a rough estimate of the mean low-level storm motion was 18 m/s toward 110°. The lack of correction for this motion would be most noticeable in figures 4-14 through 4-16. As an upper limit, the lowest and highest observations in those figures should be translated to the east or west, respectively, relative to the midlevel, by an amount

$$2 \text{ min} \times 20 \text{ m/s (toward } 90^\circ) = 2.4 \text{ km}$$

Other observations above or below the midlevel would be translated correspondingly less.

It is also common to remove the contribution to the Doppler velocities of the terminal fall speed of the precipitation which was not done in this analysis. In the worst case, at an elevation angle of 10° and with reflectivity values of 55 DbZ, this would add 2.5 m/s to the detected velocities toward the radar. This is equal to half the contour increment in figures 4-14 through 4-16.

Once all of the data had been interpolated onto the regular Cartesian grid the contour maps shown in chapter 4 were produced.

As noted in chapter 5, the Doppler velocity data used there was interpolated first to a regular cylindrical coordinate system in order to do the calculations necessary for deriving the azimuthal velocity and was subsequently interpolated onto an x-y Cartesian grid at each height. All other procedures were completed as described above.

Appendix B.

The National Severe Storms Laboratory Spring Program is run every year to acquire observational data on severe storms in Oklahoma. There are two permanently located Doppler radars in the area (CIM and NRO) and both of them were operational during 1981.

A 2-Doppler derivation of the horizontal windfield in a storm can be very accurate and complete when the beams from the radars simultaneously illuminate the region in question, and do so at approximately right angles to each other. Then the radial velocity fields from the two radars represent estimates of two orthogonal components of the windfield. In contrast, along and near the line connecting the two radars it is only possible to detect one component of the windfield; this is the same situation as having only one radar present.

A glance as figure 4-2 will show that the geometric configuration of the storm relative to the two radars was quite poor for a 2-Doppler analysis. However, in an effort to obtain as much information about the 13 April 1981 case as possible, and thanks to the bravery of Dr. Peter Ray at NSSL, two separate 2-Doppler analyses were attempted. The chosen analysis boxes are shown by dashed lines in figure 4-2.

Before the winds could be estimated, the data had to be edited and interpolated onto a common Cartesian grid with the origin at NRO. Velocity estimates with a signal-to-noise ratio less than the chosen threshold value of -1 Db were discarded. All velocity dealiasing was done manually and an automatic check for range aliasing which required that the second trip echo be at least 10 Db less than the first trip

echo was performed. The data was transferred from radar spherical coordinates to Cartesian coordinates using a Lambert conformal map projection with standard parallels of 34°N and 37°N and was interpolated to a regular Cartesian grid using a Cressman weighting function. Horizontal grid spacing was 1.0 km at 2045 CST and 0.5 km at 2130 CST. At both times the vertical spacing was 0.5 km. Observations were relocated, using an advective procedure, to their estimated position at the specified analysis time.

The 2-Doppler program of Ray, et al (1980) (Technique A) was used to estimate the three dimensional windfields and is briefly described below.

If each radar is located at (x_i, y_i, z_i) where $i = 1$ or 2 , and u , v , and $W (= w + V_t)$ represent the particle motion in the east, north, and local vertical directions at a data point located at (x, y, z) then the measured radial velocity by the i th radar, V_i , is related to the Cartesian wind components by

$$\frac{u(x-x_i)}{R_i} + \frac{v(y-y_i)}{R_i} + \frac{W(z-z_i)}{R_i} = V_i \quad \text{B1}$$

where

$$R_i = \left[(x-x_i)^2 + (y-y_i)^2 + (z-z_i)^2 \right]^{1/2} \quad \text{B2}$$

and V_t is the particle terminal velocity determined from the analyzed reflectivity and corrected for the effects of the air density on the fall speed and of having different water phases within a cloud layer.

The cartesian wind components are then derived using the anelastic form of the equation of continuity

$$\frac{\partial u}{\partial x} + \frac{\partial v}{\partial y} + \frac{\partial w}{\partial z} + \kappa w = 0 \quad \text{B3}$$

(where κ is the logarithmic rate of change of density with height), combined with the radar observations and an estimate of V_t . The equations for u and v derived using B1 are

$$u = \frac{\sum R_i V_i (x-x_i) \sum (y-y_i)^2 - \sum R_i V_i (y-y_i) \sum (x-x_i)(y-y_i)}{\sum (x-x_i)^2 \sum (y-y_i)^2 - [\sum (x-x_i)(y-y_i)]^2} \quad \text{B4}$$

$$+ \frac{w [\sum (y-y_i)(z-z_i) \sum (x-x_i)(y-y_i) - \sum (y-y_i)^2 \sum (x-x_i)(z-z_i)]}{\sum (x-x_i)^2 \sum (y-y_i)^2 - [\sum (x-x_i)(y-y_i)]^2}$$

and

$$v = \frac{\sum R_i V_i (y-y_i) \sum (x-x_i)^2 - \sum R_i V_i (x-x_i) \sum (x-x_i)(y-y_i)}{\sum (y-y_i)^2 \sum (x-x_i)^2 - [\sum (x-x_i)(y-y_i)]^2} \quad \text{B5}$$

$$+ w \frac{[\sum (x-x_i)(y-y_i) \sum (x-x_i)(z-z_i) - \sum (x-x_i)^2 \sum (y-y_i)(z-z_i)]}{\sum (y-y_i)^2 \sum (x-x_i)^2 - [\sum (x-x_i)(y-y_i)]^2}$$

where the sums are from $i = 1$ to $i = 2$.

The procedure is to solve equations B4 and B5 using an initial estimate of w and then to refine the estimate of w by B3 which is integrated upward using a boundary condition of $w=0$ at $z=0$. This process is repeated until the solution converges.

Certain other conditions must be satisfied in order for the velocity estimate at a point to be acceptable. First, the determinant of the coefficient matrix, the denominator in B4 and B5, was required to

be "small" (less than 2.2×10^{-10}). Also, the variances of the velocity errors, σ_u^2 and σ_v^2 , were required to be positive and less than 30.0 or 2.0, respectively. These are relative values since the error variance of the interpolated radial velocity was assumed to be 1.0 m /s (probably higher than it truly was). Thus, the difference between figure 5-4 and figure 5-5 which shows a larger portion of the windfield is due to the chosen threshold for the velocity error variances.

Appendix C.

A numerical simulation of the tornadic region in a supercell storm recently completed by Klemp and Rotunno (1982) uses a high resolution version of the successful three dimensional thunderstorm model of Klemp and Wilhelmson (1978). This work has not yet been published, so a brief summary is presented here.

Their simulation is initialized from a coarse scale (1 km) version of the same model which, in turn, was initialized with a representative composite sounding from the Del City, OK tornadic storm. The multiple Doppler analyses and coarse scale numerical simulations of that storm can be found in Klemp, et al (1981).

The fine scale (.25 km) numerical simulation resolved small, rapidly evolving storm features which appear to be part of a dynamic structure that consistently develops when a storm enters its tornadic or collapsing phase. The updraft weakens, the "rear flank" downdraft intensifies (see figure C-1), and the downdraft outflow proceeds cyclonically around the main updraft in a fashion similar to an occluding cold front in a mid-latitude cyclone. The maximum vorticity is found at the tip of the occlusion. The downdraft - outflow air becomes mixed with the updraft which hastens the decay of the storm cell.

As the occlusion proceeds, a strong small scale downdraft imbedded in the rear flank downdraft appears in the numerical model and is dubbed the "occlusion downdraft" by the authors. They propose "that this occlusion process and its associated downdraft are dynamically induced by the strong low level rotation which evolves along the

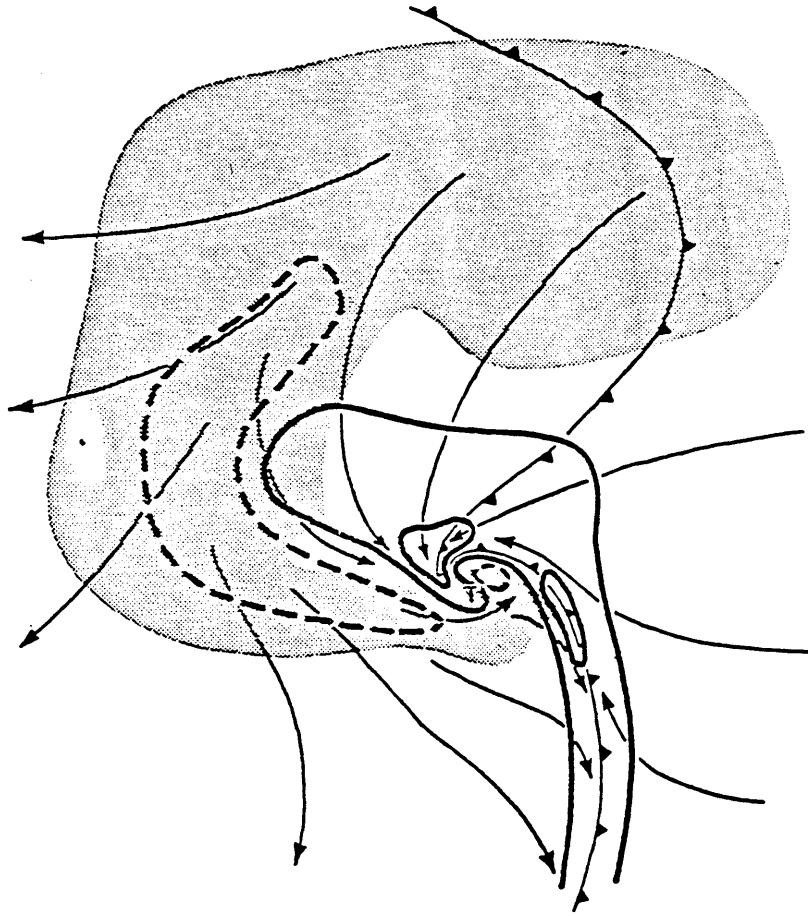


Figure C-1 Taken directly from Klemp and Rotunno (1982). Schematic low level flow field from a composite of the $z=250$ m fields at 120 minutes into the storm scale simulation (See Klemp, et al, 1981) and at 6 minutes into the finer scale resolution simulation. Vertical velocity is contoured approximately at 2 m/s intervals with the zero line omitted and the -1°C isotherm is denoted by the cold frontal boundary. Flow arrows represent storm relative streamlines and the region in which rainwater exceeds 0.5 g/kg is shaded. The location of maximum vorticity is marked with a T. Note the storm scale rear flank downdraft west of the updraft and the small scale occlusion downdraft near the center of circulation.

convergence line. This rotation induces low pressure coincident with the center of circulation and dynamically forces air down from above. In the model, the small scale occlusion downdraft actually forms first at low levels and then extends upward as the flow adjusts to the vertical pressure gradient."

A further analysis of the individual forcing terms in the vertical momentum equation reveals that "the buoyancy induced forcing has only a minor influence" and that "the negative vertical acceleration in the vicinity of the center of circulation is caused primarily by the dynamically induced vertical pressure gradient." A closer look at the dynamic pressure gradient reveals that the contribution directly related to the horizontal curvature of the flow "promotes downdraft intensification along the entire backside of the convergence line and is particularly strong in the vicinity of the center of circulation."

Trajectory analyses indicate that the air just behind the gust front originates at low levels (1 to 2 km) in the inflow air, and circulates around the backside of the storm while descending (see figure 12 in Klemp, et al, 1981). Trajectories of the dry air originating at midlevels indicate that it does not descend directly to the ground but instead mixes with the primary updraft and undergoes a long complicated journey before getting there.

ACKNOWLEDGEMENTS

Thanks go, first of all, to Dr. Kerry Emanuel for suggesting this topic and for otherwise encouraging me to work independently during the course of this research.

Very special thanks go to Dr. Frederick Sanders for all of his help.

I thank Dr. Peter Stone for authorizing a trip to NSSL, without which this work would not have been completed.

I thank my good friend and colleague, John Anderson, for many helpful discussions.

At the National Severe Storms Laboratory, many people too numerous to mention individually deserve thanks. However, I am most grateful to Dr. Peter Ray for the use of his multiple-Doppler radar analysis code, for his help on the 2-Doppler analysis, and for the unique inspiration he provided. I am also very grateful to Sue-Lee Wang for all of her help and her good nature.

This work could not have been completed without the use of the MIT Lincoln Laboratory FAA Weather Project computing facilities. I thank Dr. James Evans and Melvin Stone for their help in arranging my access to Lincoln Lab and for their personal encouragement and support. I also thank Mark Merritt of Lincoln Lab for his computing and graphics assistance.

Many thanks go to my colleague, John DiStefano for his analyses that were used in this thesis and for many helpful conversations throughout the last 6 months.

I thank Dr. T. T. Fujita for sharing his insight in a very helpful conversation.

I thank Dr. R. Passarelli and Dr. N. Gordon for helpful discussions pertaining to the derivation of horizontal wind fields from Doppler velocities.

I also thank Dr. John Boyd for his help.

GOES-EAST satellite pictures which were not published in this study but were very useful were loaned to me by Dr. Aylmer Thompson of the Meteorology department at the Texas A & M University. I thank him and acknowledge the National Earth Satellite Service for these pictures.

REFERENCES

- Brown, R. A., C. R. Safford, S. P. Nelson, D. W. Burgess, W. C. Bumgarner, M. L. Weible, L. C. Fortner, 1981: Multiple Doppler radar analysis of severe thunderstorms: Designing a general analysis system. NOAA Technical Memorandum ERL-NSSL-92.
- Browning, K. A., and R. Wexler, 1968: The determination of kinematic properties of a wind field using Doppler radar. *J. Appl. Met.*, 7, 105-113.
- Caracena, F., 1978: A comparison of 2 downbursts of different size scales. Conference of Weather Forecasting and Analysis and Aviation Meteorology. Silver Springs, MD, 293-300.
- Caracena, F. and M. Maier, 1979: Analysis of a microburst in the FACE meteorological mesonetwork. Eleventh Conference on Severe Local Storms, Kansas City, MO, 279-286.
- Caton, P. G., 1963: The measurement of wind and convergence by Doppler radar. Preprints Tenth Weather Radar Conference., Washington, DC
- Cressman, G. P., 1959: An operational objective analysis system. *Mon. Wea. Rev.*, 87, 367-374.
- DiStefano, J., 1983: Analysis of a thunderstorm downburst. Master's Thesis, Massachusetts Institute of Technology.
- Easterbrook, C. C., 1975: Estimating horizontal wind fields by two dimensional curve fitting of single Doppler radar measurements. Preprints Sixteenth Radar Meteorology Conference, Houston, TX
- Emanuel, K., 1981: A similarity theory for unsaturated downdrafts within clouds. *J. Atmos. Sci.*, 38, 1541-1580.
- Forbes, G., and R. Wakimoto, 1981: A concentrated outbreak of tornadoes, downbursts, and microbursts on 6 August 1977. Submitted to *Monthly Weather Review*.
- Foster, D. S., 1958: Thunderstorm gusts compared with computed downdraft speeds. *Mon. Wea. Rev.*, 86, 91-94.
- Fujita, T. T., 1976: Spearhead echo and downburst near the approach end of a J. F. Kennedy airport runway, NYC. SMRP Research Paper 137, University of Chicago.
- Fujita, T. T., 1978: Manual of downburst identification for Project NIMROD. SMRP Research Paper 156, University of Chicago.
- Fujita, T. T., 1979: Objectives, operation, and results of project NIMROD. Preprints Eleventh Conference on Severe Local Storms, Kansas City, MO.

- Fujita, T. T., 1980: Downbursts and microbursts - an aviation hazard. Preprints Nineteenth Radar Meteorology Conference, Miami Beach, FL.
- Fujita, T. T., 1981: Tornadoes and downbursts in the context of generalized planetary scales. *J. Atmos. Sci.*, 38, 1511-1534
- Fujita, T. T., and H. Byers, 1977: Spearhead echo and downburst in the crash of an airliner. *Mon. Wea. Rev.*, 105, 129-146
- Fujita, T. T., and F. Caracena, 1977: Analysis of three weather related aircraft accidents. *Bull. Amer. Met. Soc.*, 58, 1164-1181
- Fujita, T. T., and R. Wakimoto, 1981: Five scales of airflow associated with a series of downbursts on 16 July 1980. *Mon. Wea. Rev.*, 109, 1438-1456.
- Hamilton, R. E., 1970: Use of detailed intensity radar data in mesoscale surface analysis of the July 4 1969 storm in Ohio. Fourteenth Radar Meteorology Conference, 339-346.
- Holton, J. R., 1972: An introduction to dynamic meteorology. Academic Press. Appendix C, 305-306.
- Klemp, J. B., and R. B. Wilhelmson, 1978: The simulation of three dimensional convective storm dynamics. *J. Atmos. Sci.*, 35, 1070-1096.
- Klemp, J. B., R. B. Wilhelmson, and P. S. Ray, 1981: Observed and numerically simulated structure of a mature supercell thunderstorm. *J. Atmos. Sci.*, 38, 1558-1580.
- Klemp, J. B., and R. Rotunno, 1982: A study of the tornadic region within a supercell thunderstorm. Submitted to ??
- Nolen, R. H., 1959: A radar pattern associated with tornadoes. *Bull. Amer. Met. Soc.*, 40, 277-279.
- Ray, P. S., 1976: Vorticity and divergence fields within tornadic storms from dual Doppler observations. *J. Appl. Met.*, 15, 879-890.
- Ray, P. S., C. L. Ziegler, and W. Bumgarner, 1980: Single- and multiple-Doppler radar observations of tornadic storms. *Mon. Wea. Rev.*, 108, 1607-1625.
- Wakimoto, R., 1982: The life cycle of thunderstorm gust fronts as viewed with Doppler radar and rawinsonde data. *Mon. Wea. Rev.*, 110, 1060-1082.
- Waldteufel, P., and H. Corbin, 1979: On the analysis of single-Doppler radar data. *J. Appl. Met.*, 18, 532-542.